10-4-2006

Preliminary finite element modeling of a piezoelectric actuated marine propulsion fin

Andrew Streett

Preliminary Finite Element Modeling of a Piezoelectric Actuated Marine Propulsion Fin

By

ANDREW R. STREETT

A Thesis Submitted in Partial Fulfillment of the Requirement
for Master of Science in Mechanical Engineering

Approved by:

Dr. Hany Ghoneim – *Thesis Advisor* _____
Department of Mechanical Engineering

Dr. Amitabha Ghosh _____
Department of Mechanical Engineering

Dr. Jeffrey Kozak _____
Department of Mechanical Engineering

Dr. Edward Hensel _____
Department Head of Mechanical Engineering

Department of Mechanical Engineering
Rochester Institute of Technology
Rochester, New York 14623
September 2006

PERMISSION TO REPRODUCE THE THESIS

Preliminary Finite Element Modeling of a Piezoelectric Actuated Marine Propulsion Fin

I, ANDREW R. STREETT, hereby grant permission to the Wallace Memorial Library of Rochester Institute of Technology to reproduce my thesis in the whole or part. Any reproduction will not be for commercial use or profit.

Date: _____ Signature: _____

September 2006

ABSTRACT

New technologies surrounding composite materials and autonomous underwater vehicle (AUV) design have led to numerous studies involving the marine propulsion for these AUVs. AUVs traditionally are classified as highly efficient, payload capable, and can be utilized as reconnaissance or surveillance vehicles. Undullatory and oscillatory propulsion devices have been conceived to replace the present propulsion technologies, of propellers, with highly maneuverable, efficient, and quiet propulsion systems. Undullatory and oscillatory propulsion has been around for centuries employed by aquatic life, but only recently have the mini-technologies been available to present such propulsion devices economically and with enough materials research as to mimic biologic life on the same scale.

Piezoelectric properties coupled with a thin plate allow for actuation properties, similar to bimetallic metals. Applying two piezoelectrics to the fixed end of a cantilevered beam or plate, on opposite sides, and actuating them with an opposite phase shift in electrical voltage potential results in transverse motion of the beam from the orthogonal plane to the vertical axis of the piezoelectric device. Coupling this property to a particular fiber orientation, composite thin plate, significantly increases the actuation properties. In addition, placing more than two piezoelectrics along the length of the thin composite plate gives the potential to increase actuation properties and change the motion from oscillatory to undullatory. These motions can again be increased by utilizing the natural vibration modes of the thin composite plate with piezoelectrics near resonance actuation.

The current research is involved with modeling a piezoelectric actuated marine propulsion fin using the Galerkin finite element technique. An experimental proof of concept was developed to compare results. Using fluid-structure interaction (FSI) methods, it is proposed that the fluid and structure programs are resolved within one program. This is in contrast to traditional attempts at FSI problems that utilize a computational fluid dynamics (CFD) solver transferring load data between a structural dynamics/finite element (FE) program.

ACKNOWLEDGEMENTS

Above all I would like to thank my parents for their incredible support and intuitive sense to understand my potential and push me to the pinnacle of my potential throughout this whole research endeavor and life.

I sincerely thank Dr. Hany Ghoneim for his support, dedication, knowledge and above all positive attitude. From the start he has been able to steer my research and have an undeniable sense of direction with this project. Without his guidance this research would not have succeeded as well as it has. I acknowledge him as a driving force behind my continued interest in this research and many of the topics he has taught me.

I would also like to thank the Department of Mechanical Engineering at the Rochester Institute of Technology, in specific the department head - Dr. Edward Hensel, for supporting this research.

I am grateful to professors Dr. Amitabha Ghosh and Dr. Jeffery Kozak for serving as my thesis committee and taking the time to review my thesis research.

I wish to thank Todd Nichols for his help with ANSYS 9.0 programming questions.

The stimulating discussions on a wide range of finite element computations, mechanics, computational fluid dynamics, and machining from my professors Dr. Agamemnon Crassidis, Dr. Lawrence Agbezuge, Dave Hathaway and colleagues, Ryan F. Schkoda, alike deserve words of appreciation.

TABLE OF CONTENTS

List of Figures

List of Tables

NOMENCLATURE

R_e	Reynolds Number
V_{char}	Characteristic Velocity
L_{char}	Characteristic Length
υ	Kinematic Viscosity
$\underline{v}$	Velocity
p	Pressure
σ_{ij}	Stress Tensor
δ_{ij}	Kronecker Delta
s_{ij}	Deviatoric Stress Tensor
ε_{ij}	Strain Rate/Vector
μ	Dynamic Viscosity
ρ	Density
$\underline{b}$	Body Forces
$\hat{n}$	Unit Normal
$\hat{\tau}$	Unit Tangential
T	Traction Forces
u	Approximate Dependent Variable
Ψ	Interpolation Functions (Shape Functions), normally for Velocity
t	Time
$\underline{f}$, F	External Forces
w	Weighting Function
$[K]$	Viscous Term (Matrix)
$[C]$	Convective Term (Matrix)
$[M]$	Mass Term (Matrix)
$[G]$	Off-Diagonal Viscous Term (Matrix)
(ξ,η)	Local Coordinates on an Element
$[J]$	Jacobian Matrix
Φ	Interpolation Function for Pressure
$\overline{\upsilon}$	Artificial Diffusion
R	Residual
τ	Stabilization Parameter
τ_{SUPG}	Stabilization Parameter for SUPG Method
$h^{\#}$	Local Length Scale
r	Stability Constant
$[\widetilde{k}]$	Stability Viscous Term (Matrix)
$[\widetilde{c}]$	Stability Mass Term (Matrix)
e	Error
Γ	Boundary
Ω	Domain
V	Shear Force

M_z	Moment
c_f	Elastic Foundation Modulus
w	Deflection of beam
q	Transverse Load
E	Modulus of Elasticity
A	Cross-Sectional Area
θ	Slope at Node
ω	Frequency (rad/sec)
L	Total Length
D	Electric Displacement Vector
E	Electric Field
[S]	Compliance matrix
[d]	Piezoelectric Strain Coefficient matrix
$[e]^t$	Electric Displacement-Field matrix
t_b	Thickness of Beam
t_p	Thickness of Piezoelectric
w_p	Width of Piezoelectric
w_b	Width of Beam

1 Introduction

1.1 Background

New technologies surrounding composite materials and autonomous underwater vehicle (AUV) design have led to numerous studies involving the marine propulsion for these AUVs. AUVs traditionally are classified as highly efficient, payload capable, and can be utilized as reconnaissance or surveillance vehicles. Undullatory and oscillatory propulsion devices have been conceived to replace the present propulsion technologies, of propellers, with highly maneuverable, efficient, and quiet propulsion systems. Undullatory and oscillatory propulsion has been around for centuries employed by aquatic life, but only recently have the mini-technologies been available to present such propulsion devices economically and with enough materials research as to mimic biologic life on the same scale. This pursuit, to mimic biological systems, triggered the emergence of the science of biomimetrics, which is the study of natural systems in order to improve the design and functionality of synthetic systems.

The study of fish motion and its highly efficient nature, can be related back to a study done by Lighthill (1960). He applied the slender body theory of hydrodynamics to oscillatory motions of slender fish, which resulted in Elongated Body Theory (EBT). Using EBT, Lighthill was able to show the high propulsion efficiency of aquatic life, which utilized the energy of the surrounding medium to move. This finding is directly attributed to the increased research conducted for marine propulsion. It is very attractive in a world where engines and high power consumption devices are currently being used.

Early pursuits to use the science of biomimetrics for underwater marine propulsion resulted in actuation devices that were either hydraulically or mechanically driven, using conventional motors, linkages and other interfacing parts. These mechanical propulsion devices shared the same problems as propellers with low efficiencies and high thermal energy loss. However new technologies have given rise to an innovative class of electroactive materials, primarily high energy density piezoelectric actuators.

The history of piezoelectricity dates back to 1880 when Pierre and Jacques Curie discovered it in Rochelle Salt and quartz. Piezoelectricity and its effect allow a material to generate an electric charge with the application of pressure. Alternatively, in the presence of an electric field, the material changes shape, which can be developed into actuation.

Piezoelectric properties coupled with a thin plate allow for actuation properties, similar to bimetallic metals. Applying two piezoelectrics to the fixed end of a cantilevered beam or plate, on opposite sides, and actuating them with an opposite phase shift in electrical voltage potential results in transverse motion of the beam from the orthogonal plane to the vertical axis of the piezoelectric device. Coupling this property to a particular fiber orientation, composite thin plate, significantly increases the actuation properties. In addition, placing more than two piezoelectrics along the length of the thin composite plate gives the potential to increase actuation properties and change the motion from oscillatory to undullatory. These motions can again be increased by utilizing the natural vibration modes of the thin composite plate with piezoelectrics near resonance actuation.

This new option to recreate either oscillatory or undullatory underwater marine propulsion by means of a composite fin, has the potential to be very efficient, effective, lightweight, noiseless, with less wake, also neutrally buoyant and fast. It has the potential to either model a caudal fin of a fish as a single composite fin, dual oscillating/undullatory fins like the fins on a sea lion, or a seahorse dorsal fin array as a series of membrane connected fins. Derivative uses could possibly be a means of control for AUVs like a dorsal, pectoral, or anal fin(s) of a fish; the piezoelectrics and composite fibers can be positioned differently to obtain three-dimensional control [Rabinovitch, Vinson (2003)].

1.2 Overview of Marine Propulsion Concepts

Over the past 520 million years nearly 25,000 species of fish have evolved. The mechanical propulsion systems that have developed in fish have not necessarily been the most optimal, but are highly efficient for their surrounding environment and evolutionary

needs, due to the process of natural selection. Some of these highly efficient swimming mechanisms involve a complex relationship between different sets of fins but they provide inspiration for mechanical systems that could possibly outperform them, in certain applications.

The main properties of water, such as incompressibility and high density, have helped to steer the evolution of aquatic locomotion. The incompressibility of water causes the fluid motion, that an aquatic animal creates, to be experienced by the whole length of the animal. This is due to the fact that any motion is automatically transferred from the animal to its surroundings and from its surroundings back to the animal. The density of water allows for more buoyancy and thus a counterbalance to the animals weight. Due to the fact that any motion is directly transferred to other portions of an aquatic animal's body length and the fact that propulsion does not have to develop based on weight restrictions, makes the evolution of marine propulsion highly different than that of any other land based creature.

The main source of propulsion for fish comes from fins mounted in strategic locations along the length of a fish's body. Most fish have a total of seven separate fins. There are two of each pelvic and pectoral fins and one of each of a dorsal, anal and caudal fin. Figure 1 shows the five groupings of fins found on a typical Pumpkinseed sunfish, Lepomis gibbosus.

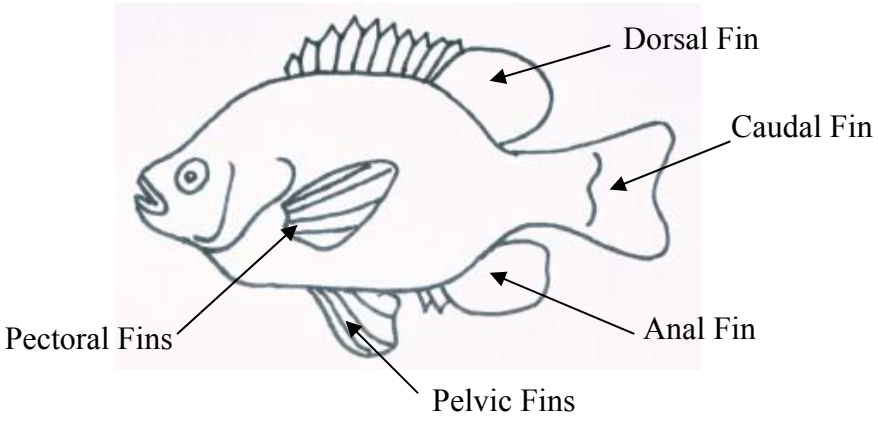

Figure 1: Five groupings of fins on a Pumpkinseed sunfish

The act of swimming involves the transfer of momentum from the fish to the surrounding medium, water, which again reacts and transfers energy to the fish. The main modes of transfer exist within the concepts of drag, lift and acceleration reaction forces. The drag force can be broken up into two main concept areas. The first is viscous drag or friction drag. Friction drag occurs as a result of the viscosity of water and large velocity gradients along the surface of a moving object. It also depends on boundary layer which is a function of water condition and velocity through the medium. The second is pressure drag, which is caused by distorting the medium that is being traveled through. It also corresponds to the energy lost to the medium to create thrust, such as the vortices produced as a fish moves through the water. The lifting reaction force is caused by asymmetric flow and the viscosity of the water. As a fish propels itself, any variation in pressure will cause a lifting force to be generated perpendicular to the flow direction. Last the acceleration reaction force is an inertial force explained by the resistance of the water when an object is accelerating or decelerating through it.

The forces acting on a fish are weight, buoyancy and hydrodynamic lift, exerted in the vertical direction, and thrust and resistance in the horizontal direction, which can be viewed in Figure 2. The components of drag, lift and acceleration reaction forces can be applied to the thrust and resistive forces shown. Finally the body inertial force due to the acceleration of the mass of the fish is also in the horizontal direction.

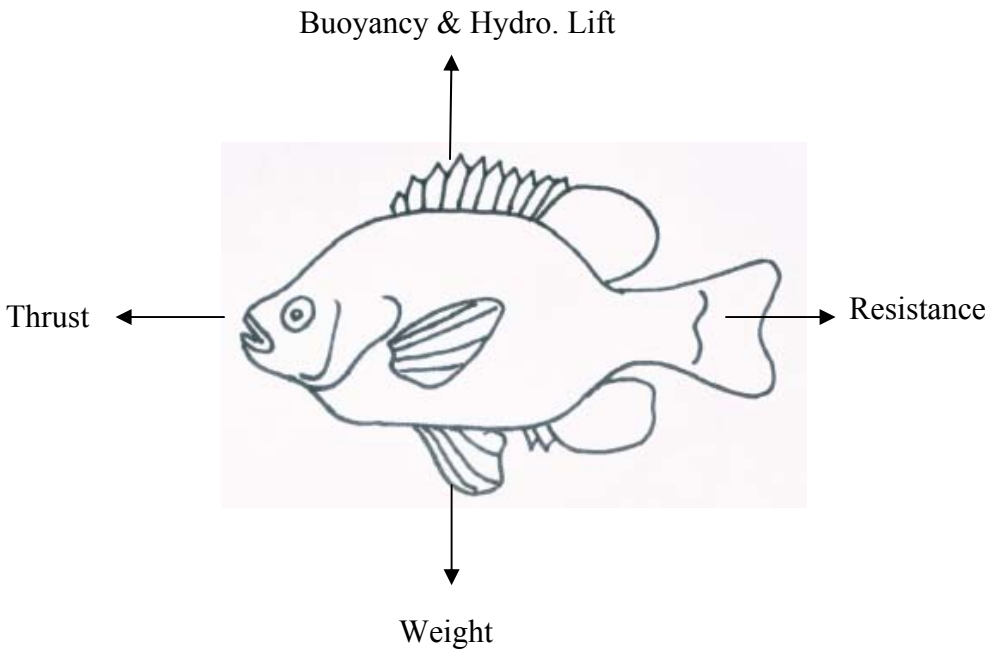

Figure 2: Horizontal and vertical components of force

A quantifying number determining the dynamic similitude between different types of fish with different propulsion properties is the Reynolds number. The Reynolds number is the ratio between the inertial and the viscous forces. It is defined as:

$$R_e = \frac{V_{char} L_{char}}{\upsilon},$$

where V_{char} is the characteristic swimming velocity, L_{char} is the characteristic length of the fish body or propulsor, and υ is the kinematic viscosity defined by the dynamic viscosity divided by the density. For typical adult swimming fish the Reynolds number is reported to be ($10^3 < \mathrm{Re} < 5 \cdot 10^6$) [Sfakiotakis et al. (1999)].

The momentum forces experienced on a swimming fish are all dependent on the type of fish and the propulsion movement it employs. A common distinction made between different types of fish involves undullatory or oscillatory propulsion. Undullatory propulsion involves a traveling wave down the length of the fish's body. Oscillatory motion entails a swinging

pendulum motion that is comparatively rigid. This main distinction exists but it is important to note that oscillatory motion can be derived from a gradual increase of undullatory motion. Both of these modes can exist at once by placing multiple series of oscillatory segments together and generating oscillations either in an in-phase fashion or an out-of-phase fashion. Figure 3 shows the difference between oscillatory and undullatory motion and Figure 4 shows the concept of multiple series of oscillatory segments pieced together to generate an oscillatory motion (in-phase) or undullatory motion (out-of-phase).

Figure 3: Difference between ½ oscillatory wave (left) and ½ undullatory wave (right)

Figure 4: Segmented oscillatory (in-phase) and undullatory (out-of-phase) motion

Five main distinct categories of fish exist between the undullatory and oscillatory continuum, Figure 5. The present research dealing with both oscillatory and undullatory features is most closely associated with the Thunniform and Ostraciiform categories of fish because they are closest to oscillatory motion and due to the small continuum range that exists between slightly undullatory and purely oscillatory motions.

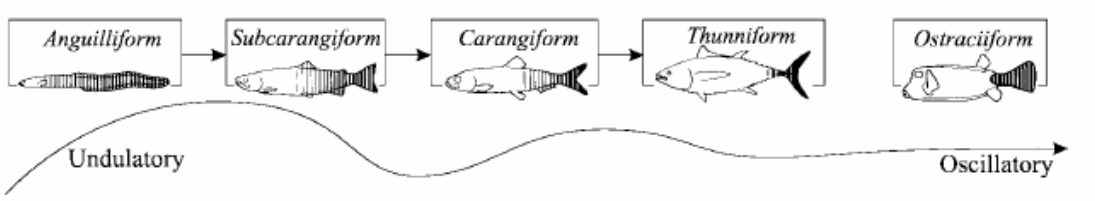

Figure 5: 5 main categories of swimmers – [Adapted from Lindsey (1978)]

The Thunniform mode of marine propulsion is considered a pinnacle of the evolutionary process of marine locomotion because it is found in many forms of aquatic life that evolved separately. It is considered the most efficient, due to the fact that high cruising speeds can be maintained for long periods of time. The caudal fin is stiff and produces large propulsion forces with relatively small amplitudes, while the mass distribution ensures that recoil forces, which are transferred to the leading section of the body as unnecessary vibrations or losses in energy, are minimized. The fact that a Thunniform fish utilizes only the aft section of their body for propulsion and has a stiff tail gives the notion that a flat cantilevered plate with similar size, shape and range of motion should have high efficiency as well, which is the reason for many current research endeavors. The one drawback to Thunniform swimming is that it is optimized for fast swimming in calm waters and not for turning maneuvers or turbulent flow. This is an aspect where nature has optimized based upon the environment, but technology has the ability to improve upon.

The Ostraciiform mode of locomotion is a purely oscillatory motion of the relatively rigid caudal fin [Breder (1926), Blake (1977) (1981)]. Normally this type of propulsion is found on rigid-body aquatic life but is cast as low efficiency, which is primarily used in escape maneuvers or prey stalking. Breder (1926) points out that most aquatic life employing the ostraciiform locomotion did so at low speeds and paired the oscillatory motion of the caudal fin with the undullatory action of their dorsal or anal fins. This has been echoed in present research with supporting experimental work [Drucker and Lauder (2001) (2004)].

The ability for a marine propulsion device to incorporate features of both the Thunniform and the Ostraciiform modes of locomotion could potentially be very efficient at both high

and low speeds. Using the idea of segmented fin propulsion, shown in Figure 4, both of these propulsion actions can co-exist, therefore technology can cater to any environmental setting.

Until recently the caudal fin of Thunniforms was predicted to give 90% of the propulsion force needed to travel thorough the water [Sfakiotakis et al. (1999)]. Multiple studies conducted by Lauder and Drucker (2001) (2004), on perciform fish - a category of fish that fall within undullatory fish, revealed that the caudal fin was actually aided quite significantly by the wake generation of the dorsal fin and they predicted the anal fin as well. Recent adjustments made to the formation of thrust actually show that 37.9% is from the caudal fin, 12.1% is from the soft dorsal fins and 50% is from the pectoral fins of perciform fish, shown in Figure 6. The study shows that fish derive a thrust benefit from the caudal fin passing through the wake shed of the dorsal fin, and presumably the anal fin, shown in Figure 6 [Lauder, Drucker (2004)].

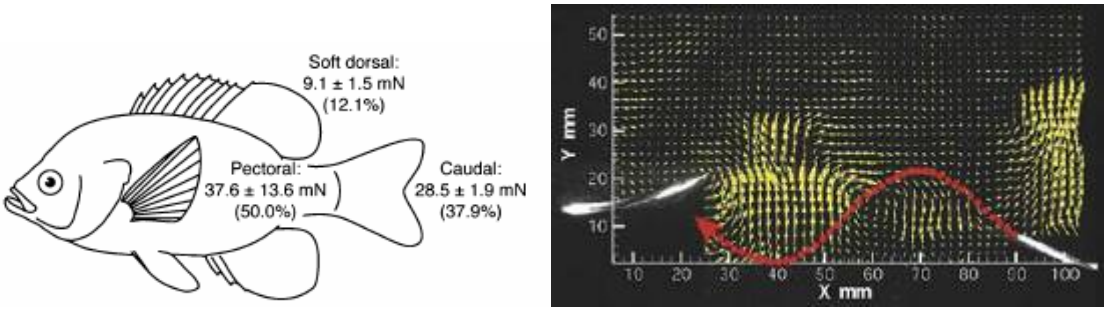

Figure 6: Fish propulsion thrust percentages (left) and wake shedding from DPIV analysis (right) [Adapted from Lauder, Drucker (2004)]

This wake shedding or wake generation that is seen from the dorsal fin, is actually a staggering array of trailing discrete vortices of alternating sign, which are generated as a fin motions back and forth through the water; this is commonly referred to as the classical reverse Kármán vortex street [von Kármán and Burgess (1935)]. The Kármán vortex street pattern is the phenomenon present when a bluff object is placed in a free velocity stream where alternating vorticities are created behind the object curling into the low pressure zone found directly behind the bluff object (Figure 7). Another prominent theory was considered

in 1959 when Rosen concluded that other forms of fish used a "vortex peg" methodology of locomotion whereby vortices are created along the aft end of a fish and the rotational energy that is present in each vortex is extracted when the fish thrusts its body against the resulting vortices. This "vortex peg" method is closely assimilated to the dorsal fin vortex benefit for caudal fin propulsion. Both these theories are experimentally shown and applied to both Thunniform and Ostraciiform modes of marine locomotion, although the reverse Kármán vortex street is most typically related.

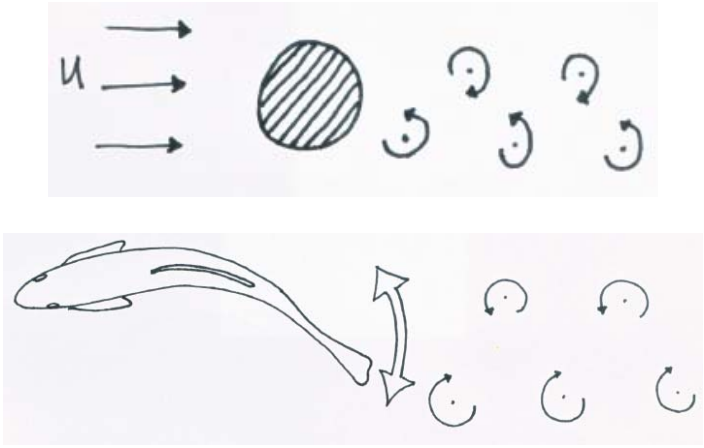

Figure 7: von Kármán street vortex theory (top) and reverse Kármán street vortex theory (bottom) for aquatic animals. Note the rotation of the vortices.

Many mathematical models have been developed that approximate undullatory marine propulsion [Lighthill (1960), Lighthill (1970), Katz and Weihs (1979), and Root and Long (1997)], however they have not yet been able to adequately describe Thunniform motion due to the shape of the caudal and pectoral fins. There have also been numerous studies conducted on purely undullatory motion [Ayers (2000), Allen and Smits (2001), and Liu and Kawachi (1999)]. Bountiful research and simulations have also been conducted that model oscillating plates and their independent effect on the propulsion of a fish [Streitlien and Triantafyllou (1998), Wu (1961), Triantafyllou et al. (1993), Bandyopadhyay (1997), Anderson et al. (1998), Hover et al. (2004), Murray and Howle (2003)]. It is also known that numerical studies are being conducted using complex computational fluid dynamics on the entire body of a fish to better understand and quantify the effect of the upstream movements of a fish to its aft motions. An area of research that has not had a thorough inspection is

simulating the interaction of the dorsal fin and the caudal fin, expressed by Lauder and Drucker (2004).

1.3 AUV Research and Development on a 'Large' Scale

The fact that the Thunniform mode of marine locomotion is known to be highly efficient has spawned many research avenues on the complexities involved with reproducing this type of propulsion for an AUV concept. Some of the most well-known research has been developed at MIT and involves RoboTuna, RoboPike, and a derivative of RoboTuna called Proteus the Penguin Boat.

RoboTuna is a robotic fish that uses motors and pulleys to actuate the undullatory motion of its tail. RoboTuna was created in 1995 and modeled after a blue fin tuna. It is used to study the efficiency of undullatory motion in aquatic life which is the primary question in Gray's Paradox. In 1936 James Gray came up with Gray's paradox, which estimates that the power required by dolphins to achieve the swimming abilities that they have is approximately 10 times greater than the amount of power available from their muscles. RoboTuna was able to give insight into the mechanism by which efficient marine propulsion could be achieved and gave clues to reason Gray's Paradox. RoboTuna was reported to have an 86 percent efficiency which was calculated based on sensors attached to the pulley-string actuation system it employed.

RoboPike is a relative of RoboTuna and it was designed to accurately depict marine locomotion on a 32 inch platform. It uses the same type of actuation as the RoboTuna, with motors, steel cables and pulleys. Again Gray's paradox was a problem to solve.

Proteus the Penguin boat was an offspring idea to RoboTuna that uses two oscillatory flippers controlled by mechanic drive motors and linkages at the stern of the boat, which mimics the marine propulsion used by Penguins. The research conducted in the laboratory achieved 87 percent efficiency whereas current propeller systems are at or below 70 percent

efficient [Penguin Boat (1997)]. The general dimensions of the flippers are less than a foot long and the boat is 12 feet long by 1.5 feet wide.

RoboTuna, RoboPike and Proteus showed that undullatory and oscillatory modes of locomotion are viable forms of propulsion, however the heavy and bulky equipment used to manipulate the propulsion can be improved upon and made smaller to follow more AUV-based design criteria like being less visible and having an ability to carry payload.

In response to trying to locate current mini-technologies that would allow for marine propulsion, a model was produced in 2001 by Charles Stark Draper Laboratory in Massachusetts that closely resembled a yellow fin tuna. The 2.4 m long, 142 kg, model was constructed of a main body cavity to hold components, and 4 hydraulically controlled, segmented sections to construct the undullatory motion of the tuna's propulsion. An in-depth study was conducted and found that an aquatic animal of this size requires strain and forces equivalent to 30 percent more than natural muscle ability. Following these results, artificial muscle actuators such as polymer based MEMS and integrated force array electrostatic actuators and EPAM, silicone and polyurethane electrostrictive actuators were compared to the needed power requirements. At the time of the study there were no candidate actuators that satisfied the extremely high requirements of strain [Kerrebrock, Anderson, Parry (2001)]. This study evolved the segmented fin idea and reinforces the need for larger/heavier actuators to be involved in the marine propulsion for vehicles of this size. Therefore for AUVs, the size is somewhat restricted due to materials available. The direct response to RoboTuna's, RoboPike's, Proteus's and this research was to look to mini-technologies that have the potential to power much smaller AUVs.

1.4 AUV Research and Development on a 'Small' Scale

Mini-technologies refer to electrically controlled devices that allow for actuation on a very small scale. These mini-technologies can incorporate electrostrictive transducers,

magnetostrictive materials, shape-memory-alloy wires, polyelectrolyte gels, conducting polymers and piezoelectric actuators.

Electrostrictive materials operate under the influence of an electric field, which elastically deforms its dielectric material. Electrostrictive materials are mostly based on lead (Pb) Niobium (Nb) and Magnesium (Mg). They are classified as a type of material that changes length due to a spontaneous orientation of their dipoles in an electric field. Electrostrictive materials have the unique ability to elongate in both a positive and a negative electric field. However electrostrictive material drawbacks include highly non-linear behavior with high hysteresis and they are very temperature dependent.

Magnetostrictive materials, such as TerfenolD, expand more than 1400 micro-meters under high magnetic fields due to the alignment of their magnetic domains. These types of materials are good for giant dynamical strains, low-frequency domains, low hysteresis, high temperature ranges and low driving power input. They also exhibit linear behavior, which is a positive aspect for modeling reasons. Unfortunately large, heavy magnets are often necessary to produce such magnetic fields and magnetostrictive materials can normally only utilize a vertical change in displacement.

Shape Memory Alloy (SMA) wires have the ability to eradicate a deformation and recover a predefined, or imprinted, shape due to a solid-solid phase transition that takes place in a specific temperature interval. Typical SMA wires are Nitinol (NiTi) and it is proven to achieve an 8 percent strain when induced with heat or electrical energy. Other typical SMA actuators are CuAl(Ni,Zn) which can only produce 4 percent strain but cost about one-tenth of Nitinol. Above the transition temperature of a SMA wire, the austenistic state, the wire exhibits symmetrical crystalline structure and a high modulus of elasticity and below the transformation state, or martenistic state, the wire is more stable with respect to thermodynamic properties. As the SMA wire has current driven through it, its resistive properties cause heat to build up and as this happens the wire goes through its phase change and stiffens up. The positive aspects of using a SMA wire is that they can model muscle fibers that have already been studied under the biology side of biomimetrics and they have

been significantly researched in the past decades to be comparable to human muscle tissue; when they are grouped together. The drawbacks to SMA wires are that they need to dissipate heat to return to their predefined shape, or non-strained state. Also they exhibit non-linear behavior, actuation loss and fatigue over repetitive cyclic loading, low energy efficiencies and relatively large current requirements which causes a need for large, heavy batteries for remote use.

Poly-electrolyte gels and conducting polymers both use polymer molecules to exhibit a displacement gradient. Poly-electrolyte gels have a cross-linked network of long polymer molecules that generate a pH gradient when an electrical field is introduced. This pH gradient results in mechanical work that has been reported to be on the same level as human muscles. The conducting polymers need to be doped with another polymer to change the conductivity of the overall system. Due to the increase in conductivity and doping material used, a change in volume is experienced. Both of these materials are on the fore-front of technology and not many commercially available products exist.

Piezoelectric materials were discovered in 1880 by Pierre and Jacques Curie when they found that pressure generated an electrical charge in Rochelle Salt and Quartz. An inverse piezoelectric effect is when a piezoelectric material changes shape due to their crystalline electrical dipoles spontaneously aligning in an electric field causing deformation of the crystalline structure. Until about 1950 piezoelectric sensors and actuators progressed slowly because material science could not synthetically produce many materials capable of material properties higher than naturally occurring piezoelectric materials. The $BaTiO_3$ transducer was the main topic of research until about 1950 when Japanese research found phase diagrams and high temperature capability for materials in the PZT, or lead zirconate titanate ($Pb(Zr,Ti)O_3$), category. This breed new research avenues and ceramic PZTs have been the dominant form of piezoelectric actuators since then. New research into piezoelectric actuators has been focused on doping PZT material with transition metals like Lanthanum, (La) or Niobium (Nb). It has been proven that this doping significantly effects piezoelectric properties. For example PLZT, PZT doped with La, exhibit strains up to two times as much as PZT materials. Also there are current research endeavors to uncover the maximum strain

advantage of piezoelectric monocrystals, which have the potential of producing as much as eight times the amount of strain as a typical PZT material [Janocha (1999)].

The past decade of research into AUV propulsion utilizes almost all of these actuation options with varied results. The following review outlines a majority of the AUV concepts that were produced in the past decade utilizing the previously mentioned materials. As the progression of materials changed and developed, new types of actuation were attainable and that is evident in the following review.

In 1995 the Department of Micro Systems Engineering at Nagoya University in Japan developed a micro-marine vehicle utilizing PZT, or a piezoelectric as an actuator. The main mode of thrust utilized the natural frequency of the body structure which held the PZT and moved out to the two 'legs' each having dual fins at the end. This research is important because it utilized piezoelectrics to vibrate a structure at resonance, which in turn gave the micro-fins, located at the end of the structure, a vibration to propel the micro-vehicle [Fukada et al. (1995)]. At that time, the drawback to using piezoelectrics as a form of actuation was that they had relatively low energy densities compared to other actuation materials.

In 1997 the University of Mexico introduced the use of DuPont polyelectrolyte Ion-Exchange Membrane Metal Composites (IEMMC) as a viable undullatory propulsion device. Using a 2 and 1/4 in^2 strip (0.0072 inches thick) of the composite membrane a small Styrofoam boat, approximately 3 in^2, was propelled at almost 0.8 in/sec. The theory of locomotion recognizes Rosen's (1959) contribution to biomimetrics by stating his "vortex peg" hypothesis is being applied to the compliant sheets of composite membrane. The ability for the boat to be propelled forward with only a 2 VAC input signal was a major step forward in relinquishing large batteries for mechanical drive motors [Mojarrad, Shahinpoor (1997)].

In 2000, Biomimetric Products used a relatively new class of electroactive materials called ionic polymer composites to replicate the undulating motion of aquatic propulsion by means of Composite Artificial Muscle (CAM) fins. The tests were conducted using a 0.17 mm thick CAM polymeric membrane fin, 2.54 cm wide by 3.81 cm long. The voltage

requirements never ran higher than 10 VPP and 0.8 grams was reportedly the highest value of thrust attained. Using CAM fin propulsion, the results showed that the bending-oscillatory motion was a viable means of efficient forward propulsion and steering for a vehicle of its size. Although the voltage requirements were low, the size and thrust values are not very attractive to any AUV propulsion of slightly larger magnitude [Mojarrad (2000)].

In 2001, a transducer material called Ionic Polymer Composite Metal (IPCM) was used to produce a swimming micro robot using the dual fin feature like a sea lion. The best result from this type of material was modeled as a bending beam. This was due to the fact that the 12x10x0.01 mm IPMC was very compliant and a very small section of it had to be used to get any reasonable motion. It was also reported that IPMC materials have a very non-linear behavior with great hysteris; both do not help to obtain repeatable results. The conclusion was that generation of thrust is possible but for longer pieces, undullatory motion must be aided with another stiffer material [Laurent and Piat (2001)].

The most recent adjustment in actuator technologies for AUV designs was reported in 2000 when a lamprey robot was developed by Northeastern University using ten 0.01 inch Nitinol (SMA) wires to control the undullatory motion. Also in 2002 when Texas A&M University published results on a six-segment underwater hydrofoil also utilizing the Shape-Memory-Alloy (SMA) actuator technology. SMA actuators are wires that change shape when they are heated and then are brought back to their original shape when they are cooled. The benefit to using the SMA wires underwater is that they can be cooled quicker using the surrounding medium and low driving voltages. The drawbacks are fatigue over repetitive cyclic loading, low efficiency, and relatively large current requirements. The Texas A&M study used a NACA 0009 airfoil with a 30 in chord and found that tail-only actuation was able to generate more force than the traveling sine wave actuation scheme. It also found that the resonance frequency of the whole system plays a large part in reducing power requirements and due to the fact that the tail was compliant at the far aft segment, the mass of the traveling water was able to deform it to a point that was not optimal for force characteristics [Rediniotis et al. (2002)].

Steering an AUV is also of multi-disciplinary concern when an AUV propulsion system is being developed. Due to the multi-function of the propulsion system, it needs to respond to changes in controller input. In 2003, using IPMC actuators, a tadpole robot, called TadRob, was constructed and achieved a moving speed of 13.5 mm/sec under oscillatory propulsion. A main point of this research was that changing the duty ratio of the input signal allowed for controlled turning maneuvers [Jung et al. (2003)]. Also in 2004, at the University of Washington's Center for Intelligent Materials and Systems a design for a hammerhead shark aquatic model was conceived with SMA actuators. Utilizing two plates they devised a way to design for steering and diving up and down [Ono et al. (2004)]. Although this current research is not directly concerned with steering requirements, it is possible to devise a system using the proposed components, so future experimental work can succeed easily.

The research over the past decade has developed a wealth of important information but the utilization of various propulsion materials depends on the size and shape of the aquatic propulsion required. This wide range of materials does not allow for an easily conceived grouping scheme. Instead the most basic way to organize the AUV propulsion research would be through means of four sizing categories: Large (Greater than 4 feet in length – RoboTuna, RoboPike, Proteus and Yellowfin Tuna AUV), Medium (between 4 feet and 1 foot – Lamprey, Hammerhead, CAM AUV, and Texas A&M hydrofoil), Small (between 1 foot and 3 in – perciform research) and Micro (less than 3 in – TadRob, PZT microrobot, IEMMC & IPMC creations) aquatic propulsion vehicles. Although the Micro group has bountiful research and many avenues of future development, it is apparent that the potential of such small AUVs decreases drastically once they leave the quiet, undisturbed laboratory and enter an environment full of currents, wakes and plenty of larger predators. Some Micro AUV devices have been assigned to medical uses primarily for investigation into the body with sensors and cameras using Micro AUV propulsion technology.

There is an obvious gap in research, between 1 foot and 3 inch AUVs, which applies directly to a huge category of aquatic life and a vast majority of the research taking place for biomimetrics, on the biology side, such as sunfish [Lauder and Drucker]. The need for

representative research in this field on the engineering side of biomimetrics, is one reason for the current research into a piezoelectric actuated composite fin.

1.5 Piezoelectric Research for Small AUVs

The actuation technology, outlined above, has shed light on the reasons to use and not to use specific types of actuation based on size and propulsion thrust requirements. From the past 10 years the actuators have been primarily SMA wires, IPMC, IEMMC, CAM and PZT actuators. SMAs are at the forefront of biomimetric research because they represent muscle contractions and can be implemented similar to already existing muscle structure. However their drawbacks, such as actuator loss and fatigue over repetitive cyclic loading, low energy efficiencies, relatively large current requirements and it is necessary to dissipate heat to return the SMA wire to its original position, for AUV design, outweigh their usefulness. A group of actuators called electroactive polymers is what encompasses IPMC and IEMMC actuators. It appears from the previous research that they are primarily useful with the Micro scale AUVs, not for the scale that the current research is concerned with. Since 1995 PZT technology has been quite successful in producing actuators with high energy densities that when combined with other materials, have the potential to be successful on the small scale AUVs (1 foot to 3 inches). This potential is due to the fact that over the last 10 years piezoelectric devices have been researched extensively.

Piezoelectric materials have been researched since the mid 1980's to provide structures with vibration control, aeroelastic tailoring, helicopter rotor blade control, noise suppression, etc. The reasons for this research are that piezoelectrics offer a low weight, high energy density, and high frequency response. For the past ten years the major hurdle to implementing these types of actuators on many more devices have been the limitations that exist on the displacement, or the stroke. New breeds of piezoelectric actuators have recently been uncovered and obtain a substantial increase in stroke compared to its predecessors, when used in a cantilevered situation.

The Thin Layer Composite Unimorph Ferroelectric Driver and Sensor, or THUNDER, actuator was discovered at the NASA Langley Research Center in 1994. Since then the Face International Corporation has been developing these actuators for commercial uses. The actuator is a ceramic wafer attached to a metal plate using polymide (LaRC-SI) adhesive film. The prestressed piezoelectric ceramic achieves various displacements depending on its boundary conditions at either end of the plate [Mulling et al. (2000)]. Face International Corporation reports an 8mm displacement at the free end of the cantilevered metal plate for its TH-7R THUNDER actuator [THUNDER TH-7R (2006), Face (2002) (2001)].

In 2001, THUNDER actuators were employed to design a miniature aquatic vehicle composed of a small boat actuating a single fin in oscillatory motion at Ohio State University [Miniature (2001)]. Also in 2001 the Center for Intelligent Mechatronics developed a mesoscale robotic insect capable of terrestrial movements using two THUNDER piezoelectrics to actuate its legs. It is capable of multi-degree of freedom locomotion that allows it to navigate rough terrain [Goldfarb (2000)]. The piezoelectrics have also been investigated using analytical models and finite element analysis [Cappozzoli et al. 1999, Taleghani and Campbell (1999), Barmac (2000)].

The submerged marine propulsive thrust of these actuators has only recently been investigated in 2002 by University of Florida. Designing a clamshell structure using two THUNDER piezoelectrics positioned on top of one another, the analytical and experimental research concluded that the peak value of momentum flux was approximately 4.5N at a resonance frequency of 14 Hz. It was also reported that the average power consumption was only 8W, compared to another marine propulsion device currently being used, the Autonomous Benthic Explorer (ABE), that consumes 50W [Balakrishnan and Niezrecki (2002)].

Past research has indicated that piezoelectric materials are not a good choice for marine propulsion actuation because they have high voltage requirements, their high frequency potential will not be utilized, and they do not have adequate energy density or stroke [Redinotis et al. (2002) and Kerrebrock, Anderson, Parry (2001)]. The THUNDER actuator

and other newly conceived piezoelectric actuators, like the Sonox P505, have the potential to eliminate the last drawback.

The high voltage requirements can be weighed against other actuation technologies to determine that even though a piezoelectric actuator may need high voltage, its overall power requirements are quite low. It is reported by Niezrecki and Cudney (1994) that a piezoelectric actuator can be operated at the actuator's electrical resonance, with an inductor, to virtually eliminate the actuator's power consumption when they are configured in parallel. The whole premise to a piezoelectric actuator is that it needs an electrical field to produce a stroke; more stroke equals more voltage, and in turn more current. The research from Niezrecki and Cudney (1994) showed that depending on a parallel or series connection between a PZT and an inductor, the current consumption dropped by 75% or the voltage was increased by 300%, respectively. These options are beneficial, specifically the parallel circuit results for dropping the overall power consumption drastically. Therefore using this research the drawback of PZTs dealing with high voltage, considering power, can be eliminated [Balakrishnan and Niezrecki (2002)].

The high voltage requirement also is a drawback because it will be surrounded by water, obviously two mediums that do not react well with one another. The only actuator that can easily be submerged in water is an electroactive polymer, however it was determined, based on past research, that it is not an appropriate choice for small AUV propulsion. Between the other different actuation technologies that have been implemented and could be used, i.e. SMA wires, CAM, other electroactive materials, magnetostrictive materials, polyelectrolyte gels, and conducting polymers, all use some type of voltage requirements [Janocha (1999)]. Aside from electroactive polymers like the ones employed on the IEMMC and IPMC projects, the rest of the actuators' power connections need some level of protection. Therefore any type of actuator must be properly constructed as to minimize water damage on any scale bigger than the micro category of AUVs. Due to this fact and the overall low power consumption that can be implemented for a very high mechanical power density, the piezoelectric actuators are the best choice for small AUV propulsion actuation.

The high frequencies that a piezoelectric actuator can sustain are useful to a point, it should not be a limitation to an underwater marine propulsion device. Using a piezoelectric in a cantilevered beam configuration allows many modes to be expressed through various frequencies created by the piezoelectric. The natural damping of the beam in addition to the damping caused by the water after actuation, requires that the piezoelectric be run at a higher frequency than what is achieved by the propulsion device in air. Also, a higher frequency range could lead to better propulsion due to different mode shapes experienced by the beam.

The features of a piezoelectric that were once a limitation to its uses, have been researched enough to allow piezoelectrics to break out as a primary choice for marine underwater propulsion actuation. The actuators are also quiet and when laid up with fibrous composites provide cheap and easy construction with high repeatability.

1.6 Experimental Proof of Concept Test and Equipment

Preface

The previous review indicated that piezoelectric actuators coupled with a fibrous composite plate have high potential when being used as an underwater propulsion device on small AUVs. An experimental proof of concept was developed to initially test this new underwater propulsion idea. The experimental proof of concept will be presented briefly and generally to allow the understanding of how to construct the setup and use the equipment. Experimental results will not be formed from this test setup, but generalizations will be formed about the primary test that was conducted. The primary test is interested in construction techniques and finding out to what extent the composite fin will move underwater. It is concerned with holding boundary conditions, protecting electrical components from the water and understanding the testing equipment connections/real-time observations.

1.6.1 Piezoelectric Actuated Composite Fin Construction

The piezoelectric actuated composite fin (Figure 8) was constructed at RIT using standard vacuum bag techniques for composite materials. The sandwich lay-up consisted of two piezoelectrics placed at one end on opposite sides of the [0/0/90/90] E-glass epoxy cross-ply laminate. The vacuum bag setup can be seen in Figure 8.

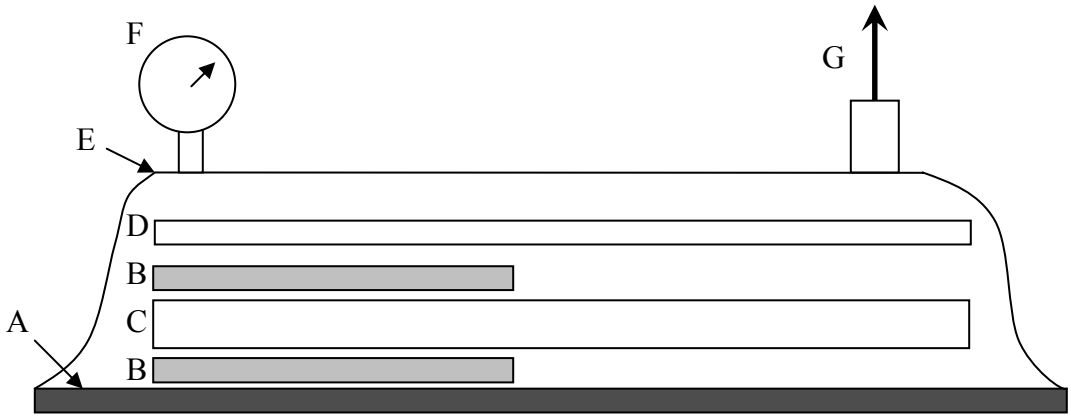

Figure 8: Vacuum bag setup for construction of composite fin with piezoelectrics

where A is a flat plate, B is a piezoelectric, C is the composite E-glass cross-ply laminate [0/0/90/90], D is the combination of peel ply and breather material (standard vacuum bagging supplies), E is the vacuum bag, F is the vacuum gauge and G is the vacuum suction hole.

The reason for using the composite materials in a laminate orientation of [0/0/90/90] was to take advantage of a coupling effect of the in-plane stress-strain relationships that can exist in fibrous composites of [0/90] orientation. When the particular orientation of [0/90] is strained in one of the 0 or 90 degree directions, a bending moment is created in the fibrous composite. Since the piezoelectric exerts a high strain in a specified direction, it is the strain exertion on the fibrous [0/90] composite that causes an internal stress and produces bending tendencies. The bending tendencies can be further enhanced by placing the piezoelectric further from the neutral axis of the composite laminate. This can be further analyzed through equations in Chapter 9 for a typical laminated piezoelectric beam element. Furthermore, the number of [0/90] plies was chosen to be [0/0/90/90] because the number of plies had to be a

power of two and a third set of [0/90] layers would have resulted in a fin that was too stiff for the piezoelectrics to move; however one set was to compliant for underwater propulsion.

The piezoelectric chosen was the Sonox P505 piezoelectric bender, made of 5A1 PZT material. This specific piezoelectric material was chosen because, compared to other very thin PZT materials available, it had a relatively high piezoelectric charge coefficient in the lateral direction. This means that it had the highest energy density for transverse loading conditions, see Figure 61, or that it would produce the most strain in the preferred direction (transversely). Many companies manufacture 5A1 material thin piezoelectrics, so cost was also considered in the choice. A comparison study of the main piezoelectric modeling properties of interest for two leading manufactures of thin 5A1 piezoelectric actuators can be seen in Table 1. The other brand of piezoelectric, the Type E Piezo-Bender, is sold by the same company that produces the THUNDER actuators mentioned previously.

Comparison Study of Two Piezoelectric Actuators:

		Sonox P505	Type E Piezo-Bender
Electromechanical Properties:			
Charge Coefficients (10^{-12} C/N) -	d_{31}	-185	-175
	d_{33}	440	415
	d_{15}	560	650
Mechanical Properties:			
Density (g/cm^3)		7.8	7.6
Compliance Constants (10^{-12} C/N) -	S_{11}	18.5	15.7
	S_{33}	20.7	18.2

Table 1: Comparison of Piezoelectric Actuators

Note that the highlighted numbers represent the transverse energy density. Cost was relatively the same, so the Sonox P505 was chosen because of the larger transverse charge coefficient.

The experimental composite fin with embedded piezoelectrics can be seen in Figure 9.

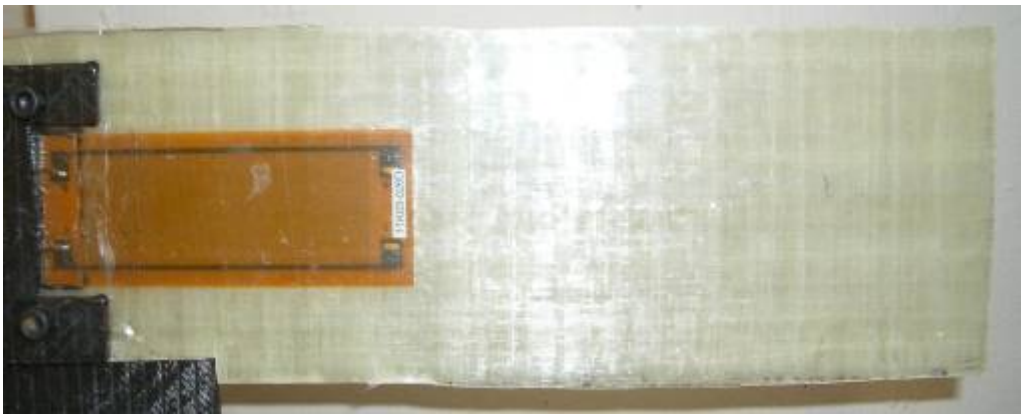

Figure 9: 12 inch long cantilevered piezoelectric actuated composite fin

1.6.2 Full Test Setup and Equipment Used

The test setup allows the piezoelectric composite fin to be securely fastened, in a cantilevered plate boundary condition, while allowing it to move linearly through the water with minimal resistance. Two testing platforms were created to sustain cantilevered boundary conditions: one to test initial results with very little propulsion force and a second larger and more robust platform, which will allow for more linear movement through the water.

The overall test setup can be seen in Figure 10 and consists of:

1. Test Platform (Fin attached)
2. Linear Constrained Motion Guides
3. Water Tank
4. Tektronic 2221 60MHz Digital Storage Oscilloscope
5. Tektronic CFG253 3MHz Function Generator
6. Trek Model PZD700-1-L-CE Piezo Driver/Amplifier Series

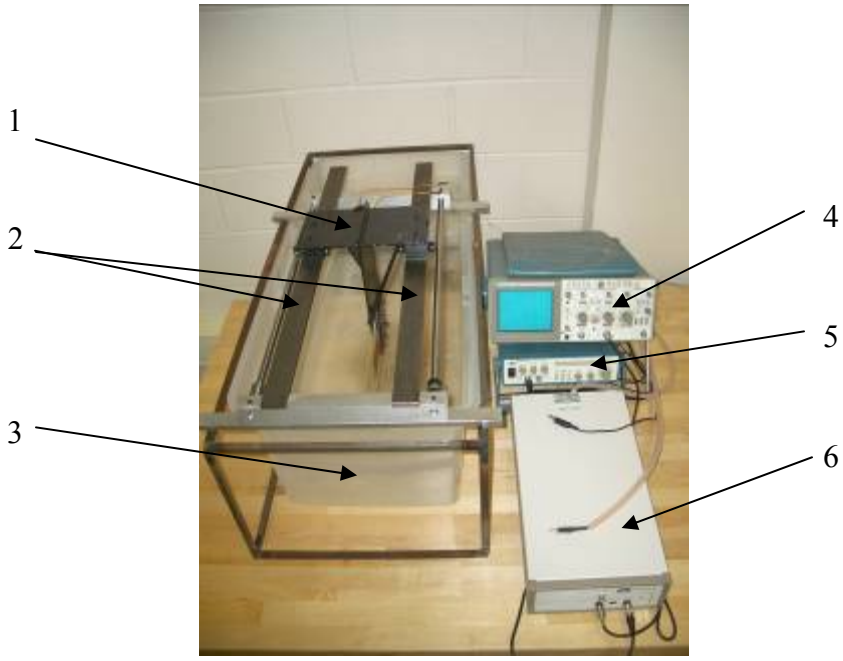

Figure 10: Full test setup

The overall test setup can also be viewed in a simplified diagram, by Figure 11:

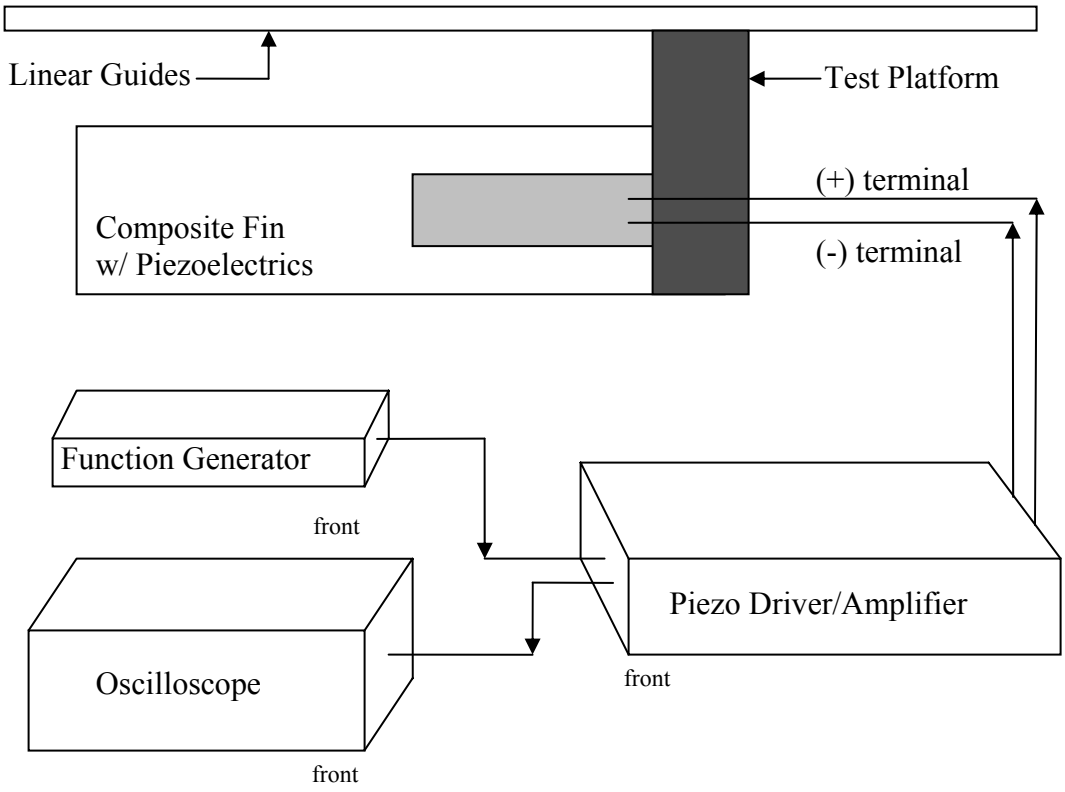

Figure 11: Simplified Diagram of Test Setup with Electrical Connections

1.6.3 Specific Components in Test Setup

There are two types of testing platforms. The first testing platform created was to deal with initial testing and start-up where very little thrust, if any, was expected from the marine propulsion fin. It was designed with lightweight carbon fiber plates and very low friction pillow linear bearings, which act as the system's linearly constrained motion guides. The marine propulsion fin is sandwiched between two plates of carbon fiber, which has a very low water absorption rate, and secured using 6, ¼"-20 bolts and nuts to simulate a cantilevered boundary condition at one end of the fin. The extension plate, which allows the marine propulsion fin to sit in the water, is reinforced with two 30 degree spars. The whole setup is attached to a stationary carbon fiber plate which has hole locations to line up with the linear pillow bearings. The pillow bearings are allowed to travel a maximum of 0.025 meters

at an extremely low friction loss. All carbon fiber plates were created at RIT using the standard vacuum bagging techniques for composite materials. Figure 12 shows the first testing platform and Figure 13 shows an exploded CAD drawing of the five pieces that make up the platform.

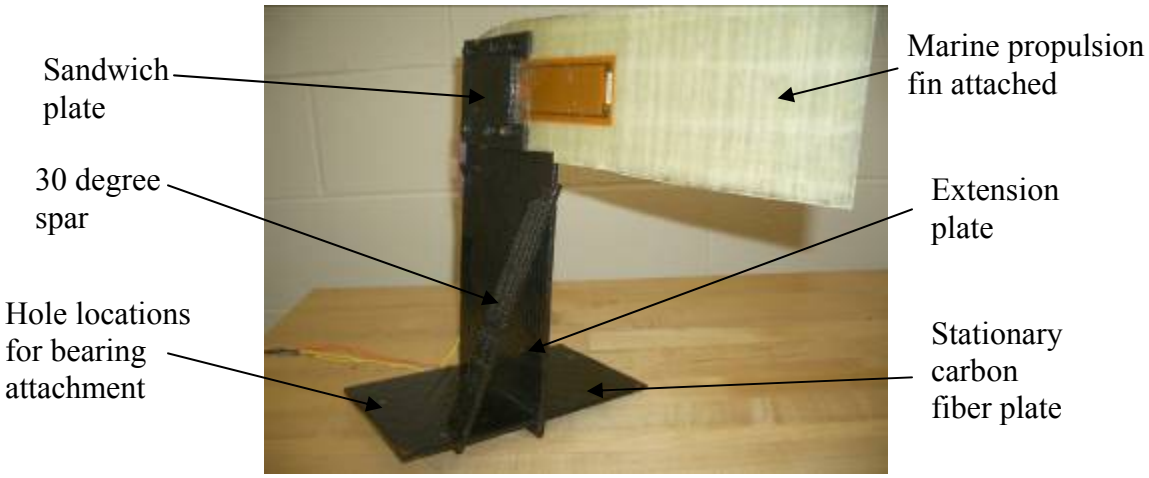

Figure 12: Inverted (upside-down) view of low thrust test platform with marine propulsion fin

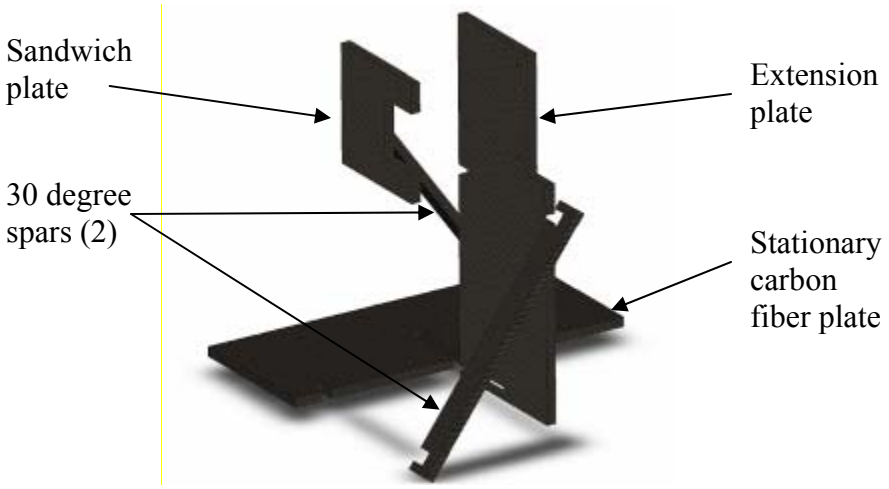

Figure 13: Exploded view of assembly for first test platform

The second test platform, Figure 14, was created to travel farther distances, on the order of 0.3 meters, with the idea of higher thrust values, if any were achieved. The test platform was created similar to the low thrust platform but it was made of aluminum, due to its non-

rust properties. It uses 4 small roller bearings per side, Figure 15, to achieve low friction losses while being directed across the linear constrained motion guides, which are 0.127m diameter machined steel rods. Using the tangent of the rods and the tangent point on low friction roller bearings, the setup has very low friction losses. Sandwich plates are again used to sustain the cantilevered plate boundary condition. The cantilevered plate boundary condition is also upheld by the extension plate being rigidly connected to the stationary plate by three machined nut and bolt locations.

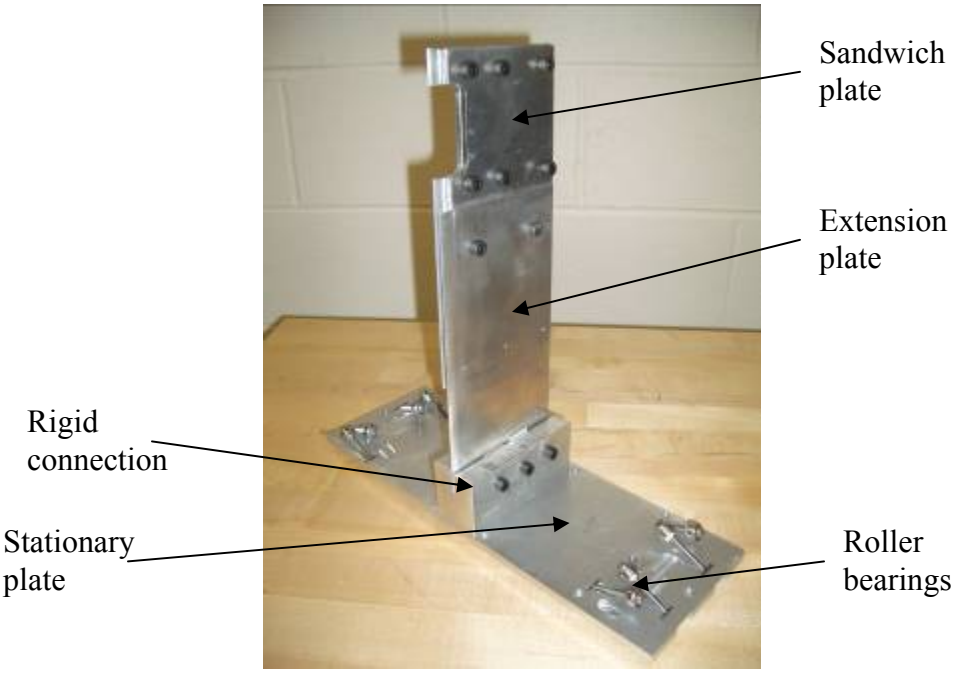

Figure 14: Inverted (upside-down) view of high thrust test platform

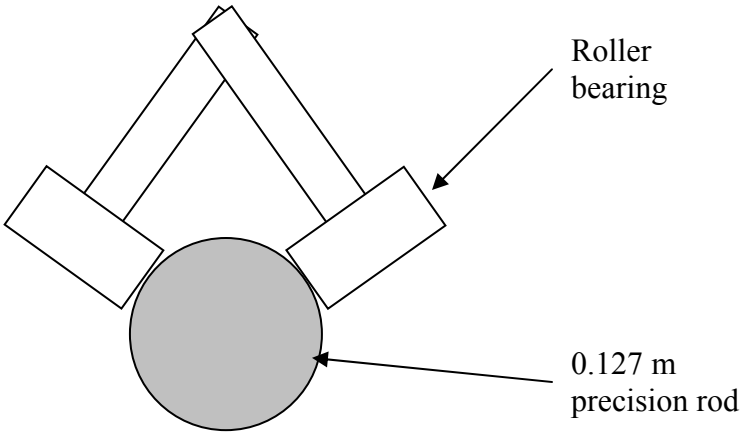

Figure 15: Display low friction concept for linear constrained motion

The water tank consists of a HDPE container outlined by a 0.9144 x 0.4572 x 0.3048 meters 1018 steel frame. The water level in the water tank is kept at a constant 0.254 meters deep.

The Tektronic 2221 60MHz Digital Storage Oscilloscope was used to monitor the input signal to the piezoelectric. For the Sonox P505 piezoelectric there is a maximum peak-to-peak voltage of 500 Volts. For the initial experiment the voltage was kept well below this peak, at 250 Volts Peak-to-Peak (VPP), due to the fact that the oscilloscope could not detect higher than positive/negative 250 Volts.

The Tektronic CFG253 3MHz Function Generator was used to produce a sine wave at 2 VPP at different frequencies, depending on the mode of the fin that was trying to be excited. The reason for using 2 VPP input signal was that it was easy to implement precise amplification to the signal to obtain the 250 DC VPP needed.

The Trek Model PZD700-1-L-CE Piezo Driver/Amplifier Series made it possible to change the 2 VPP input signal from the function generator into a 250 DC VPP output signal that was sent to the piezoelectrics. It is a high-voltage DC power amplifier that has the ability to amplify a signal 300V/V. This device has the maximum capacity to output 700

VPP or 1.4 kV in the positive or negative direction from 0 Volts. Further testing will utilize up to 500 VPP.

1.6.4 Operating the Test Setup

Use Figure 11 as a wiring diagram for the electrical components. The function generator supplies the initial signal to the driver/amplifier, the oscilloscope monitors the output of the driver/amplifier by means of a plug-in on the front of the driver/amplifier, and the driver/amplifier supplies the signal to piezoelectrics embedded in the composite fin lay-up.

The piezoelectrics are supplied with out-of-phase voltage, which causes one piezoelectric to expand and the other piezoelectric to contract; which in turn generates the driving moment that propels the beam.

1.6.5 Discussion of Results

The objective of this proof of concept was to develop a piezoelectric actuated composite fin that would oscillate underwater and may provide sufficient propulsive force. The setup was developed for the possibility that propulsive forces exist.

The first test was conducted out of water while the testing platform was clamped down. The testing platforms held the cantilevered, fixed, boundary condition well and the 0.305 meter piezoelectric actuated composite fin oscillated at its first natural frequency of 6.756 Hz in air. The maximum displacement, from stationary conditions, was on the order of 0.02 meters.

The second test was to submerge the setup and see how well the piezoelectric actuator moved the fin underwater. All electrical connections were coated with rubber cement, so the electrical energy was not released into the highly conductive water, carbon fiber platform, or metal frame of the tank. The 0.305 meter composite fin had a naturally occurring mode at

approximately 1 Hz (underwater). The voltage supplied was at 250 VPP and the maximum displacement, from stationary conditions was on the order of 0.01 meters.

Allowing the setup to run for more than 10 seconds produced a wave pattern in the tank, which was out-of-phase with the mode of vibration of the composite fin over time, thus causing the maximum amplitude of the free end to be hindered most significantly when the wave pattern was exactly out-of-phase from the input signal.

The conclusion is that the setup was successful in proving that the piezoelectric actuated composite fin would have underwater movement, however no forward motion was produced based on the observations of the test setup. The testing setup also allows future work to be conducted because two platforms were created where the second aluminum platform is made to travel 0.3 meters in the positive thrust direction.

1.7 Overview and Motivation for Present Work

This research is primarily concerned with constructing a FEA model of a beam immersed in a two-dimensional fluid and validation of a piezoelectric actuated marine propulsion fin that can be utilized on a small AUV (1 foot to 3 inches long). The fin consists of a fibrous composite thin flat plate and two piezoelectric actuators to produce an actuation effect like a bimetallic metal exhibits.

There are many reasons for using piezoelectrics for the present work and for AUVs. First, when coupled with large plates, the piezoelectric/plate setup has frequency ranges underwater that could be utilized on biomimetrically inspired small AUVs (~2-6Hz). Secondly, it was proven that using an inductor in parallel significantly reduces power requirements. This will provide for low power consumption, which in turn requires significantly less battery power, or weight, than previous AUV propulsion systems. Third, there is very low maintenance associated with the present work; there is no need to service any mechanical devices such as bearings, motors, or seals. Fourth, the fin is relatively inexpensive and can be manufactured efficiently and precisely. Fifth, the small AUV

concept, being depicted in this research, can be made neutrally buoyant in the water due to the fact that the fin is lightweight and the idea that all electrical components can be individually coated with a polymer to resist water. Finally, the piezoelectric propulsion system proposed in this research has little or no acoustic signature, making it ideal for reconnaissance or surveillance.

To analyze this experimental research project, simulations were developed using MATLAB software utilizing the finite element analysis technique and fluid structure interaction. The analysis was performed in the following 3 sections:

1) Two-dimensional fluid analysis development and verification
2) One-dimensional laminated piezoelectric-beam theory development and verification
3) Fluid-Structure Interaction (FSI)

Note that to complete the third section both the previous two sections have to be completed.

In the first section, the two-dimensional fluid MATLAB code is developed and verified in Chapters 2-6. Chapter 2 describes the general finite element method and the method is applied to fluid analysis. Chapter 3 solves a Stokes Flow problem and verifies the results with available analytical solutions. Chapter 4 develops solutions for a two-dimensional cavity flow problem for various Reynolds Numbers and verifies the cavity flow problem against published data. Chapter 5 develops a simulation of a transient plane jet flow problem and is verified with published and ANSYS 9.0 finite element software solutions. Chapter 6 develops some of the most current stability research for fluid analysis and compares the two most well-known methods.

In the second section, one-dimensional beam MATLAB code is developed and verified in Chapters 7-9. Chapter 7 develops the finite element theory and analysis involved with a one-dimensional Euler-Bernoulli beam and compares simulation results to published results. Chapter 8 develops the piezoelectric theory and explains important concepts of piezoelectric modeling. Chapter 9 combines Chapters 7 and 8 to develop the governing equations for a

laminated piezoelectric-beam element. Results obtained from Chapter 9 involve free vibration results and forced vibration results to obtain the natural frequencies of the laminated piezoelectric-beam.

In the third section a simplified fluid-structure interaction method is developed and velocity and pressure patterns are solved for. A major step forward in the fluid-structure interaction strategy is proposed that allows the fluid and the structure programs to be run within one program, rather than transferring loads between two programs, as most commercial packages currently do.

SECTION 1

2 Basic Concepts, Governing Equations and FE Formulation

Preface

By definition, a fluid is a material continuum that is unable to withstand a static shear stress. Unlike an elastic solid which responds to a shear stress with a recoverable deformation, a fluid responds with an irrecoverable flow. This section defines kinematic relationships, the governing equations and the finite element analysis associated with fluid motion.

2.1 Two-dimensional strain tensor and vorticity tensor formulation

The analysis of the motion of a fluid particle is analogous to the deformation of an elastic solid body. The fluid rate of strain and rate of rotation can be directly related to the strain and rigid body rotation of a solid. For fluid motion the velocity gradient is analogous to the displacement gradient of a solid. The velocity gradient is a second-order tensor defined in a Cartesian coordinate system by:

$$\nabla v = \begin{pmatrix} \frac{\partial v_1}{\partial x_1} & \frac{\partial v_1}{\partial x_2} & \frac{\partial v_1}{\partial x_3} \\ \frac{\partial v_2}{\partial x_1} & \frac{\partial v_2}{\partial x_2} & \frac{\partial v_2}{\partial x_3} \\ \frac{\partial v_3}{\partial x_1} & \frac{\partial v_3}{\partial x_2} & \frac{\partial v_3}{\partial x_3} \end{pmatrix}, \tag{2.1}$$

where $\underline{v}$ is the velocity and $\underline{x}$ is the axes orientation.

The velocity gradient may be broken down into its symmetric and anti-symmetric parts:

$$\frac{\partial v_i}{\partial x_j} = \frac{1}{2}\left(\frac{\partial v_i}{\partial x_j} + \frac{\partial v_j}{\partial x_i}\right) + \frac{1}{2}\left(\frac{\partial v_i}{\partial x_j} - \frac{\partial v_j}{\partial x_i}\right), \quad \text{for } i,j = \{1,2,3\} \tag{2.2}$$

Similar to the solid mechanics of an elastic body, the symmetric matrix on the left of Equation 2.2, is the rate of deformation, or rate of strain, tensor. Note that if the strain rate tensor is zero at a specific point, the region around that point is considered rigid body rotation. The anti-symmetric matrix, on the right, is called the vorticity tensor, or spin tensor. The vorticity vector can be associated with the vorticity equation, $\underline{\Omega} = \nabla \times \underline{v}$. Note that if the spin tensor is zero everywhere, the velocity flow field is irrotational [Donea and Huerta (2003)].

2.2 Formation of Stokes' law

Stress tensors describe the behavior of a body that does not depend on the coordinates used to measure it. The stress tensor is symmetric and can be decomposed into the sum of two symmetric tensors. There is a mean, or hydrostatic stress tensor, $-p\delta_{ij}$ which involves only expansion and contraction. Then there is a shear, or deviatoric stress tensor, s_{ij} which involves only shear stress.

$$\sigma_{ij} = -p\delta_{ij} + s_{ij}, \qquad \text{for i,j} = \{1,2,3\}, \tag{2.3}$$

where σ_{ij} is the stress, δ_{ij} is the Kronecker delta, and p is the pressure.

By definition a Newtonian fluid is a viscous fluid whose shear stresses are a linear function of the fluid strain rate, ε, expressed as:

$$s_{ij} = K_{ijpq}\varepsilon_{pq}, \qquad \text{for i,j,p,q} = \{1,2,3\}, \tag{2.4}$$

where s_{ij} is the shear stress, K_{ijpq} is the linear relationship between stress and strain and ε_{pq} is the fluid strain rate defined by the symmetric portion of the velocity gradient (Equation 2.2).

The stress-strain relationship for an incompressible Newtonian fluid is given by:

$$\sigma_{ij} = -p\delta_{ij} + s_{ij} = -p\delta_{ij} + \mu\left(\frac{\partial v_i}{\partial x_j} + \frac{\partial v_j}{\partial x_i}\right), \qquad \text{for i,j} = \{1,2,3\}, \tag{2.5}$$

where μ is the fluid dynamic viscosity. This is known as Stokes' Law [Donea and Huerta (2003)].

2.3 The Navier-Stokes equations

The Navier-Stokes equations are derived using the conservation of momentum and the conservation of mass is utilized to derive the incompressible Navier-Stokes Equations. Three assumptions the Navier-Stokes equations make are: the fluid is isothermal, it is continuous and the fields of interest like pressure, velocity, density and temperature, are differentiable. Also it is necessary to distinguish the domain, Ω, as a finite size and the boundary, Γ, must be Lipschitz continuous, which means it is a closed and sufficiently regular surface. The Navier-Stokes equations are defined by the following equations:

$$\rho\left(\dot{\underline{v}} + \left(\underline{v}\cdot\nabla\right)\underline{v}\right) = \nabla\cdot\underline{\underline{\sigma}} + \rho\underline{b}, \tag{2.6}$$

$$\nabla\cdot\underline{v} = 0, \tag{2.7}$$

where $\underline{v}$ is the velocity vector, ρ is the fluid density and $\underline{b}$ is the body force per unit mass vector on the fluid. Equation 2.6, referred to as the equation of motion, can be expressed in more convenient terms by substituting in Stokes' Law, Equation 2.5 to obtain Equation 2.8.

$$\dot{\underline{v}} + \left(\underline{v}\cdot\nabla\right)\underline{v} - \upsilon\nabla^2\underline{v} - \upsilon\nabla\left(\nabla\cdot\underline{v}\right) + \nabla p = \underline{b}, \tag{2.8}$$

where p is the kinematic pressure defined by pressure divided by density, and υ is the fluid kinematic viscosity equal to the fluid dynamic viscosity divided by the density. Equation 2.8 takes the form of the velocity-pressure stress-divergence equation.

The Navier Stokes equations can be expressed in Cartesian coordinates, shown in Equations 2.9, 2.10, 2.11.

$$\frac{\partial v_x}{\partial t} + \left(v_x \frac{\partial v_x}{\partial x} + v_y \frac{\partial v_x}{\partial y} \right) - \frac{\mu}{\rho} \left[2 \frac{\partial^2 v_x}{\partial x^2} + \frac{\partial}{\partial y} \left(\frac{\partial v_x}{\partial y} + \frac{\partial v_y}{\partial x} \right) \right] + \frac{\partial p}{\partial x} = b_x, \tag{2.9}$$

$$\frac{\partial v_y}{\partial t} + \left(v_x \frac{\partial v_y}{\partial x} + v_y \frac{\partial v_y}{\partial y} \right) - \frac{\mu}{\rho} \left[\frac{\partial}{\partial x} \left(\frac{\partial v_x}{\partial y} + \frac{\partial v_y}{\partial x} \right) + 2 \frac{\partial^2 v_y}{\partial y^2} \right] + \frac{\partial p}{\partial y} = b_y, \tag{2.10}$$

$$\frac{\partial v_x}{\partial x} + \frac{\partial v_y}{\partial y} = 0, \tag{2.11}$$

where t is time.

Notice that the velocity-pressure stress-divergence equation can be reduced by the incompressibility condition to Equation 2.12 (The fluid is considered incompressible, or mathematically the divergence is zero: $(\nabla \cdot \underline{v}) = 0$).

$$\dot{\underline{v}} + (\underline{v} \cdot \nabla)\underline{v} - \upsilon \nabla^2 \underline{v} + \nabla p = \underline{b}, \tag{2.12}$$

The Navier-Stokes equations must also have appropriate initial and boundary conditions applied, to be solved. Normally boundary conditions specify either the velocity component (Dirichlet or essential boundary conditions) or the traction component (Neumann or natural boundary conditions) at each point on the boundary. The traction components, $\underline{T}$, can be mathematically represented by:

$$\hat{n} \cdot \underline{\sigma} = -p + 2\upsilon \hat{n} \cdot \frac{1}{2} \left(\frac{\partial v_i}{\partial x_j} + \frac{\partial v_j}{\partial x_i} \right) = \underline{T}_{\hat{n}}, \qquad \text{for i,j} = \{1,2,3\}, \tag{2.13}$$

where $\hat{n}$ is the unit normal on the boundary.

Figure 16 shows the relationship between global (x,y) coordinates and (n,τ) coordinates.

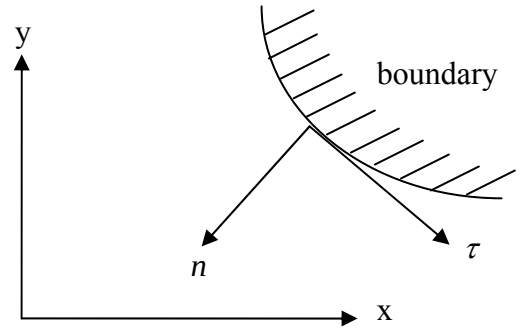

Figure 16: Coordinate systems (x,y) and (n, τ)

With reference to local Cartesian axes (n,τ) the traction equations are:

$$T_n = -p + 2\upsilon \frac{\partial v_n}{\partial n}, \tag{2.14}$$

$$T_\tau = v\left(\frac{\partial v_\tau}{\partial n} + \frac{\partial v_n}{\partial \tau} \right), \tag{2.15}$$

Also in the case of time-dependent problems, the initial value of the velocity field must be given.

It is important to note three specific features of the Navier Stokes equation. The first is that no initial condition is needed for the fluid pressure because there is no time-derivative of the pressure in the governing equation. With the use of Dirichlet boundary conditions, pressure is only represented as a gradient through the Navier-Stokes equations. Therefore it is customary to assign a specific value, or possibly the mean value, to a specific point of reference for all the other points. Secondly in the case of highly viscous flows, the convective term $(v \cdot \nabla)v$ often can be neglected because the inertial effects are not as responsible for fluid interaction as the viscous effects; this is considered Stokes Flow. Lastly the Navier-Stokes equations can be represented non-dimensionally by using the inverse of

the Reynolds number to replace the viscosity term understanding that V_{char} and L_{char} are unity [Donea and Huerta (2003)].

2.4 Finite Element Formulation using Galerkin's Method

The finite element method provides approximate solutions for boundary value problems. In the finite element method, a given domain, or region over which the problem is solved, is viewed as a collection of sub domains, similar to finite difference. Over each sub domain the governing differential equation that represents that domain is approximated by any of the traditional variational methods. Breaking up the domain into smaller sub domains allows a complicated function to be represented by simpler polynomials.

Classical finite element analysis consists of three main features:

1) Element choice and interpolation function generation
2) Discretization of governing equations through a traditional variational method
3) Assembly of element equations into matrix format and obtaining a solution

An element, in finite element analysis, is defined as a sub domain of the original domain. It represents a local domain in which the governing equations, of the complete domain, are upheld. Each element is distinguished by a series of nodes, which are representations of discrete points on the given domain. Elements are connected together between their connective boundaries, or sides, which are defined by the nodes. At a node, the solution must be continuous with respect to the neighboring element's nodal solution and possibly its derivatives dependent on the chosen order of the polynomials, or interpolation functions selected to represent the elements. The collection of all of these finite elements and nodes is called the mesh.

The element choice for any mesh depends primarily on the domain that is being represented and the tolerance of approximation that is allowed between the exact solution

and the finite element solution. Therefore using more elements and/or more nodes will result in a higher tolerance between the exact solution and the finite element solution.

Almost all approximation methods used to determine the solution of differential and/or integral equations, approximate the dependent variable, u, by piecewise polynomials, $\tilde{u}_e$, seen in Equation 2.16.

$$u(\underline{x}) \approx \sum_{e=1}^{N_{elem}} \tilde{u}_e(x), \tag{2.16}$$

where e represents the number of elements, or sub-domains, being used.

Each piecewise polynomial is expressed by a summation of a homogeneous part $\sum U_j \Psi_j(\underline{x})$ and a non-homogeneous part $\Psi_0(\underline{x})$. It is required that the non-homogenous part satisfy the specified essential boundary conditions and the homogenous part vanishes at the coinciding boundary position.

$$\tilde{u}_e(x) = \sum_{j=1}^{N} U_j \Psi_j(x) + \Psi_0(x), \tag{2.17}$$

where $\tilde{u}_e$ represents the approximation solution, which is the linear combination of unknown parameters, U_j, and known functions, Ψ_j, of position x in the domain, Ω, on which the problem is stated. Ψ are called the interpolation functions, or shape functions in solid body mechanics. Determining the unknown parameters, U_j, is what determines $\tilde{u}_e$.

To determine the unknown parameters, U_j, a variational method called the weighted residual method, is implemented. In the weighted-residual method, the unknown parameters, U_j, are found using the weighted-integral form of the governing equations. This process can be broken down into three steps:

- First the weighted-integral form of the governing equations is found by introducing the approximations for the unknown parameters into the partial differential equation, A, set equal to the forcing function, F.

$$A(\tilde{u}_e) = F, \tag{2.18}$$

The residual, R, is identified as the difference between the approximate solution, $A(\tilde{u}_e)$, and the exact solution, F. This term is not zero due to the approximation of u.

$$R \equiv A(\tilde{u}_e) - F \neq 0, \tag{2.19}$$

- Second a weighting function, $w(x)$, is multiplied by the residual and integrated over the stated sub-domain. This integration is set equal to zero because it is essentially setting the error, or residual of the approximations and the weighting function to zero. This finds the unknown parameters, U_j, that minimize the error associated in the approximation.

$$\int_{\Omega_e} w(x) R \, d\Omega = 0, \tag{2.20}$$

- Last the expression is integrated by parts to produce the "weak form". The weak form allows distribution of the differentiation between the approximate solution and the weight function. It also includes the essential and natural boundary conditions necessary to solve the problem.

As an example, the process of constructing the weak form of a governing differential equation using the weighted-residual method is applied to the x-direction Navier-Stokes Cartesian equation (Equation 2.9).

- $$\rho\frac{\partial\tilde{v}_x}{\partial t}+\rho\left(\tilde{v}_x\frac{\partial\tilde{v}_x}{\partial x}+\tilde{v}_y\frac{\partial\tilde{v}_x}{\partial y}\right)-\mu\left[2\frac{\partial^2\tilde{v}_x}{\partial x^2}+\frac{\partial}{\partial y}\left(\frac{\partial\tilde{v}_x}{\partial y}+\frac{\partial\tilde{v}_y}{\partial x}\right)\right]+\frac{\partial\tilde{p}}{\partial x}=f_x,$$

$$where: v_x\approx\tilde{v}_x=\sum_{j=1}^{N}c_j\Psi_{1,j}(\underline{x})+\Psi_{1,0}(\underline{x}),\quad v_y\approx\tilde{v}_y=\sum_{j=1}^{N}d_j\Psi_{2,j}(\underline{x})+\Psi_{2,0}(\underline{x}),$$

$$p\approx\tilde{p}=\sum_{j=1}^{N}e_j\Psi_{3,j}(\underline{x})+\Psi_{3,0}(\underline{x}),$$

$$R\equiv\rho\frac{\partial\tilde{v}_x}{\partial t}+\rho\left(\tilde{v}_x\frac{\partial\tilde{v}_x}{\partial x}+\tilde{v}_y\frac{\partial\tilde{v}_x}{\partial y}\right)-\mu\left[2\frac{\partial^2\tilde{v}_x}{\partial x^2}+\frac{\partial}{\partial y}\left(\frac{\partial\tilde{v}_x}{\partial y}+\frac{\partial\tilde{v}_y}{\partial x}\right)\right]+\frac{\partial\tilde{p}}{\partial x}-f_x\neq 0, \tag{2.21}$$

- $$\int_{\Omega_e}w_1\left\{\rho\frac{\partial\tilde{v}_x}{\partial t}+\rho\left(\tilde{v}_x\frac{\partial\tilde{v}_x}{\partial x}+\tilde{v}_y\frac{\partial\tilde{v}_x}{\partial y}\right)-\mu\left[2\frac{\partial^2\tilde{v}_x}{\partial x^2}+\frac{\partial}{\partial y}\left(\frac{\partial\tilde{v}_x}{\partial y}+\frac{\partial\tilde{v}_y}{\partial x}\right)\right]+\frac{\partial\tilde{p}}{\partial x}-f_x\right\}dxdy=0, \tag{2.22}$$

- Integration by parts is executed.

  Note that it is not shown here so that the Galerkin method can be implemented below.

The Galerkin method of solving partial differential equations is a special case of the weighted residual method where the weighting function, w_j, is chosen to be equal to the approximation function, Ψ_j.

Using the Galerkin method for the Navier-Stokes governing differential equations (Equations 2.9, 2.10 and 2.11) the weighted-integral formulations are:

$$\int_{\Omega_e} \Psi_1 \left\{ \rho \frac{\partial \tilde{v}_x}{\partial t} + \rho \left(\tilde{v}_x \frac{\partial \tilde{v}_x}{\partial x} + \tilde{v}_y \frac{\partial \tilde{v}_x}{\partial y} \right) - \mu \left[2 \frac{\partial^2 \tilde{v}_x}{\partial x^2} + \frac{\partial}{\partial y} \left(\frac{\partial \tilde{v}_x}{\partial y} + \frac{\partial \tilde{v}_y}{\partial x} \right) \right] + \frac{\partial \tilde{p}}{\partial x} - f_x \right\} dxdy = 0, \tag{2.23}$$

$$\int_{\Omega_e} \Psi_2 \left\{ \rho \frac{\partial \tilde{v}_y}{\partial t} + \rho \left(\tilde{v}_x \frac{\partial \tilde{v}_y}{\partial x} + \tilde{v}_y \frac{\partial \tilde{v}_y}{\partial y} \right) - \mu \left[\frac{\partial}{\partial x} \left(\frac{\partial \tilde{v}_x}{\partial y} + \frac{\partial \tilde{v}_y}{\partial x} \right) + 2 \frac{\partial^2 \tilde{v}_y}{\partial y^2} \right] + \frac{\partial \tilde{p}}{\partial y} - f_y \right\} dxdy = 0, \tag{2.24}$$

$$\int_{\Omega_e} \Psi_3 \left\{ \frac{\partial \tilde{v}_x}{\partial x} + \frac{\partial \tilde{v}_y}{\partial y} \right\} dxdy = 0, \tag{2.25}$$

where Ψ_1 can be interpreted as the weighting function associated with v_x, Ψ_2 is associated with v_y, and Ψ_3 is associated with the pressure. Note that Equations 2.22 is represented using the Galerkin method as Equation 2.23.

By integrating Equations 2.23, 2.24 and 2.25 by parts and using the Green-Gauss theorem, the weak form is generated.

$$\int_{\Omega_e} \left\{ \rho \Psi_1 \frac{\partial \tilde{v}_x}{\partial t} + \rho \Psi_1 \left(\tilde{v}_x \frac{\partial \tilde{v}_x}{\partial x} + \tilde{v}_y \frac{\partial \tilde{v}_x}{\partial y} \right) - \mu \left[2 \frac{\partial \Psi_1}{\partial x} \frac{\partial \tilde{v}_x}{\partial x} + \frac{\partial \Psi_1}{\partial y} \left(\frac{\partial \tilde{v}_x}{\partial y} + \frac{\partial \tilde{v}_y}{\partial x} \right) \right] + \frac{\partial \Psi_1}{\partial x} \tilde{p} - \Psi_1 f_x \right\} dxdy + \oint_{\Gamma_e} \Psi_1 (T_x) = 0, \tag{2.26}$$

$$\int_{\Omega_e} \left\{ \rho \Psi_2 \frac{\partial \tilde{v}_y}{\partial t} + \rho \Psi_2 \left(\tilde{v}_x \frac{\partial \tilde{v}_y}{\partial x} + \tilde{v}_y \frac{\partial \tilde{v}_y}{\partial y} \right) - \mu \left[\frac{\partial \Psi_2}{\partial x} \left(\frac{\partial \tilde{v}_x}{\partial y} + \frac{\partial \tilde{v}_y}{\partial x} \right) + 2 \frac{\partial \Psi_2}{\partial y} \frac{\partial \tilde{v}_y}{\partial y} \right] + \frac{\partial \Psi_2}{\partial y} \tilde{p} - \Psi_2 f_y \right\} dxdy + \oint_{\Gamma_e} \Psi_2 (T_y) = 0, \tag{2.27}$$

$$\int_{\Omega_e} \Psi_3 \left\{ \frac{\partial \tilde{v}_x}{\partial x} + \frac{\partial \tilde{v}_y}{\partial y} \right\} dxdy = 0, \tag{2.28}$$

An important part associated with this step in the finite element formulation is to identify the natural, or Neumann, type boundary conditions (NBC) and essential, or Dirichlet, boundary conditions (EBC). Depending on the form of the weak formulation, it can be possible to explain the types of boundary conditions needed to solve a set of governing

equations. Examining the weak formulation, the EBCs are identified as being the same order as the weighting function in the domain integrals. The NBCs are of different order than the weighting function and are normally found in the boundary integrals, denoted with Γ. For Equations 2.26, 2.27, and 2.28, the EBCs are expressed as v_x and v_y and the NBCs are expressed in terms of the tractions, T_x and T_y.

A good discussion about Equation 2.28, is presented by Reddy (2006). It states that that there is no boundary integral involving Ψ_3 because no integration by parts is used. This then implies that p is not a primary variable, but part of the secondary variables, T_x and T_y. Due to this, it is not necessary for the pressure to be continuous along the element boundaries. Meaning the pressure discretization does not have to line up with the velocity discretization. Also it is known that if $\tilde{p}$ is not specified, but the other secondary variables are, then $\tilde{p}$ is arbitrarily set to a value at some point. Therefore p can only be determined within a given arbitrary constant. Additionally the minus sign in the third equation is there to make the resulting model symmetric [Reddy (2006)].

Due to the fact that the pressure and velocity discretizations do not have to be the same and that Ψ_0 will be satisfied by the NBCs and the EBCs, the following approximations will be used:

$$v_x \approx \tilde{v}_x = \sum_{j=1}^{n} v_{x,j}\Psi_j(\underline{x}), \quad v_y \approx \tilde{v}_y = \sum_{j=1}^{n} v_{y,j}\Psi_j(\underline{x}), \quad p \approx \tilde{p} = \sum_{J=1}^{m} p_J \Phi_J(\underline{x}), \tag{2.29}$$

where Ψ_j (j = 1,2,…n) and Φ_J (J = 1,2,…m) are interpolation functions of different order and $v_{x,j}$ and $v_{y,j}$ and p_J are nodal values for the velocity and pressure respectfully.

Following the discretization of the governing equations, which were represented as the Navier-Stokes equations, through a traditional variational method, discussed as the Galerkin method, the equations must be assembled into a matrix format.

Substituting in the approximation solutions, Equations 2.29, the full finite element equations arranged in matrix form are:

$$\begin{bmatrix} 2[K^{11}]+[K^{22}]+[C_v^{11}] & [K^{21}]+[C_v^{12}] & -[K^{10}] \\ [K^{12}]+[C_v^{21}] & [K^{11}]+2[K^{22}]+[C_v^{22}] & -[K^{20}] \\ -[K^{10}]^T & -[K^{20}]^T & [0] \end{bmatrix} \begin{Bmatrix} \{v_x\} \\ \{v_y\} \\ \{P\} \end{Bmatrix} + \begin{bmatrix} [\hat{M}] & [0] & [0] \\ [0] & [\hat{M}] & [0] \\ [0] & [0] & [0] \end{bmatrix} \begin{Bmatrix} \{\dot{v}_x\} \\ \{\dot{v}_y\} \\ \{\dot{P}\} \end{Bmatrix} = \begin{Bmatrix} \{F^1\} \\ \{F^2\} \\ \{0\} \end{Bmatrix}, \tag{2.30}$$

The coefficient matrices shown are defined as:

$$\begin{aligned} \hat{M}_{ij} &= \int_{\Omega_e} \rho \Psi_i^e \Psi_j^e \, dxdy \\ K_{ij}^{\alpha\beta} &= \int_{\Omega_e} \mu \frac{\partial \Psi_i^e}{\partial x_\alpha} \frac{\partial \Psi_j^e}{\partial x_\beta} \, dxdy \\ K_{iJ}^{\alpha 0} &= \int_{\Omega_e} \mu \frac{\partial \Psi_i^e}{\partial x_\alpha} \Phi_J \, dxdy \\ C_v^{\alpha\beta} &= \int_{\Omega_e} \rho \Psi_i^e \Psi_j^e \frac{\partial v_\alpha}{\partial x_\beta} \, dxdy \\ F^1 &= \int_{\Omega_e} \Psi_i^e f_x \, dxdy + \oint_{\Gamma_e} \Psi_i^e t_x \, ds \\ F^2 &= \int_{\Omega_e} \Psi_i^e f_y \, dxdy + \oint_{\Gamma_e} \Psi_i^e t_y \, ds \end{aligned} \tag{2.31}$$

Equation 2.30 can assume the following partitioned form:

$$\begin{pmatrix} [K]+[C] & [G] \\ [G]^T & 0 \end{pmatrix} \begin{pmatrix} \underline{v} \\ \underline{p} \end{pmatrix} + \begin{pmatrix} [M] & 0 \\ 0 & 0 \end{pmatrix} \begin{pmatrix} \underline{\dot{v}} \\ \underline{\dot{p}} \end{pmatrix} = \begin{pmatrix} \underline{f} \\ 0 \end{pmatrix}, \tag{2.32}$$

$$K = \begin{bmatrix} 2[K^{11}] + [K^{22}] & [K^{21}] \\ [K^{12}] & [K^{11}] + 2[K^{22}] \end{bmatrix}$$
$$C = \begin{bmatrix} [C_v^{11}] & [C_v^{12}] \\ [C_v^{21}] & [C_v^{22}] \end{bmatrix}$$
$$G = \begin{bmatrix} -[K^{10}] \\ -[K^{20}] \end{bmatrix}$$
$$M = \begin{bmatrix} [\hat{M}] & [0] \\ [0] & [\hat{M}] \end{bmatrix}$$

(2.33)

where [K] represents the viscous term, [C] represents the convective term, [G] represents the off-diagonal viscous terms, $\underline{v}$ is the nodal velocity vectors, $\underline{p}$ is the nodal pressure vector, [M] is the mass term dealing with density, and $\underline{f}$ is the body force array. This partitioned form is essential to solving for the approximations of the unknown variables: v_x, v_y and p [Reddy 2006].

2.5 Isoparametric Elements: Choice of the Master Element – Q2Q1

An accurate representation of irregular domains, curved boundaries, can be accomplished by utilizing a strength of finite element analysis; the ability to use irregularly shaped curvilinear elements. For example, a distorted region composed of many curved boundaries can not be represented well using just rectangular elements, there will always be a finite distance, or error, between the rectangular element and the distorted boundary. Figure 17 shows the concept of using irregularly shaped curvilinear elements versus rectangular elements on a curved boundary.

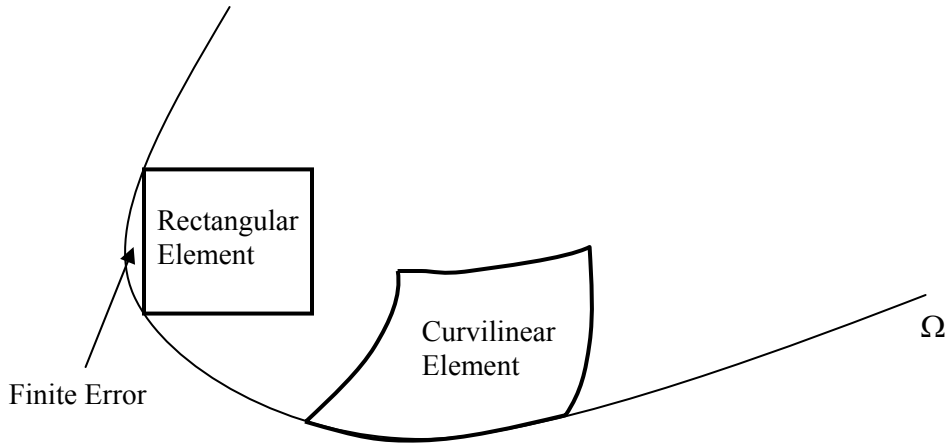

Figure 17: Difference between a rectangular element and a curvilinear element

Due to the fact that interpolation functions are easily derived for a rectangular element and it is easier to evaluate the weak form integrals over rectangular geometries, a transform must be determined to deal with the curvilinear element, or isoparametric element, dimensions that will be mapped to rectangular element dimensions.

The rectangular element, that the isoparametric element is mapped to, is called the "master" element. For rectangular elements, it has dimensions $(-1 \le (\xi,\eta) \le 1)$, where (ξ,η) are the local curvilinear coordinate axes. The rectangular element dimensions can be chosen arbitrarily for mapping, but -1 and 1 are easiest to integrate between, therefore higher computational efficiency is obtained. After the transformation to the master element occurs, the integral of the weak form can be easily analyzed. The result is then mapped back to the original set of coordinates, or the distorted shape.

The coordinate transformation between the domain of the element, Ω_e, and the domain of the master element $\hat{\Omega}$, is accomplished using a coordinate transformation of the form:

$$x = \sum_{j=1}^{m} x_j^e \hat{\Psi}_j^e(\xi,\eta), \quad y = \sum_{j=1}^{m} y_j^e \hat{\Psi}_j^e(\xi,\eta), \tag{2.34}$$

where $\hat{\Psi}_j^e$ are the interpolation functions of the master element domain. Figure 18 graphically shows the mapping between an isoparametric element on the left-hand side (LHS) in global x and y coordinates to the master element on the right-hand side (RHS).

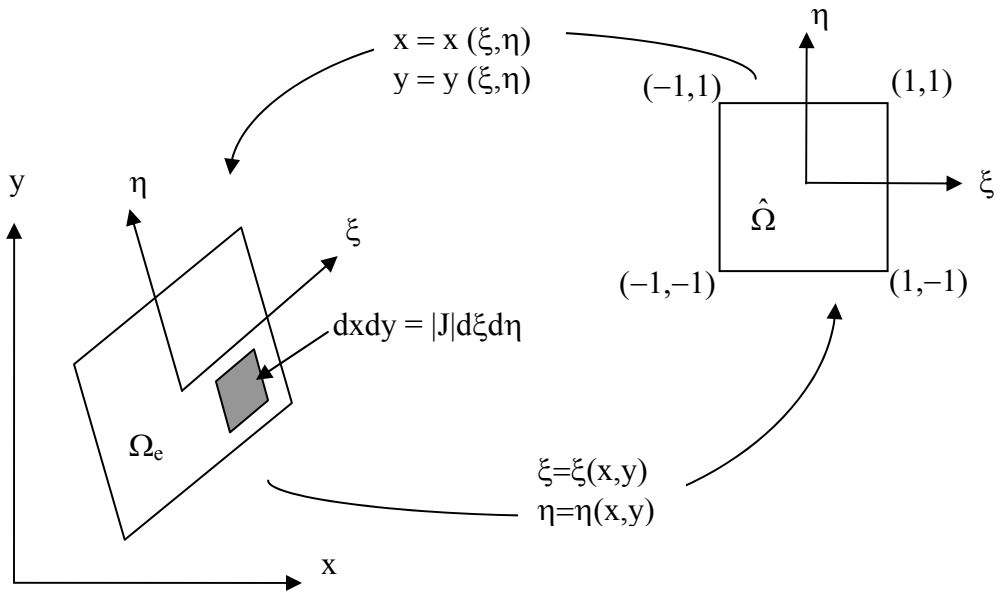

Figure 18: Coordinate transformation from isoparametric element (LHS) of a mesh to master rectangular element (RHS)

It should be noted that the reason for a transformation from the global coordinates to the master coordinates is just for numerical calculation. The resulting algebraic equations from a transformation are always in terms of the nodal values of the original physical domain.

The integral statements, i.e. Equations 2.31, are in terms of the global coordinates and some expressions have derivatives with respect to the global coordinates. The derivatives of the global coordinates must be related to the derivatives of the master element coordinates (ξ,η) using the transform expressed in Equation 2.34. Using the chain rule of partial differentiation the resulting transformation is:

$$\frac{\partial \Psi_i^e}{\partial \xi} = \frac{\partial \Psi_i^e}{\partial x}\frac{\partial x}{\partial \xi} + \frac{\partial \Psi_i^e}{\partial y}\frac{\partial y}{\partial \xi},$$
$$\frac{\partial \Psi_i^e}{\partial \eta} = \frac{\partial \Psi_i^e}{\partial x}\frac{\partial x}{\partial \eta} + \frac{\partial \Psi_i^e}{\partial y}\frac{\partial y}{\partial \eta}, \qquad (2.35)$$

These relationships can be stated in matrix format by:

$$\begin{Bmatrix} \frac{\partial \Psi_i^e}{\partial \xi} \\ \frac{\partial \Psi_i^e}{\partial \eta} \end{Bmatrix} = \begin{bmatrix} \frac{\partial x}{\partial \xi} & \frac{\partial y}{\partial \xi} \\ \frac{\partial x}{\partial \eta} & \frac{\partial y}{\partial \eta} \end{bmatrix}^e \begin{Bmatrix} \frac{\partial \Psi_i^e}{\partial x} \\ \frac{\partial \Psi_i^e}{\partial y} \end{Bmatrix} \equiv [J] \begin{Bmatrix} \frac{\partial \Psi_i^e}{\partial x} \\ \frac{\partial \Psi_i^e}{\partial y} \end{Bmatrix}, \tag{2.36}$$

where [*J*] represents the coordinate transform, referred to as the Jacobian matrix.

It is also necessary to represent the boundary of the integral in terms of the mapped coordinates. That can be done through the following transformation:

$$dxdy = |J| d\xi d\eta, \tag{2.37}$$

where $|J|$ is the determinant of the Jacobian matrix.

Equations 2.36 and 2.37 allow each isoparametric element to be mapped to a master element domain to be easily integrated. The choice of the master element is the next logical step.

The master element chosen for the fluid analysis is the Q2Q1 element. The Q2Q1 element is a Taylor-Hood element, which has continuous biquadratic velocity and continuous bilinear pressure. Figure 19 displays the Q2Q1 element where the black dots represent the local nodes of velocity and the circles represent the local nodes of pressure. The local axes of (ξ, η) and the local node numbering is shown in Figure 19.

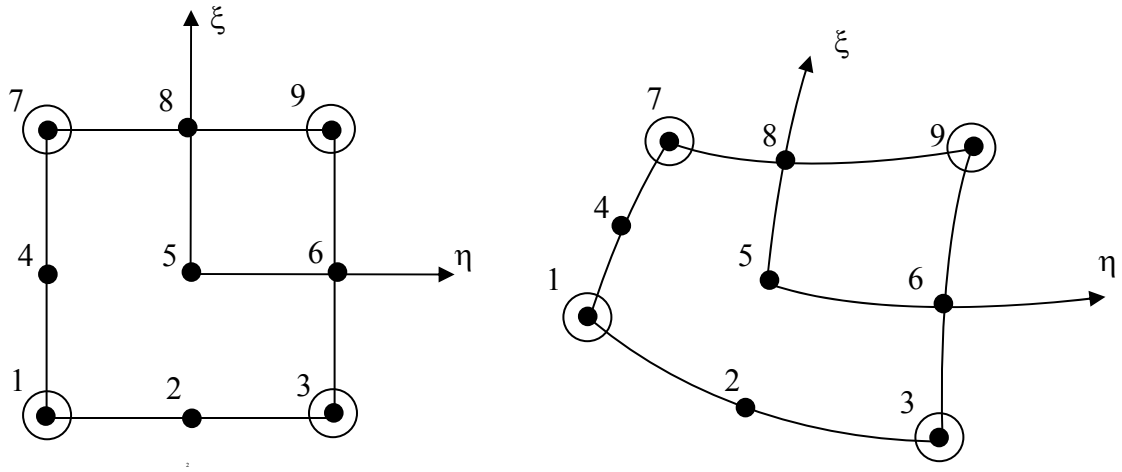

Figure 19: Master element Q2Q1 in rectangular (LHS) and isoparametric (RHS) elements

The Q2Q1 element is known to provide a guaranteed existence and unique solution for fluid analysis due to its adherence to the Ladyzhenskaya-Babuška-Brezzi (LBB) compatibility condition [Ladyzhenskaya(1969), Babuška (1970/71) and Brezzi(1974)]. Basically satisfying this condition causes an important matrix ($G^TK^{-1}G$) in solving fluid finite element problems to always be positive definite and also the partitioned matrix of $\begin{pmatrix} [K]+[C] & [G] \\ [G]^T & 0 \end{pmatrix}$ to be non-singular. It is also important to use a LBB compliant element when solving incremental schemes, such as transient problems [Guermond and Quartapelle (1998)]. Since the fluid research conducted uses transient schemes, the Q2Q1 element was beneficial.

Using the Galerkin method of the finite element formulation, the interpolation functions must be found for the Q2Q1 element because they are used as the approximating function and the weighting function. The interpolation functions are found by using portions of the first five tiers of Pascal's triangle, shown below, as the interpolating polynomial.

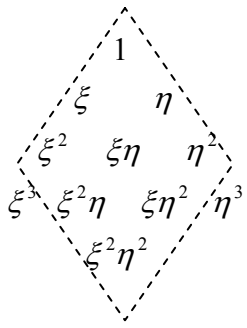

Thus the polynomial is defined using coefficients in front of each of Pascal's triangle terms as:

$$v_i^e = a_0 + a_1\xi + a_3\eta + a_4\xi\eta + a_5\xi^2 + a_6\eta^2 + a_7\xi^2\eta + a_8\xi\eta^2 + a_9\xi^2\eta^2, \qquad (2.38)$$

where v_i^e defines the nodal velocities of the element

Formulating nine equations that satisfy Equation 2.38, will construct a system of equations that have the following form:

$$\{v_i^e\} = [A]\{a_i\}, \qquad (2.39)$$

The inverse of [A] becomes the coefficients of the interpolation function by the subsequent proof (2.40).

$$\begin{aligned}
&\{v_i^e\} = [A]\{a_i\},\\
&So:\ \{a_i\} = [A]^{-1}\{v_i^e\},\\
&Since:\ \{v_i^e\} = \{1\ \ \xi_i\ \ \eta_i\ \ \xi_i\eta_i\ \ \xi_i^2\ \ \eta_i^2\ \ \xi_i^2\eta_i\ \ \xi_i\eta_i^2\ \ \xi_i^2\eta_i^2\}\{a_i\},\\
&\{v_i^e\} = \{1\ \ \xi_i\ \ \eta_i\ \ \xi_i\eta_i\ \ \xi_i^2\ \ \eta_i^2\ \ \xi_i^2\eta_i\ \ \xi_i\eta_i^2\ \ \xi_i^2\eta_i^2\}[A]^{-1}\{v_i^e\} = \sum_{i=1}^{9}\Psi_i^e v_i^e,\\
&\therefore \Psi_i^e = \{1\ \ \xi_i\ \ \eta_i\ \ \xi_i\eta_i\ \ \xi_i^2\ \ \eta_i^2\ \ \xi_i^2\eta_i\ \ \xi_i\eta_i^2\ \ \xi_i^2\eta_i^2\}[A]^{-1},
\end{aligned} \qquad (2.40)$$

The resulting interpolation functions for a Q2Q1 element for the velocity nodes in terms of its local coordinates, ξ and η, are:

$$\Psi_1^e = \frac{1}{4}(\xi - \xi^2)(\eta - \eta^2), \quad \Psi_2^e = -\frac{1}{2}(1 - \xi^2)(\eta - \eta^2), \quad \Psi_3^e = -\frac{1}{4}(\xi + \xi^2)(\eta - \eta^2),$$
$$\Psi_4^e = -\frac{1}{2}(\xi - \xi^2)(1 - \eta^2), \quad \Psi_5^e = (1 - \xi^2)(1 - \eta^2), \quad \Psi_6^e = \frac{1}{2}(\xi + \xi^2)(1 - \eta^2),$$
$$\Psi_7^e = -\frac{1}{4}(\xi - \xi^2)(\eta + \eta^2), \quad \Psi_8^e = \frac{1}{2}(1 - \xi^2)(\eta + \eta^2), \quad \Psi_9^e = \frac{1}{4}(\xi + \xi^2)(\eta + \eta^2), \tag{2.41}$$

Figure 20 graphically represents the velocity interpolation functions where 'Z' = ξ and 'n' = η.

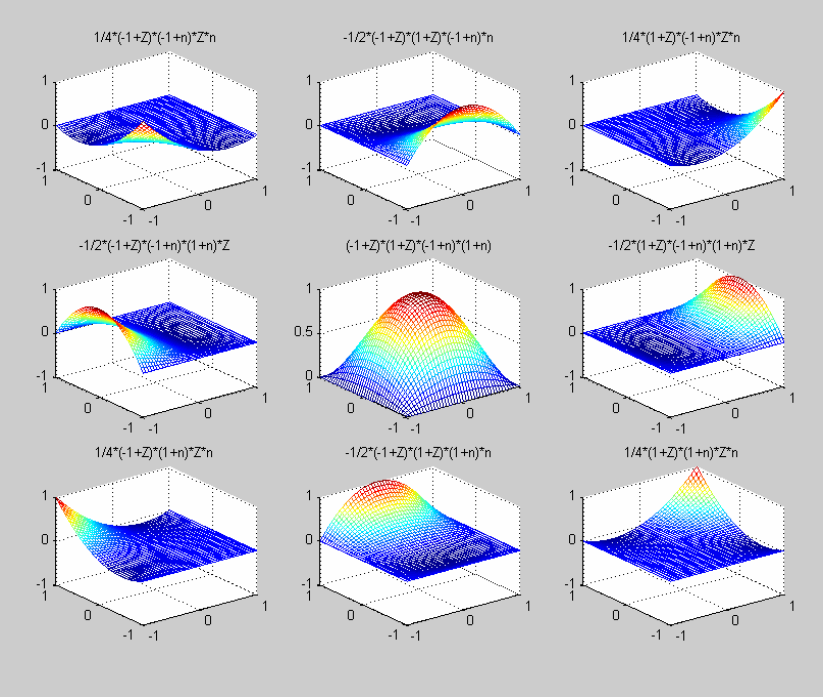

Figure 20: Graphical representation of velocity interpolation functions

Due to the fact that the pressure does not need to follow the same interpolation functions as the velocity, the interpolation functions for the pressure nodes in terms of its local coordinates, ξ and η, are:

$$\Phi_1^e = \frac{1}{4}(1-\xi)(1-\eta),\ \ \Phi_2^e = \frac{1}{4}(1+\xi)(1-\eta),$$
$$\Phi_3^e = \frac{1}{4}(1-\xi)(1+\eta),\ \ \Phi_4^e = \frac{1}{4}(1+\xi)(1+\eta), \qquad (2.42)$$

Figure 21 graphically represents the pressure interpolation functions where 'Z' = ξ and 'n' = η [Reddy 2006].

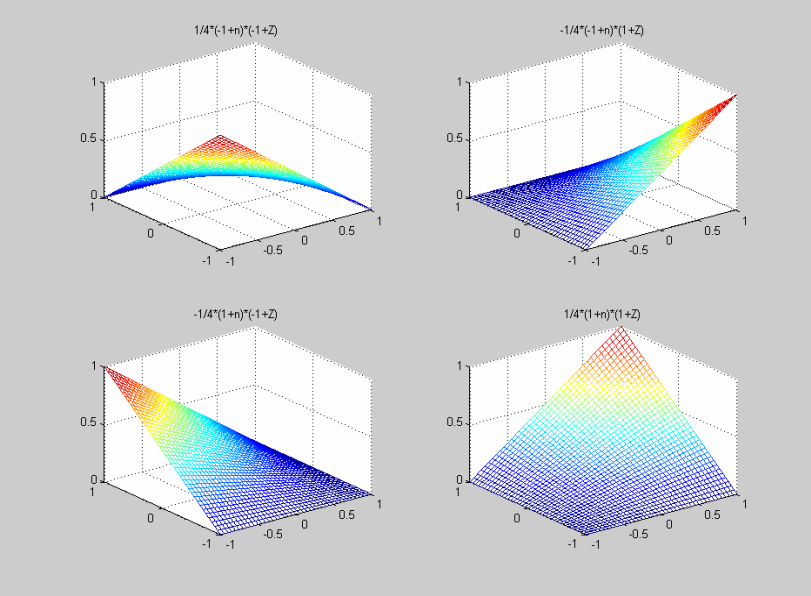

Figure 21: Graphical representation of velocity shape functions

In this chapter the classical formulation of a finite element analysis was discussed in depth. The finite element governing equations for fluid analysis have been established as the Navier-Stokes equations and the discretization of these equations have been accomplished by the Galerkin weighted residual method, Equations 2.26, 2.27, 2.28. The Q2Q1 element, Figure 19, has been chosen as the master element for the finite element mesh. Finally the assembly of these discretized equations is represented in matrix format as Equation 2.32.

The next three chapters validate MATLAB code created to simulate three important fluid dynamics problems. The three problems are Stokes Flow, stationary Navier-Stokes cavity flow and transient Navier-Stokes flow.

3 Stokes Flow Problem

Preface

A Stokes Flow problem refers to a type of flow where the inertial forces are small compared to the viscous forces. For this particular problem a Newtonian, low-speed, viscous, incompressible fluid will be analyzed using the Navier-Stokes equations and the results compared to analytical published results.

3.1 Stokes Flow Problem Definition

The problem is a stationary Stokes Flow problem over the domain, Ω = [0:1,0:1]. The viscosity, $\upsilon = 1$, the density, $\rho = 1$, and the mesh is made up of a 10 X 10 element mesh of Q2Q1 elements. All boundary conditions are fixed, which are Dirichlet boundary conditions. The given body forces are:

$$\begin{aligned} b_1 &= (12-24y)x^4 + (-24+48y)x^3 + (-48y+72y^2-48y^3+12)x^2 \\ &\quad + (-2+24y-72y^2+48y^3)x + 1 - 4y + 12y^2 - 8y^3, \\ b_2 &= (8-48y+48y^2)x^3 + (-12+72y-72y^2)x^2 \\ &\quad + (4-24y+48y^2-48y^3+24y^4)x - 12y^2 + 24y^3 - 12y^4, \end{aligned} \tag{3.1}$$

The Stokes Flow equations are simplified Navier-Stokes equations; the inertial, or non-linear, term is negligible compared to the viscous term. The Stokes Flow equations are shown in Equation 3.2.

$$\begin{aligned} &\upsilon\nabla^2\underline{v} + \nabla p = \underline{b} \quad in\ \Omega, \\ &\nabla\cdot\underline{v} = 0 \qquad in\ \Omega, \\ &\underline{v} = 0 \qquad on\ \Gamma, \end{aligned} \tag{3.2}$$

The resulting partitioned form of the finite element matrix, neglecting the non-linear or convective matrix, then becomes:

$$\begin{pmatrix} [K] & [G] \\ [G]^T & 0 \end{pmatrix} \begin{pmatrix} \underline{v} \\ \underline{p} \end{pmatrix} = \begin{pmatrix} \underline{f} \\ 0 \end{pmatrix}, \tag{3.3}$$

3.2 Simulation Results and Comparison

Using MATLAB software the problem was coded, Appendix B.1, solved, and results were obtained for the velocity field, Figure 22, and the pressure field, Figure 23.

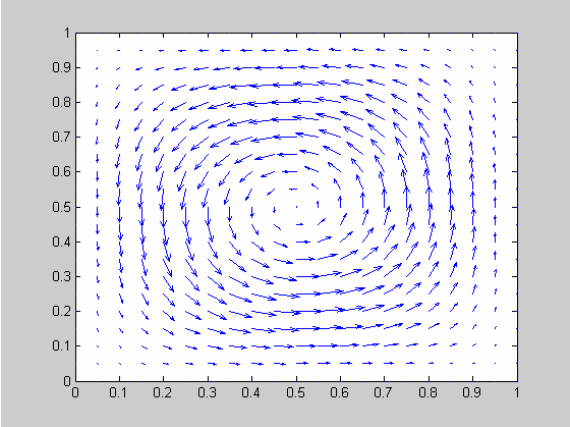

Figure 22: MATLAB simulation results for the velocity field

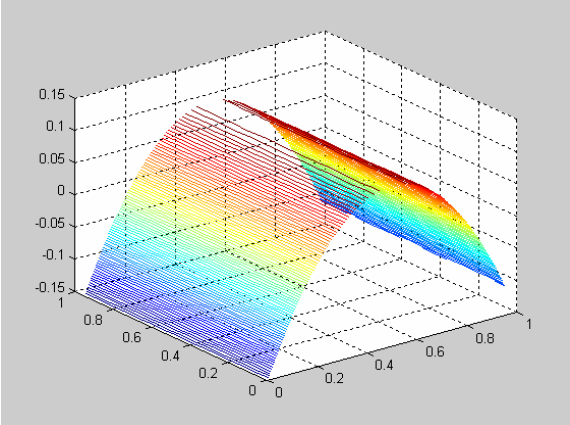

Figure 23: MATLAB simulation results for the pressure field

The exact analytical solution, with the same body forces, can be solved for the velocity field and pressure field components:

$$\begin{aligned} v_1(x,y) &= x^2(1-x)^2\left(2y-6y^2+4y^3\right), \\ v_2(x,y) &= -y^2(1-y)^2\left(2x-6x^2+4x^3\right), \\ p(x,y) &= x(1-x), \end{aligned} \tag{3.4}$$

Graphically those results are displayed in Figures 24 and 25 as the velocity field and pressure respectively.

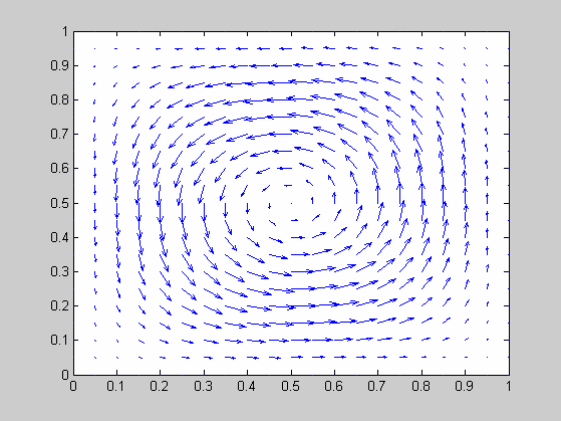

Figure 24: Exact Solution of velocity field

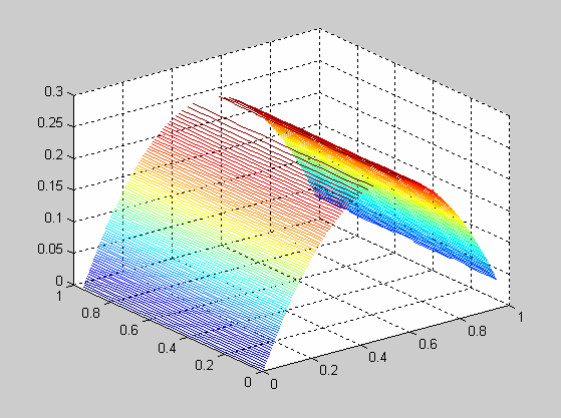

Figure 25: Exact Solution of pressure field

The first order norm error is applied to compare the velocity and pressure results between the developed MATLAB code and the exact solution. The definition of the calculated error is shown in Equation 3.5.

$$e_{v_x} = \sum \left(|\hat{v}_x| - |v_x| \right), \tag{3.5}$$

where e is the error, $\hat{v}_x$ is the exact solution, and v_x is the simulation solution

For the velocity field, error in the x-direction of the velocity was $2.3791 \cdot 10^{-16}$ and for the y-direction of the velocity it was $1.3047 \cdot 10^{-16}$. The pressure field error was $3.8580 \cdot 10^{-15}$.

Note that the pressure values for the current simulation start at -0.15, while the exact solution values start at zero. This is due to the fact that the pressure can only be found by an arbitrary constant.

The results obtained from the MATLAB simulation directly correlate to the results found by Donea and Huerta (2003) for the Q2Q1 element, and the analytical solution with superior error tolerance [Donea and Huerta (2003)].

The MATLAB code used to formulate the Stokes Flow problem can be found in Appendix B.1.

4 Steady State Navier Stokes: Cavity Flow

Preface

A benchmark standard for two-dimensional incompressible flow is the cavity flow problem. Stokes Flow and Navier-Stokes problems can be analyzed by cavity flow situations. For this particular problem a Newtonian, low-speed, viscous, incompressible fluid is analyzed using the Navier-Stokes equations. The results of this analysis are compared to published results.

4.1 Cavity Flow Problem Definition

The cavity flow problem models a plane flow of an isothermal fluid in a square lid-driven cavity. The top side of the cavity moves, in its own plane, at unit speed. The other sides of the cavity are fixed boundary conditions. The upper two corners of the cavity present an issue for the boundary conditions: the upper corners can either be constrained to the fixed boundary condition (non-leaky), or they can be assumed to follow the top side of the cavity at unit speed (leaky). The latter condition is employed here. At these points there will also be singularities in the pressure partly due to the different Dirichlet boundary conditions.

The cavity flow problem will be analyzed first by Stokes flow, as in Chapter 3 and secondly by stationary Navier-Stokes flow. The differences in these two flows are the convective term, or the inertial effects, as the viscosity changes.

4.2 Stokes Flow Solution

It is important to solve this problem primarily for a Stokes Flow, which leaves the inertial non-linear term out of the governing differential equation. The domain $\Omega = [0:1,0:1]$ is discretized using a 15 X 15 uniform mesh using the Q2Q1 master element. Results of the

Stokes Flow are shown in Figures 26, 27, and 28. Figure 26 shows the velocity field, Figure 27 shows a particle streamline plot, and Figure 28 shows the pressure field.

The properties for the fluid are:

Kinematic viscosity = $\upsilon = 1\ m^2/s$

Density = $\rho = 1\ kg/m^3$

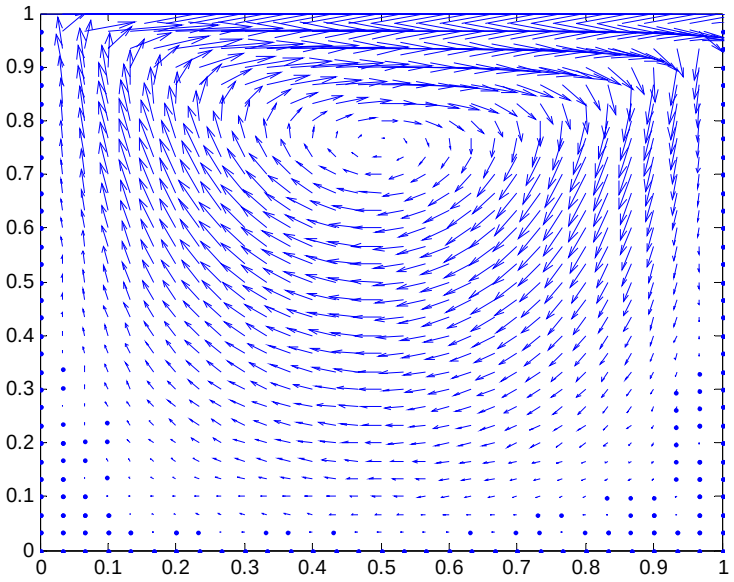

Figure 26: Stokes Flow for Cavity Flow – Velocity Field

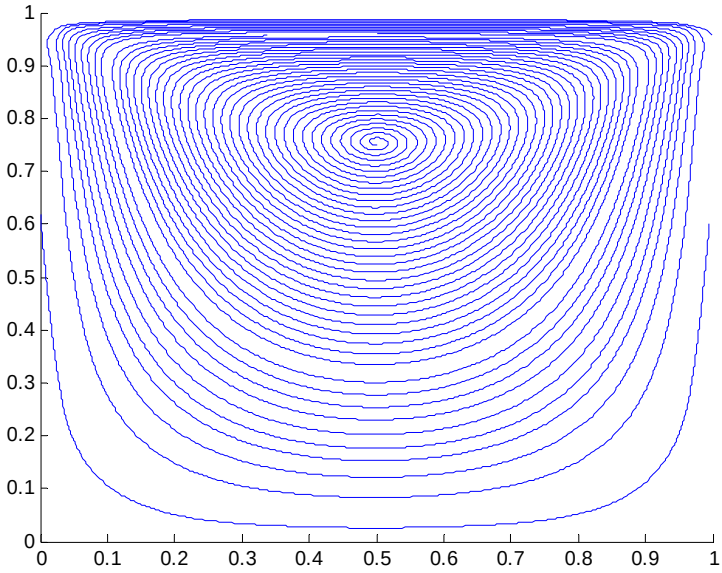

Figure 27: Stokes Flow for Cavity Flow – Particle Streamline Plot

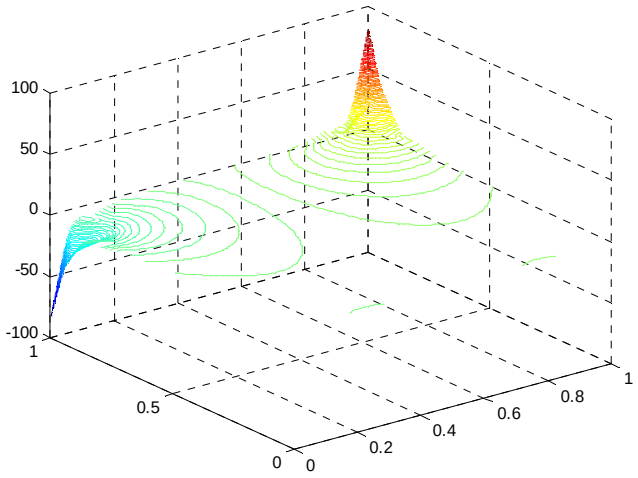

Figure 28: Stokes Flow for Cavity Flow - Pressure

Note that the particle streamline plot shows particle streamlines, which exist as if a particle was followed after it was dropped into the middle vortex.

It is easily seen that the center of the particle streamline plot, Figure 27, is at [0.5, 0.75] and the velocity field, Figure 26 and 27, has symmetry. It is also seen that the pressure field

has singularities at both upper corners of the cavity. These results are in good agreement with the results found by Donea and Huerta (2003) and Olsen and Tuann (1979).

4.3 Stationary Navier-Stokes Flow

Revisiting the Navier-Stokes equation for Stokes Flow provides Equations 3.2. However in the case of cavity flow, which will have increasing viscosities due to analysis at increasing Reynolds numbers, the inertial terms become significant and therefore they need to be included in the governing equation that is solved. The only terms neglected out of the complete Navier-Stokes equations are the dynamic, or mass, terms; leaving the following equation for analysis.

$$\begin{pmatrix} [K]+[C] & [G] \\ [G]^T & 0 \end{pmatrix} \begin{pmatrix} \underline{v} \\ \underline{p} \end{pmatrix} = \begin{pmatrix} \underline{f} \\ 0 \end{pmatrix}, \tag{4.1}$$

Equation 4.1 is the same as Equation 2.32 except the dynamic terms are not included.

For stationary Navier-Stokes solutions, the Reynolds number, R_e, completely characterizes the problem. $R_e = V_{char}L_{char}/\upsilon$, where V_{char} is the characteristic velocity, L_{char} is the characteristic length and υ is the kinematic viscosity. In the case of cavity flow, $V_{char} = 1$ m/s and $L_{char} = 1$ meter, are already set. Therefore the only way to influence a flow is to change its kinematic viscosity, or more specifically the dynamic viscosity, μ, because the density is set at 1 kg/m^3.

The following properties for the next three analyses are:

Reynolds number = {100, 400, 1000}
Dynamic viscosity = μ = {1/100, 1/400, 1/1000} N*s/m^2
Density = ρ = 1 kg/m^3
V_{char} = 1m/s
L_{char} = 1m

Dealing with increasing Reynolds numbers can cause the flow to become unstable, due to approximations made to the non-linear convective term and the high velocity gradient.

Therefore a non-uniform mesh was developed to deal with the boundary layers, high velocity gradients and the intense pressure singularities at the upper two corners. The refinement of the mesh is displayed in Figure 29, which shows the non-uniform 23 x 23 mesh that was defined by plotting circles where each node is located. The divisions for the non-uniform mesh are: [0.005 0.010 0.030 0.060 0.100 0.150 0.200 0.250 0.300 0.375 0.450 0.525 0.600 0.675 0.750 0.800 0.850 0.900 0.940 0.970 0.990 0.995 1.000].

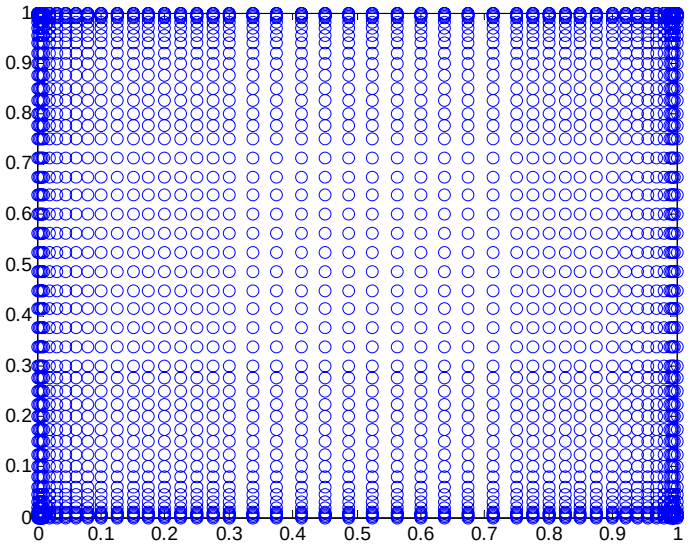

Figure 29: Non-uniform discretization of domain where circles represent nodes

The handling of the non-linear convective term is a current area of research. Equation 2.12, without the dynamic term, is:

$$(\underline{v} \cdot \nabla)\underline{v} - \mathrm{Re}^{-1} \nabla^2 \underline{v} + \nabla p = \underline{b}, \tag{4.2}$$

where the inverse of the Reynolds number is replacing the kinematic viscosity, discussed above. The Reynolds number, represented in this equation, is a measure of the relative strength of the non-linear term to the viscous term. If the R_e is high, it renders the convective term dominant because the viscous term is more insignificant. Therefore flows that have higher Reynolds numbers need to include the convective term and deal with its non-linearity.

The non-linearity of the convective term and the difficulties associated with it, when solving finite element problems, is brought about when it is expanded. Equations 4.3 shows the convective term in the x and y directions.

$$x-direction: \quad \rho\left(v_x \frac{\partial v_x}{\partial x} + v_y \frac{\partial v_x}{\partial y}\right),$$
$$y-direction: \quad \rho\left(v_x \frac{\partial v_y}{\partial x} + v_y \frac{\partial v_y}{\partial y}\right), \tag{4.3}$$

It has been previously noted that an approximation takes place for the velocity that follows the forms of Equations 2.29. For the convective terms it is unclear whether to approximate the velocity term or the derivative of the velocity term; the reason that current research is ongoing. Equations 4.4 and 4.5 show the weak formulation of just the convective term. Case (1) is where the velocity is approximated and then Case (2) is where the derivative of the velocity is approximated:

Case (1):

$$x-direction: \quad \sum_{j=1}^{N_{nodes}} \left[\int_{\Omega_e} \Psi_i \rho\left(\Psi_j \frac{\partial v_x}{\partial x}\right)\right] \tilde{v}_x + \sum_{j=1}^{N_{nodes}} \left[\int_{\Omega_e} \Psi_i \rho\left(\Psi_j \frac{\partial v_x}{\partial y}\right)\right] \tilde{v}_y,$$
$$y-direction: \quad \sum_{j=1}^{N_{nodes}} \left[\int_{\Omega_e} \Psi_i \rho\left(\Psi_j \frac{\partial v_y}{\partial x}\right)\right] \tilde{v}_x + \sum_{j=1}^{N_{nodes}} \left[\int_{\Omega_e} \Psi_i \rho\left(\Psi_j \frac{\partial v_y}{\partial y}\right)\right] \tilde{v}_y, \tag{4.4}$$

Case (2):

$$x-direction: \quad \sum_{j=1}^{N_{nodes}} \left[\int_{\Omega_e} \Psi_i \rho\left(v_x \frac{\partial \Psi_j}{\partial x} + v_y \frac{\partial \Psi_j}{\partial x}\right)\right] \tilde{v}_x,$$
$$y-direction: \quad \sum_{j=1}^{N_{nodes}} \left[\int_{\Omega_e} \Psi_i \rho\left(v_x \frac{\partial \Psi_j}{\partial x} + v_y \frac{\partial \Psi_j}{\partial x}\right)\right] \tilde{v}_y, \tag{4.5}$$

Many experts in the field approximate the derivative of the velocity, Case (2), and this approach was taken for this research because it eliminates extra computations associated with the derivative.

In the equations of Case (2) it is unclear what the values for the v_x and v_y terms, in the integral statement. Since these values are not known, an iterative loop must be set up to converge on a specific answer within a specified tolerance.

These unknown values and the convergence loop construction is another area of current research. One of the methods of solving this problem is to utilize a technique that can be seen in both finite difference and finite element analyses. When solving for Equations 4.4 and 4.5, in matrix format, use nodal velocities from the previous iterative loop as the velocities inside the integral statement.

The convergence tolerance of the iterative loops was calculated by the following formula:

$$tolerance = \frac{\sum_{i=1}^{N_{nodes}} \left(\frac{\left| v_{old_{i,j}} \right| - \left| v_{new_{i,j}} \right|}{\left| v_{new_{i,j}} \right|} \right)}{N_{nodes}}, \qquad j = \{1,2\} \qquad (4.6)$$

where N_{nodes} is the number of nodes, $v_{old\,i}$ is an array of velocities in the x-direction and the y-direction from the previous iterative loop, and $v_{new\,i}$ is an array of velocities in the x-direction and the y-direction from the current iterative loop. This is considered the Cauchy convergence criteria. It is also possible to use the second residual norm type of convergence criteria.

Using this approach for the convective iterative loops, the results for the cavity flow problem with $R_e = 100$ are shown below. Figure 30 shows the velocity field, Figure 31 shows the particle streamline plot and center vortex location, Figure 32 shows the pressure distribution and singularities, and Figure 33 shows the velocity contour plot.

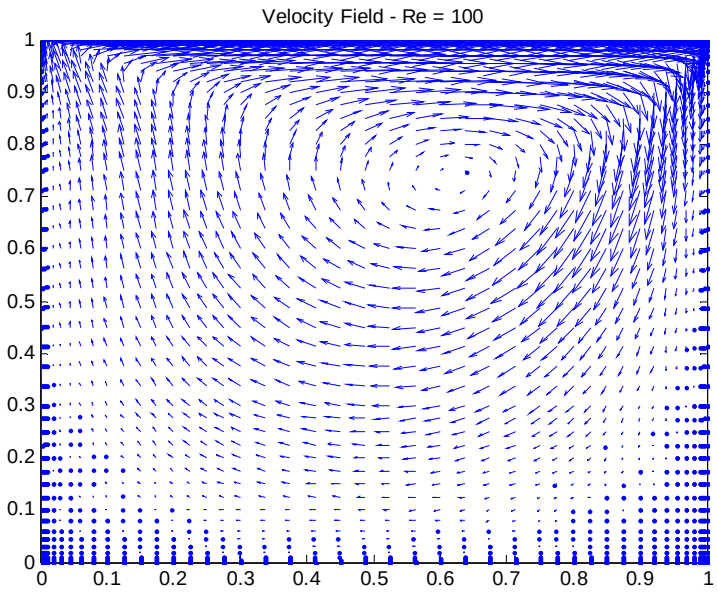

Figure 30: Navier-Stokes Velocity Field at Re = 100 for Cavity Flow

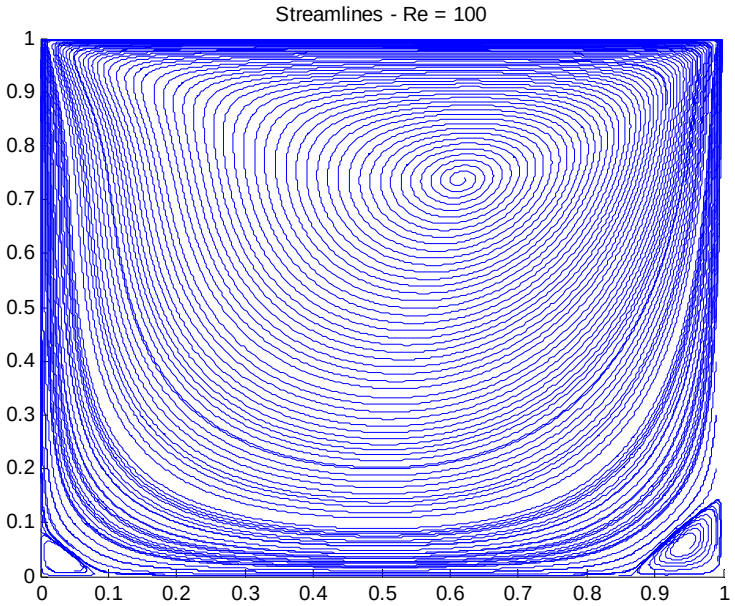

Figure 31: Navier-Stokes Particle Streamline Plot at Re = 100 for Cavity Flow
Center vortex location: {0.62, 0.74} and note vorticies in both lower corners

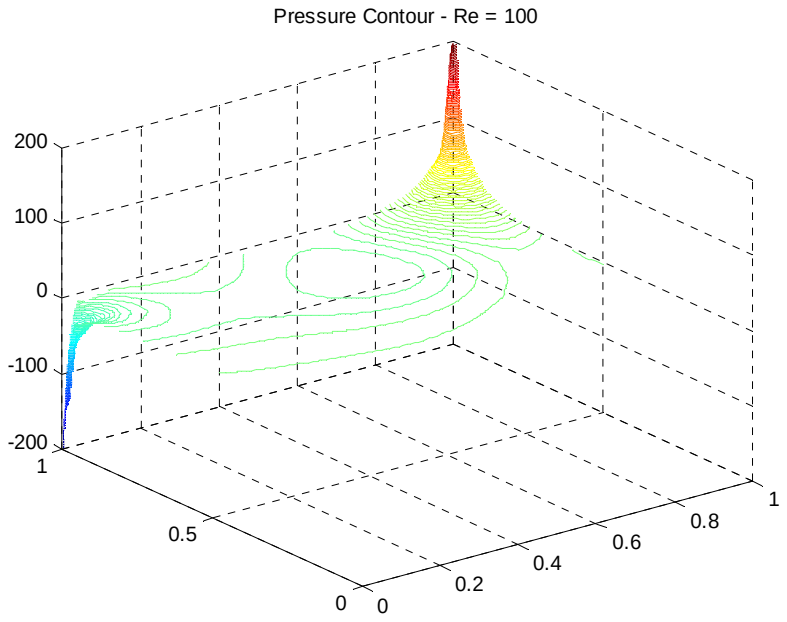

Figure 32: Pressure distribution and singularities for Re = 100 Navier-Stokes Cavity Flow

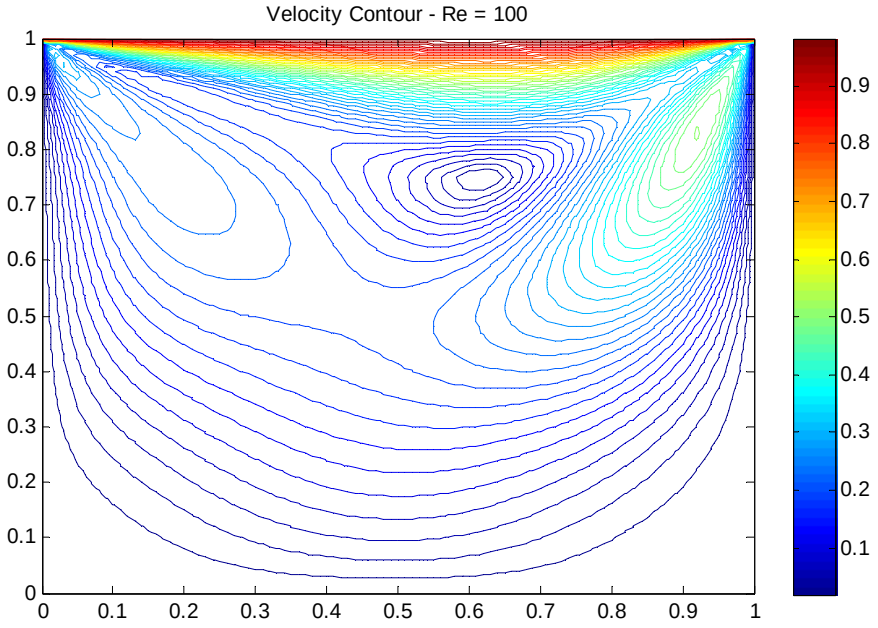

Figure 33: Velocity contour plot for Re = 100 for Navier-Stokes Cavity Flow

For a R_e = 100, 23 X 23 non-uniform mesh, the cavity flow problem converged under 2% in 5 iterations. These results, for R_e = 100, are in good agreement with the results found by Donea and Huerta (2003) and Olsen and Tuann (1979).

The results for the cavity flow problem with $R_e = 400$ are shown below. Figure 34 shows the velocity field, Figure 35 shows the particle streamline plot and center vortex location, Figure 36 shows the pressure distribution and singularities, and Figure 37 shows the velocity contour plot.

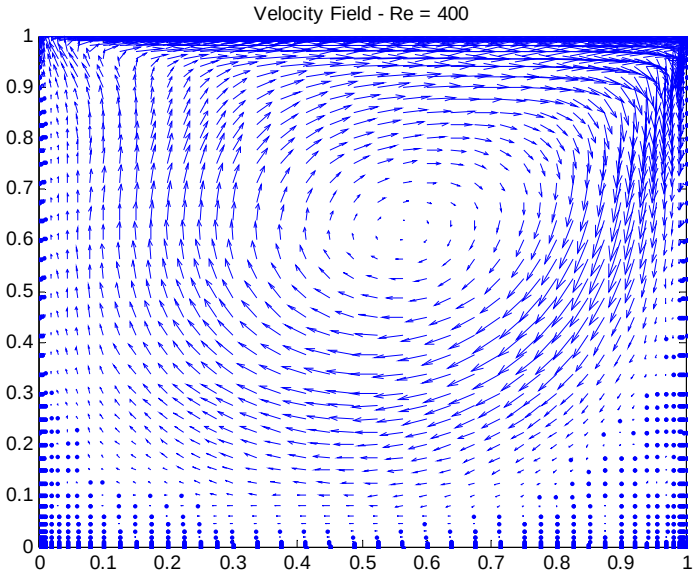

Figure 34: Navier-Stokes Velocity Field at Re = 400 for Cavity Flow

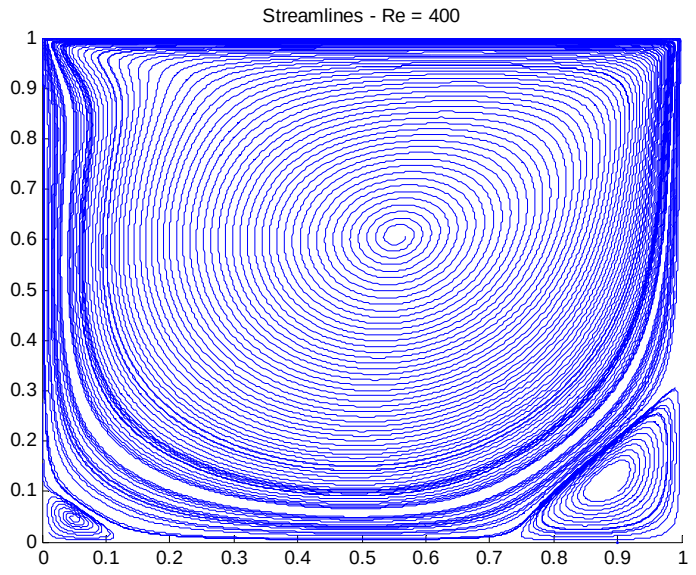

Figure 35: Navier-Stokes Particle Streamline Plot at Re = 400 for Cavity Flow
Center vortex location: {0.57, 0.61}and note vorticies in both lower corners

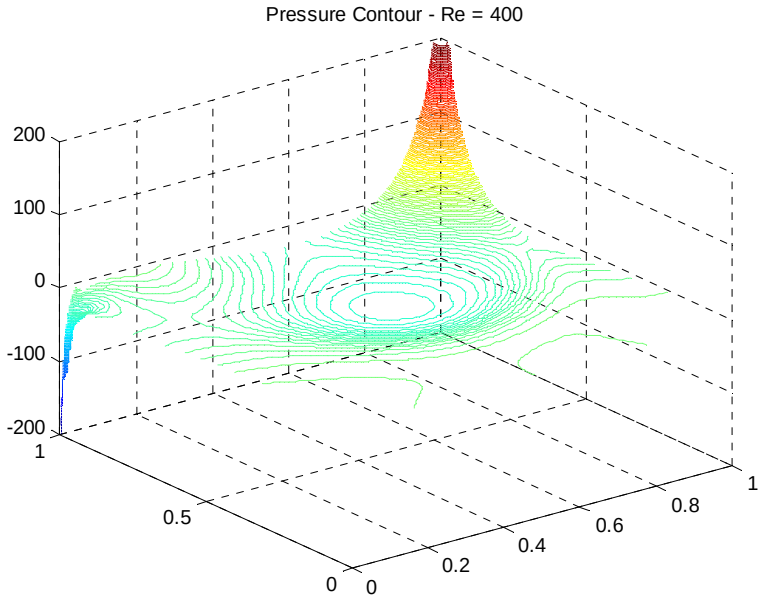

Figure 36: Pressure distribution and singularities for Re = 400 Navier-Stokes Cavity Flow

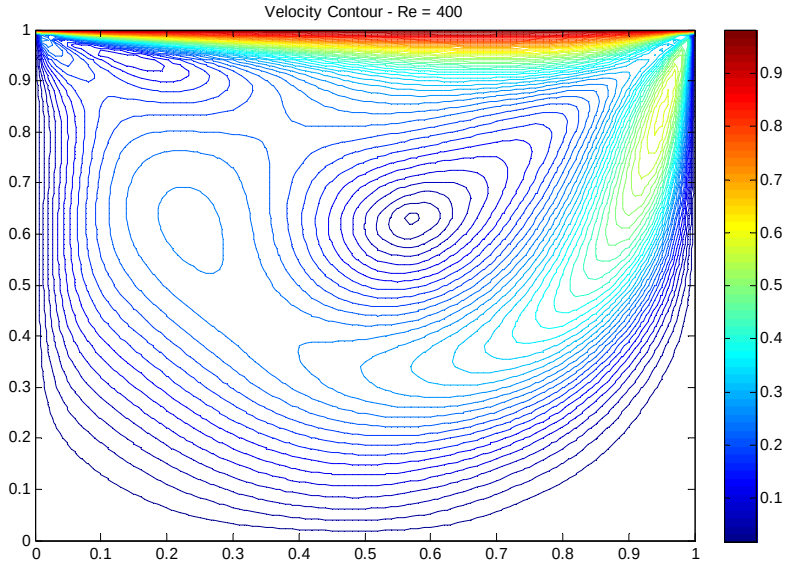

Figure 37: Velocity contour plot for Re = 400 for Navier-Stokes Cavity Flow

For a R_e = 400, 23 X 23 non-uniform mesh, the cavity flow problem converged under 2% in 6 iterations. These results, for R_e = 400, are in good agreement with the results found by Donea and Huerta (2003) and Olsen and Tuann (1979).

The results for the cavity flow problem with $R_e = 1000$ are shown below. Figure 38 shows the velocity field, Figure 39 shows the particle streamline plot and center vortex location, Figure 40 shows the pressure distribution and singularities, and Figure 41 shows the velocity contour plot.

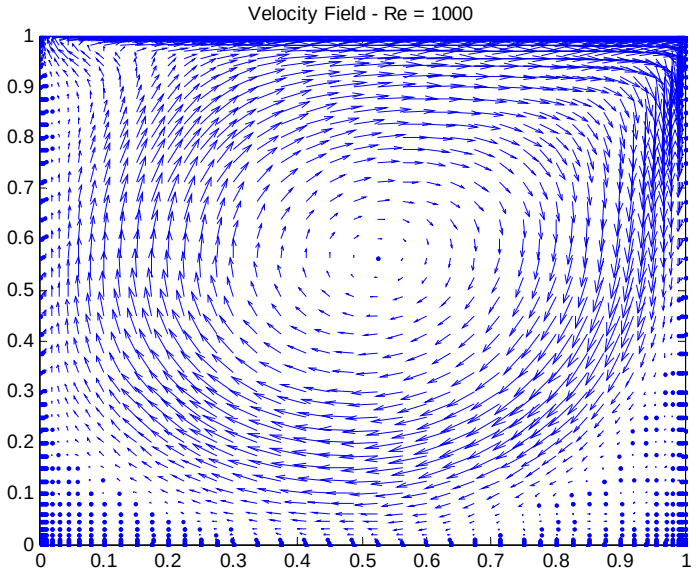

Figure 38: Navier-Stokes Velocity Field at Re = 1000 for Cavity Flow

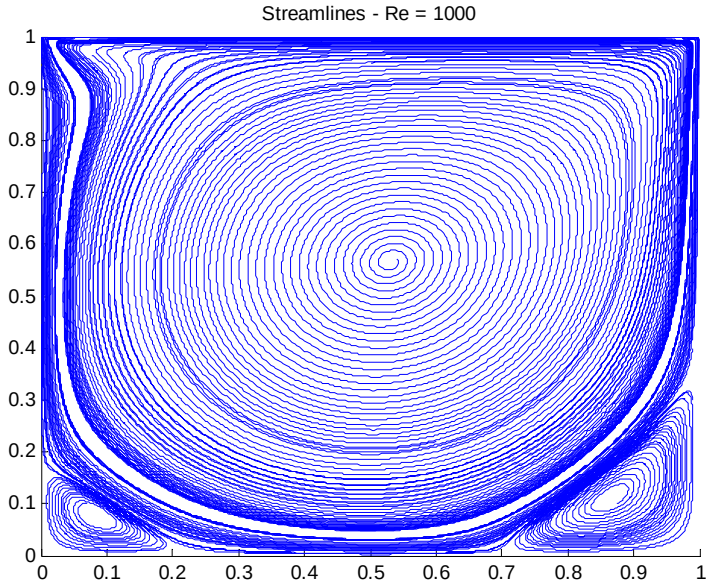

Figure 39: Navier-Stokes Particle Streamline Plot at Re = 1000 for Cavity Flow
Center vortex location: {0.54, 0.57} and note vorticies in both lower corners

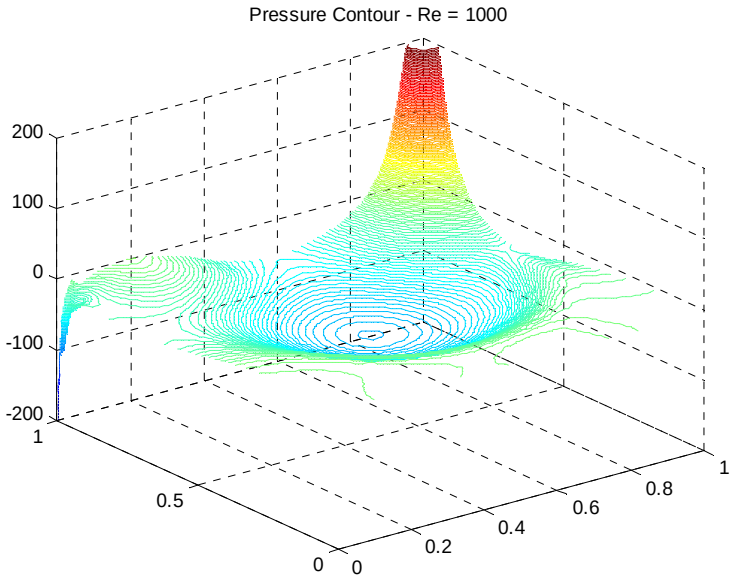

Figure 40: Pressure distribution and singularities for Re = 1000 Cavity Flow

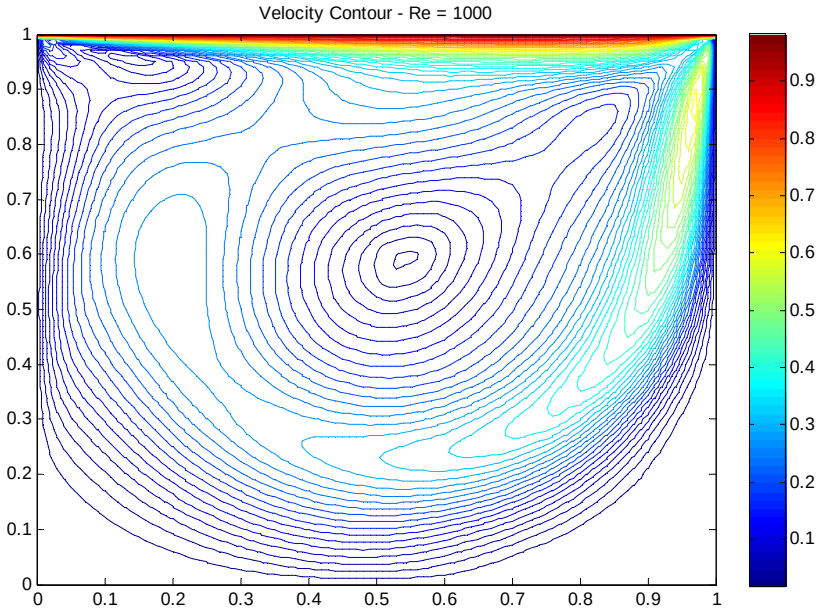

Figure 41: Velocity contour plot for Re = 1000 for Navier-Stokes Cavity Flow

For a R_e = 1000, 23 X 23 non-uniform mesh, the cavity flow problem converged under 2% in 7 iterations. These results, for R_e = 1000, are in good agreement with the results found by Donea and Huerta (2003) and Olsen and Tuann (1979).

The summary of the results and comparisons to published data can be found in the following table (Table 2):

Cavity Flow Center Vortex Location	x	y
Stokes Flow		
Current Simulation	0.50	0.75
Donea and Huerta (2003)	0.50	0.75
Olsen and Tuann (1979)	0.50	0.76
$R_e = 100$		
Current Simulation	0.62	0.74
Donea and Huerta (2003)	0.62	0.74
Olsen and Tuann (1979)	0.62	0.74
$R_e = 400$		
Current Simulation	0.57	0.61
Donea and Huerta (2003)	0.568	0.606
Olsen and Tuann (1979)	0.55	0.60
$R_e = 1000$		
Current Simulation	0.54	0.57
Donea and Huerta (2003)	0.540	0.573
Olsen and Tuann (1979)	0.53	0.56

The data found from the current simulation correlates very well to the published data [Donea and Huerta (2003) and Olsen and Tuann (1979)]. MATLAB code can be found in Appendix B.2.

Table 2: Simulation vs. Published Results for Various Cavity Flow Reynolds Numbers

5 Transient Navier Stokes Analysis: Plane Jet

Preface

A transient condition is defined when the situation being analyzed is changing over time. A transient analysis takes place when a water jet is introduced to stationary water. For this particular problem a Newtonian, low-speed, viscous, incompressible fluid will be analyzed using the Navier-Stokes equations. The MATLAB simulation results will be compared to published results and ANSYS 9.0 results.

5.1 Transient Plane Jet Problem Definition

The transient plane jet problem models a plane flow where the domain is the right-half space, or $\{x > 0\}$ and $\{-\infty < y < \infty\}$. The computational domain is condensed to only incorporate a small section of the positive right-half space: $\{0 < x < 1\}$ m and $\{0 < y < 1\}$ m. The jet is parabolic shaped having a velocity of 1 m/s, situated at $\{0, 0.5\}$ and is 1/16 m wide, corresponding to a $R_e = 125$. The domain is discretized by a 16 X 16 uniform mesh of Q2Q1 elements.

The properties for the fluid are:

Kinematic viscosity = $\upsilon = 5 \times 10^{-4}$ m^2/s

Density = $\rho = 1$ kg/m^3

The boundary conditions for this problem are essential and normal boundary conditions. On the left wall ($x = 0$), the velocity in the x and y-directions are set equal to zero except where the jet is located. The boundary conditions for the top ($y = 1$) and bottom ($y = 0$) sides of the domain set the velocity in the x-direction and the traction forces in the y-direction to be zero. The reason for the traction force boundary condition is to satisfy the necessary amount of boundary conditions. This is considered an open/artificial boundary condition

because it is imposed to represent infinite boundary conditions. The boundary conditions on the right side (x = 1) set the velocity in the y-direction and the traction force in the x-direction to be zero. Figure 42 shows a schematic of the plane jet flow problem with labeled boundary conditions.

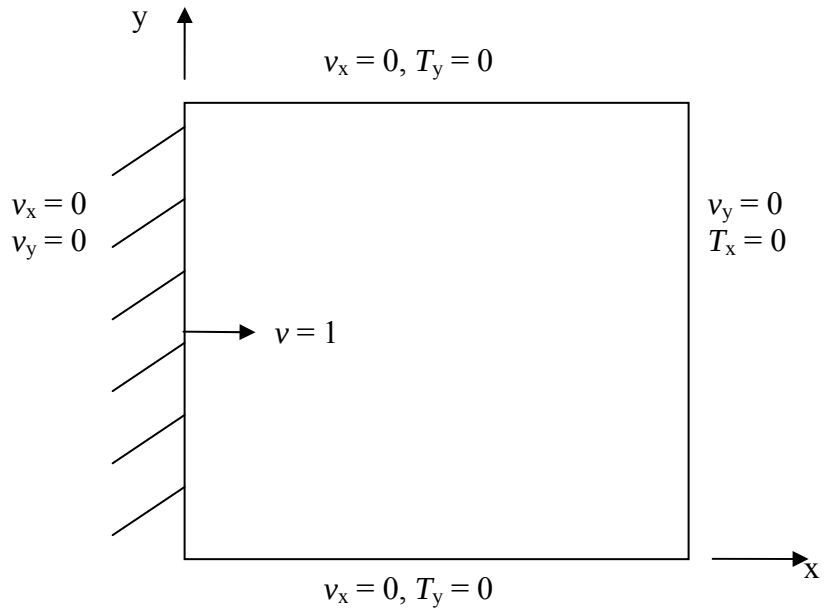

Figure 42: Plane jet flow problem boundary conditions

5.2 Solving Transient Navier-Stokes using FEA

The time marching scheme implemented for this problem is the Chorin-Temam projection method. The fluid is considered at rest for t = 0. The Chorin-Temam projection method can be viewed as a physical splitting of the original incompressible Navier-Stokes equations into two relatively easy sub-steps. The first sub-step is associated with time discretization and finds an intermediate velocity. The second sub-step is associated with spatial discretization and finds the end-of-step pressure and velocity [Donea and Huerta (2003)].

Quarteroni, Saleri, and Veneziani (2000) introduced a full algebraic splitting technique for the Chorin-Temam projection method that efficiently solves transient solutions of the incompressible Navier-Stokes equations. The algebraic splitting technique of the Chorin-

Temam projection method is primarily based on an incomplete (or approximate) block LU factorization of the original transient Navier-Stokes equations, shown in Equation 5.1:

$$\begin{pmatrix} [B] & [G] \\ [G]^T & 0 \end{pmatrix} \begin{pmatrix} \underline{v}^{n+1} \\ \underline{p}^{n+1} \end{pmatrix} = \begin{pmatrix} \underline{f}^* \\ \underline{h} \end{pmatrix}, \tag{5.1}$$

where $\underline{f}^*$ incorporates the dirichlet velocities and known terms resulting from known velocities of the previous time step.

For simplicity [*B*] is a condensed version of the full equations solved with an implicit Euler scheme for iterations, shown in Equation 5.2.

$$[B] = \frac{1}{\Delta t}[M] + ([K] + [C(v^{n+1})]), \tag{5.2}$$

Quarteroni et al. (2000) showed that an exact LU factorization of Equation 5.1 is:

$$\begin{pmatrix} [B] & 0 \\ [G]^T & -[G]^T[B]^{-1}[G] \end{pmatrix} \begin{pmatrix} I & [B]^{-1}[G] \\ 0 & I \end{pmatrix} \begin{pmatrix} \underline{v}^{n+1} \\ \underline{p}^{n+1} \end{pmatrix} = \begin{pmatrix} \underline{f}^* \\ \underline{h} \end{pmatrix}, \tag{5.3}$$

The inverse of [B], from Equation 5.2, is quite computationally intensive. Therefore first, second and third order approximations to the inverse of [*B*] have been constructed:

$$[B]_1^{-1} \approx [H]_1 = \Delta t[M]^{-1}, \tag{5.4}$$

$$[B]_2^{-1} \approx [H]_2 = \Delta t\left(I - \Delta t[M]^{-1}([K] + [C])\right)[M]^{-1}, \tag{5.5}$$

$$[B]_3^{-1} \approx [H]_3 = \Delta t\left(I - \Delta t[M]^{-1}([K] + [C]) + \Delta t^2\left([M]^{-1}([K] + [C])\right)^2\right)[M]^{-1}, \tag{5.6}$$

For these expressions the mass matrix, [*M*], is diagonalized using the 'row-sum' (or 'lumped-mass') technique. It has been documented that for a 9-noded element, the 'lumped mass' term stabilizes a majority of problems, even in convection dominated situations [Donea et al. (1982)].

Equation 5.3 is segmented again to obtain the two steps of the Chorin-Temam projection method:

$$\begin{pmatrix} [B] & 0 \\ [G]^T & -[G]^T[B]^{-1}[G] \end{pmatrix} \begin{pmatrix} \underline{v}_{\text{int}}^{n+1} \\ \underline{p}_{\text{int}}^{n+1} \end{pmatrix} = \begin{pmatrix} \underline{f}^* \\ \underline{h} \end{pmatrix}, \tag{5.7}$$

$$\begin{pmatrix} I & [B]^{-1}[G] \\ 0 & I \end{pmatrix} \begin{pmatrix} \underline{v}^{n+1} \\ \underline{p}^{n+1} \end{pmatrix} = \begin{pmatrix} \underline{v}_{\text{int}}^{n+1} \\ \underline{p}_{\text{int}}^{n+1} \end{pmatrix} \tag{5.8}$$

The third order approximation (5.6) was chosen to represent all instances of the inverse of [*B*]. Projection fractional-step methods, such as Chorin-Temam, use this same approach to solve for the final result [Donea and Huerta (2003)].

Using Equations 5.7 and 5.8, $\underline{v}^{n+1}$ and $\underline{p}^{n+1}$ can be calculated by means of the following steps (similar to the Stokes Flow solution technique):

$$L-step \begin{cases} [B]\underline{v}_{\text{int}}^{n+1} = \underline{f}^*, \\ [G]^T \underline{v}_{\text{int}}^{n+1} - [G]^T [H_3][G]\underline{p}_{\text{int}}^{n+1} = \underline{h}, \end{cases}$$

$$U-step \begin{cases} \underline{v}^{n+1} + [H_3][G]\underline{p}^{n+1} = \underline{v}_{\text{int}}^{n+1}, \\ \underline{p}^{n+1} = \underline{p}_{\text{int}}^{n+1}, \end{cases}$$

Or equivalently:

$$\begin{cases} [B]\underline{v}_{\text{int}}^{n+1} = \underline{f}^*, & \text{(Intermediate Velocity Computation)} \\ [G]^T [H_3][G]\underline{p}^{n+1} = [G]^T \underline{v}_{\text{int}}^{n+1} - \underline{h}, & \text{(Pressure Computation)} \\ \underline{v}^{n+1} = \underline{v}_{\text{int}}^{n+1} - [H_3][G]\underline{p}^{n+1}, & \text{(End-of-Step Velocity Computation)} \end{cases}$$

The first step is the implicit iterative step, to find the intermediate velocity. On completion of the intermediate velocity, the pressure and end-of-step velocity are calculated using the second and third steps, respectively.

5.3 Transient Plane Jet Solution and Comparison

Using MATLAB code, solutions for the transient jet problem were obtained and compared to three solutions at different times using a time step $\Delta t = 0.1$ seconds and the solution technique of algebraic splitting of the Chorin-Temam projection method.

For the MATLAB code the transient solutions are shown in Figures 43-46, which show the transient time values of {0.1, 1.2, 2.5 and 4.0} seconds. Figure 43-46 show the velocity particle streamlines and pressure contour plots respectively at times {0.1, 1.2, 2.5 and 4.0} seconds.

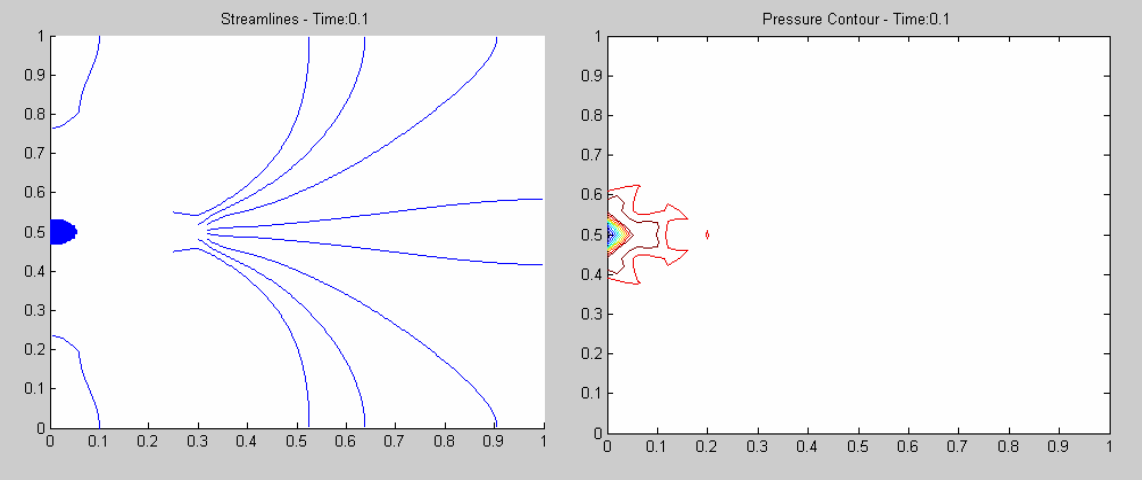

Figure 43: Particle Streamline and Pressure Contour Plots for t = 0.1 sec

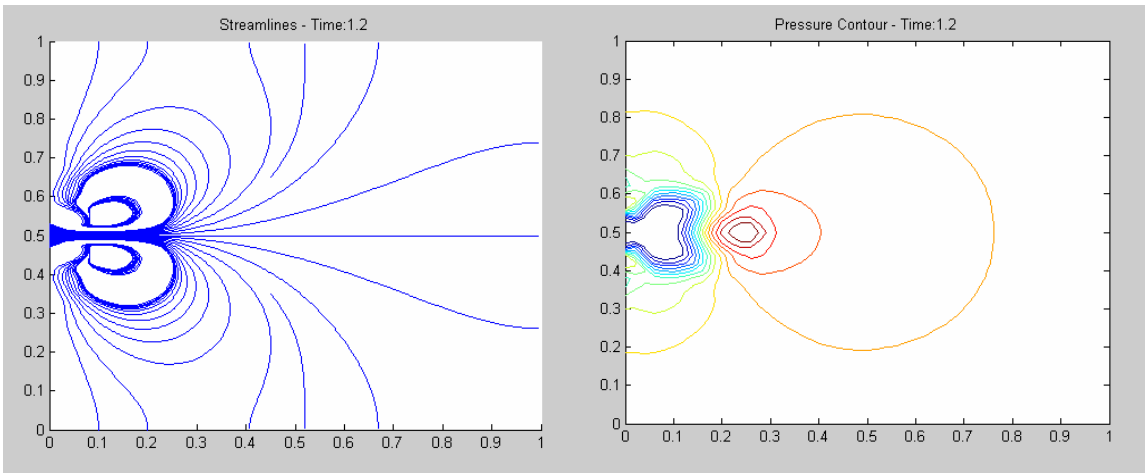

Figure 44: Particle Streamline and Pressure Contour Plots for t = 1.2 sec

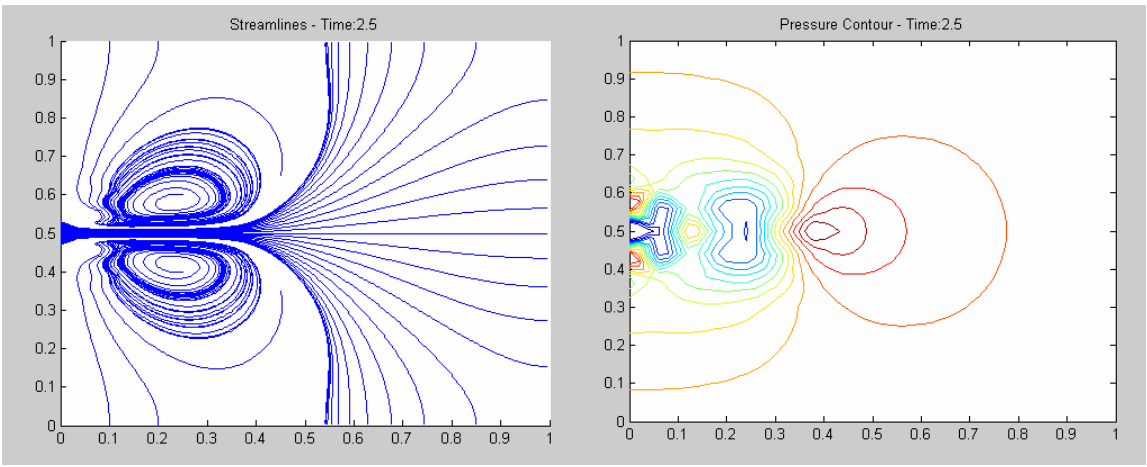

Figure 45: Particle Streamline and Pressure Contour Plots for t = 2.5 sec

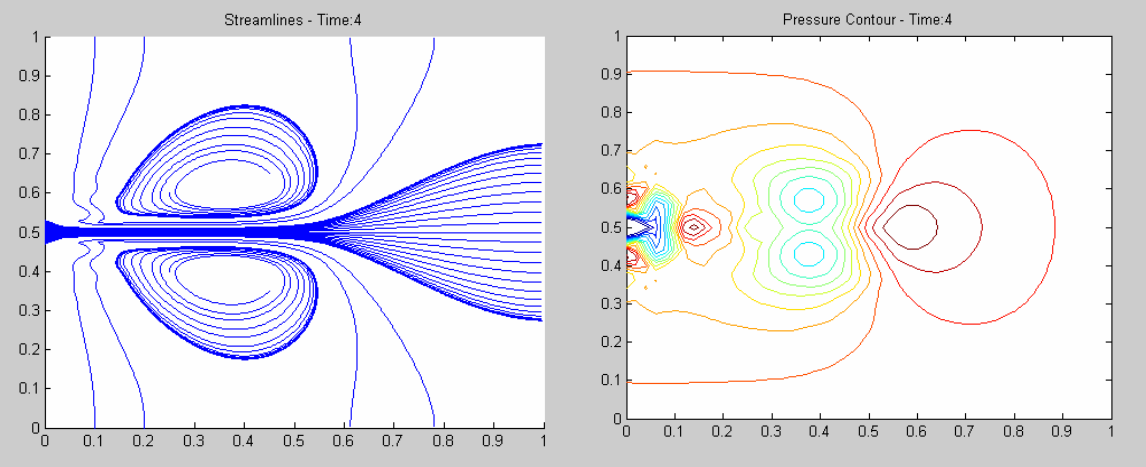

Figure 46: Particle Streamline and Pressure Contour Plots for t = 4.0 sec

The MATLAB simulation results are in good agreement with published data by Donea and Huerta (2003), Laval and Quartapelle (1990), and Bristeau et al. (1987). Donea and Huerta used the Chorin-Temam projection method, while Laval and Quartapelle used a three-phase fractional-step Taylor-Galerkin method.

The algebraic splitting method, which is based on the Chorin-Temam projection method, accurately portrays the velocity and pressure for a plane jet problem however it is still only first-order in time. Modified schemes have been developed for higher-order methods [Donea and Huerta (2003)].

It should be pointed out that the algebraic splitting technique based on the Chorin-Temam projection method, as used above, must use elements satisfying the LBB condition, discussed previously. Guermond and Quartapelle (1998) concluded that in the case of an incremental projection scheme, such as the Chorin-Temam projection method, the element velocity-pressure pairs must satisfy the LBB compatibility condition to obtain non-oscillatory numerical results [Donea and Huerta (2003)].

The transient jet problem is also solved using ANSYS 9.0 in order to validate the MATLAB results. ANSYS 9.0, a finite element software package, obtains answers that are commercially available and used in industry and academia.

The solution found using ANSYS 9.0 used the following commands:

Preprocessor:

Element type - Fluid141 (4-node element, 9-node does not exist)
Modeling - Create - Areas - By Dimensions
Meshing - Mesh Tool - Lines (All Four) - 32 divisions
- Mesh - Areas - Mapped - MESH

Solution:

Boundary Conditions - Vx = 0 on top, bottom and left lines (except jet location)
- Vy = 0 on left and right lines
- Pressure = 0 on top and bottom lines (for reference)

FLOTRAN Setup:

- Solution Opts: Transient, Laminar, Incompressible
- Execution Ctrl: Advection, ISTEP = 0.1
- Fluid Properties: Density = 1, Dynamic Viscosity = 5e-4

RUN FLOTRAN

Post-Processing:

Read Results – Last Step

The results from the ANSYS 9.0 analysis are shown in Figures 47-49. Figures 47-49 show the velocity vector plots and the pressure contour plots for transient time values of {1.2, 2.5, 4.0} seconds, respectively.

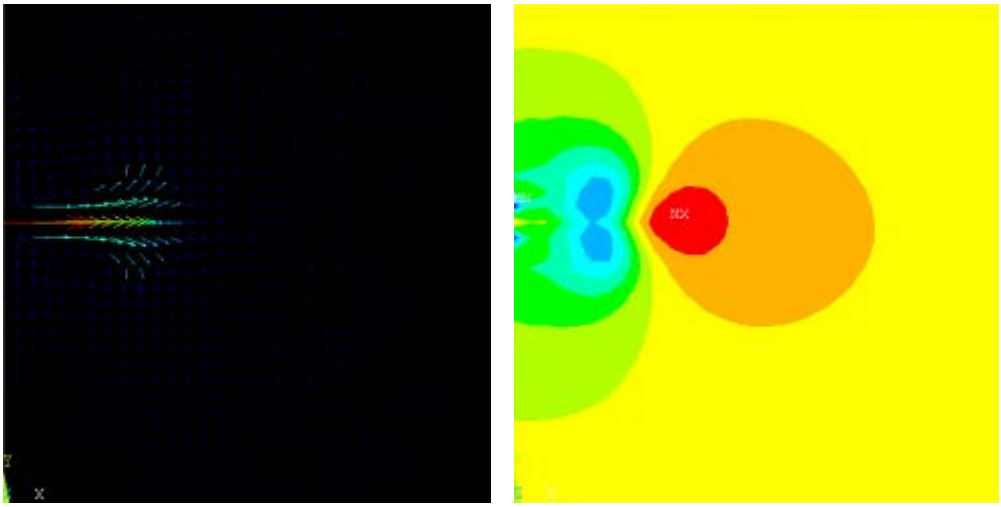

Figure 47: Velocity vector plot and the pressure contour plot respectively for t = 1.2 sec

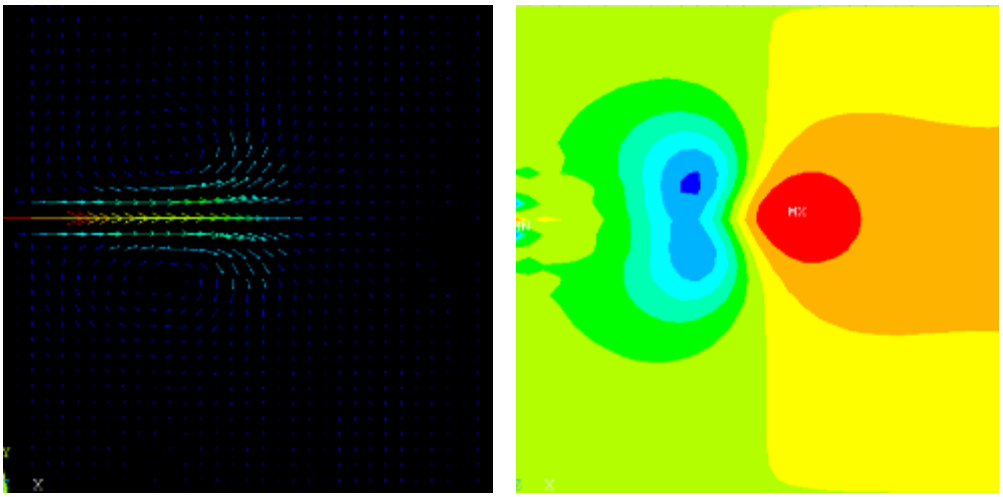

Figure 48: Velocity vector plot and the pressure contour plot respectively for t = 2.5 sec

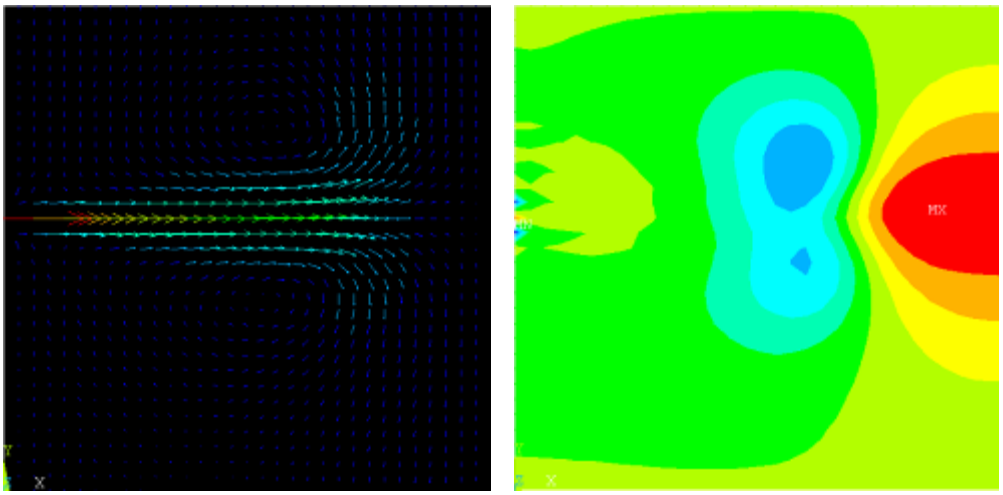

Figure 49: Velocity vector plot and the pressure contour plot respectively for t = 4.0 sec

The simulation results agree well with the ANSYS 9.0 results.

The MATLAB code for the plane jet flow problem can be found in Appendix B.3.

6 Stability for the Navier-Stokes Equations

Preface

The Galerkin weighted-residual method of finite element analysis is easily implemented and allows for less computational effort because weighting functions are chosen to be the same as the interpolation functions. However with highly convective flows, or flows with high Reynolds numbers, this introduces a truncation error. The handling of the non-linear convective term for the Galerkin weighted-residual method of finite element analysis is still an area of current research, however methods have been developed to deal with the truncation error introduced. This section will introduce the areas of instability associated with the Galerkin finite element analysis method and show current stability methods that have been developed to diminish truncation error introduced by the method and in some cases create an exact solution for highly convective flows.

6.1 The Stability Term

The Navier-Stokes equations, by definition are free of dissipation, meaning no energy is lost over time. Solving the Navier-Stokes equations using finite element analysis, specifically the Galerkin weighted-residual method, introduces negative diffusion because the weighting function is assigned to be the same as the interpolation function for the convective term [Donea and Huerta (2003)].

In the 1970's an 'upwind' scheme was developed by the Dundee and Swansea research groups that placed the foundation for the solutions currently being solved. The 'upwind' technique modifies the weighting function on the convective term to weight the elements 'upstream' of a node more heavily than 'downstream', of a flow. This is done because convective transport takes place along streamlines, not transversely. In a series of papers by Hughes and Brooks (1979) (1982), it was found that an optimal solution could be calculated for this modification so that the nodal solutions matched exact modeling equations. The

modification of the convective weighting function took the form of an artificial diffusion term. Initially the optimal artificial diffusion term was added directly to diffusivity constant, or the viscosity term for fluids (Equation 6.2), but it was mathematically proven, shown below, that essentially the same term can be added to the convective weighting function to produce the same result [Kelly et al. 1980]. This idea is termed 'balancing diffusion' due to the fact that the added numerical diffusion counterbalances the negative diffusion that comes from the Galerkin finite element formulation. It was also documented by Brooks and Hughes (1982) that when analyzing multi-dimensional cases, this modification had to be applied to the direction of flow, by use of diffusivity tensors. At this point in the development of stability for the Galerkin finite element formulation of advection/diffusion equations, it was known that changing the weighting function of the convective term produced optimal results and for multi-dimensional cases the addition of artificial diffusion had to occur in the direction of flow. The term 'streamline-upwind' was applied to the 'upwind' technique that took place over the flow direction, or streamlines.

To follow the progress of the 'streamline-upwind' technique, a general advection/diffusion equation is represented in Equation 6.1:

$$a \cdot \nabla v - \upsilon \nabla^2 v = 0, \tag{6.1}$$

where a represents the advection constant, or convection non-linear term, v represents the unknown values, or velocity in the case of fluid motion, υ is the diffusivity constant, or viscosity for the Navier-Stokes equation. Note that source terms have been set equal to zero for simplicity.

Adding in artificial diffusion, $\bar{\upsilon}$, results in the following equation:

$$\underline{a} \cdot \nabla v - \left(\upsilon + \bar{\upsilon}\right) \cdot \nabla^2 \underline{v} = 0, \tag{6.2}$$

Constructing the weak formulation of Equation 6.2 reveals:

$$\int_{\Omega} \Psi\left(\underline{a}\cdot\nabla\underline{v}\right)d\Omega + \int_{\Omega} \Psi\left(\nabla\cdot\left(\upsilon\cdot\nabla\underline{v}\right)\right)d\Omega + \int_{\Omega} \Psi\left(\nabla\cdot\left(\overline{\upsilon}\cdot\nabla\underline{v}\right)\right)d\Omega = 0, \tag{6.3}$$

Integrating by parts, the second and third term, the weak form becomes:

$$\int_{\Omega} \Psi\left(\underline{a}\cdot\nabla\underline{v}\right)d\Omega + \int_{\Omega} \nabla\Psi\cdot\upsilon\cdot\nabla\underline{v}\,d\Omega + \int_{\Omega} \nabla\Psi\cdot\overline{\upsilon}\cdot\nabla\underline{v}\,d\Omega = 0, \tag{6.4}$$

An identity is now introduced that has been mathematically proven [Donea and Huerta (2003)]:

$$\int_{\Omega} \nabla\Psi\cdot\overline{\upsilon}\cdot\nabla\underline{v}d\Omega = \int_{\Omega} \frac{\overline{\upsilon}}{\left\|\underline{a}\right\|^2}\left(\underline{a}\cdot\nabla\Psi\right)\left(\underline{a}\cdot\nabla\underline{v}\right)d\Omega, \tag{6.5}$$

Using the proven identity, shown above in Equation 6.5, the third term can now be combined with the first term of Equation 6.4 to produce the following result:

$$\int_{\Omega} \left\{\left[\Psi + \frac{\overline{\upsilon}}{\left\|\underline{a}\right\|^2}\left(\underline{a}\cdot\nabla\Psi\right)\right]\left(\underline{a}\cdot\nabla\underline{v}\right) + \upsilon\nabla\Psi\cdot\nabla\underline{v}\right\}d\Omega = 0, \tag{6.6}$$

In this form, the modification of the weighting function applied to the convective term is $\frac{\overline{\upsilon}}{\left\|\underline{a}\right\|^2}\left(\underline{a}\cdot\nabla\Psi\right)$, which was discussed previously.

Uncoupling Equation 6.6 it is easy to discern the Galerkin finite element formulation and the added diffusion term.

$$\underbrace{\int_{\Omega} \left\{\Psi\left(\underline{a}\cdot\nabla\underline{v}\right) + \upsilon\nabla\Psi\cdot\nabla\underline{v}\right\}d\Omega}_{\textit{Galerkin Formulation}} + \underbrace{\int_{\Omega} \frac{\overline{\upsilon}}{\left\|\underline{a}\right\|^2}\left(\underline{a}\cdot\nabla\Psi\right)\left(\underline{a}\cdot\nabla\underline{v}\right)d\Omega}_{\textit{Added Diffusion Term}} = 0, \tag{6.7}$$

It was uncovered that only applying the modified weight function to the convective term caused excessively diffuse problems when source and transient terms were included in the analysis. Brooks and Hughes (1982) found that it was necessary to apply the modified weighting function to all terms in the equation. This formulation is commonly referred to as the Petrov-Galerkin form of the equation because it preserves the Galerkin weighted-residual formulation, by adding an extra term also involving the residual. Equation 6.8 represents the general stability term added to the Galerkin weighted-residual finite element formulation of the Navier-Stokes equations for incompressible flow:

$$\sum_{e} \int_{\Omega_e} \mathrm{P}(\Psi)\tau\, R(\underline{\tilde{v}})\, d\Omega_e, \tag{6.8}$$

where $\mathrm{P}(\Psi)$ is a certain operator applied to the test function, τ is the stabilization parameter, and $R(\underline{\tilde{v}})$ is the residual. Equation 6.9 takes Equation 6.8 and includes the terms associated with the 'streamline-upwind/Petrov-Galerkin' (SUPG) formulation of the added diffusion term. At this point it is important to note that by including the whole residual, the term is not referred to as the added diffusion term, it is more appropriately termed the 'Stabilization term'.

$$\underbrace{\sum_{e} \int_{\Omega_e} (\underline{v} \cdot \nabla\Psi)\tau_{SUPG} \left(\dot{\underline{\tilde{v}}} + (\underline{v} \cdot \nabla\underline{\tilde{v}}) - \upsilon\nabla^2\underline{\tilde{v}} + \nabla\underline{\tilde{p}} - \underline{f}\right) d\Omega_e}_{Stabilization\ Term}, \tag{6.9}$$

Note that $\underline{v}$ is the exact velocity of the convective term.

6.2 Other Stability Issues

Although the convective term is a prime cause of instability for high Reynolds flows, the formulation of the pressure interpolation functions also may have numerical instabilities associated with them. It was found by Ladyzhenskaya (1969), Babuška (1970/71) and Brezzi (1974) that certain types of elements, such as the Q2Q1 element used in this current research effort, can provide a guaranteed existence and unique solution for fluid analysis, thereby making the solution stable. The fact that an LBB compliant element is being used for this

research, is the reason why the numerical instabilities associated with the pressure will be neglected. It was also noted that an LBB compliant element can help with numerical stability when solving incremental schemes such as transient problems [Guermond and Quartapelle (1998)].

The mass term, denoted by [*M*] in Equation 2.32 also can provide numerical instabilities. It has been proven that using a 'lumped mass' term in place of the actual mass term can significantly increase stability. It has been documented that for a 9-noded element, the 'lumped mass' term stabilizes a majority of problems, even in convection dominated situations [Donea et al. (1982)]. Therefore stability of transient problems will be furthered by the use of 'lumped mass' terms.

6.3 Recent Research for the Stability Term

The stability term is outlined above and expressed in Equation 6.9. For traditional one-dimensional problems τ, shown in Equation 6.8, is calculated by using $\frac{\overline{\upsilon}}{\|\underline{a}\|^2}$ shown in Equation 6.7. However recent analyses involving this stabilization parameter, showed that it needs to be modified, element by element, to associate to current complications that arise due to possible high velocity gradients, diffusion and transient time steps. Although this is a current area of research, two methods to calculate the τ stability parameter have been developed and are well-known.

The first method for the SUPG technique of stabilization was introduced by Tezduyar et al. (1992), which is based on a previous formulation of a stability parameter for compressible flows. The stability parameter was based on three factors, transient time scale, high velocity, and added diffusion. Each term is weighted and can be seen in Equation 6.10.

$$\tau_{SUPG1} = \left[\underbrace{\left(\frac{2}{\Delta t} \right)^r}_{Transient} + \underbrace{\left(\frac{2\left\| v^e \right\|}{h^{\#}} \right)^r}_{Velocity} + \underbrace{9\left(\frac{4\upsilon}{\left(h^{\#} \right)^2} \right)^r}_{Diffusion} \right]^{-1/r}, \tag{6.10}$$

where Δt is the time step, v^e is the elemental velocity vector, r is defined as a stability constant that is traditionally set to 2, and $h^{\#}$ is a local length scale. The local length scale is defined to be equal to the diameter of a circle which is area-equivalent to the elemental area. Results using this formulation are discussed and solutions are shown to be effective in Tezduyar (1992) and Elias et al. (2006).

The second method was introduced by Tezduyar and Osawa (2000) but it deals with the calculations in terms of the second norms of elemental matrices associated with the modified weighted-residual stability term. The stability term is shown in Equation 6.9. This term can be broken up into elemental equations, using the Galerkin finite element approach, of the following form:

$$\begin{aligned} \left[\tilde{k} \right] &= \int_{\Omega_e} \left(\underline{v} \cdot \nabla \Psi \right) \left(\underline{v} \cdot \nabla \underline{\tilde{v}} \right) d\Omega_e, \\ \left[\tilde{c} \right] &= \int_{\Omega_e} \left(\underline{v} \cdot \nabla \Psi \right) \underline{\tilde{v}} \; d\Omega_e, \end{aligned} \tag{6.11}$$

where the terms involving the viscosity vanishes for quadrilateral geometries and are insignificant for isoparametric elements [Tezduyar and Osawa (2000)]. The term involving the pressure does not need to be stabilized because the Q2Q1 elements are LBB compliant and the source term is neglected because the problems analyzed in this research do not have source terms.

These elemental equations can be restructured to include the Galerkin weighted-residual method for approximating the velocities and be made into matrices of the following form:

$$\begin{bmatrix} [\tilde{k}] & [0] & [0] \\ [0] & [\tilde{k}] & [0] \\ [0] & [0] & [0] \end{bmatrix}^e \begin{Bmatrix} \{v_x\} \\ \{v_y\} \\ \{P\} \end{Bmatrix}^e$$
$$\begin{bmatrix} [\tilde{c}] & [0] & [0] \\ [0] & [\tilde{c}] & [0] \\ [0] & [0] & [0] \end{bmatrix}^e \begin{Bmatrix} \{\dot{v}_x\} \\ \{\dot{v}_y\} \\ \{\dot{P}\} \end{Bmatrix}^e \tag{6.12}$$

where the coefficient matrices shown are defined as:

$$\tilde{k}_{ij} = \int_{\Omega_e} (\underline{v} \cdot \nabla \Psi_i)(\underline{v} \cdot \nabla \Psi_j) d\Omega_e,$$
$$\tilde{c}_{ij} = \int_{\Omega_e} (\underline{v} \cdot \nabla \Psi_i) \Psi_j \, d\Omega_e, \tag{6.13}$$

The τ term in this SUPG method is determined by the second norms of these two elemental equations. This method is a derivative of the previous one described, where the terms can again be related to high velocity, transient time scale, and added diffusion respectively.

$$\tau_{SUPG2} = \left(\frac{1}{\tau_{S1}^r} + \frac{1}{\tau_{S2}^r} + \frac{1}{\tau_{S3}^r} \right)^{-1/r}, \tag{6.14}$$

where the terms inside the parenthesis are:

$$\tau_{S1} = \underbrace{\left(\frac{\|c\|}{\|\tilde{k}\|} \right)}_{Velocity}, \quad \tau_{S2} = \underbrace{\left(\frac{\Delta t}{2} \frac{\|c\|}{\|\tilde{c}\|} \right)}_{Transient}, \quad \tau_{S3} = \underbrace{\left(\left(\frac{\|c\|}{\|\tilde{k}\|} \right)^2 \frac{\|v^e\|^2}{\upsilon} \right)}_{Diffusion}, \tag{6.15}$$

It has been noted that the stability parameter second norms can be calculated for nodal equations, degree-of-freedom equations, or elemental equations [Tezduyar (2005)]. The elemental calculations of the stability parameter will be implemented, where appropriate, in this research, due to less computational effort necessary.

6.4 Analytical Comparison of SUPG Stability Parameters

To compare the two stability parameters, τ_{SUPG1} and τ_{SUPG2}, the cavity flow problem, analyzed in Chapter 4, will be reanalyzed implementing τ_{SUPG1} and τ_{SUPG2}. The following graphical data compares the stability parameter solutions to the base case solution, which does not use any stability. The cases of Reynolds number at 400, 1000, and 1500 were analyzed and compared between various mesh sizes. The 23 non-uniform mesh was discretized on the horizontal and vertical axes by [0.005 0.010 0.030 0.060 0.100 0.150 0.200 0.250 0.300 0.375 0.450 0.525 0.600 0.675 0.750 0.800 0.850 0.900 0.940 0.970 0.990 0.995 1.000] and is shown in Figure 50 where the circles represent nodes inside the mesh.

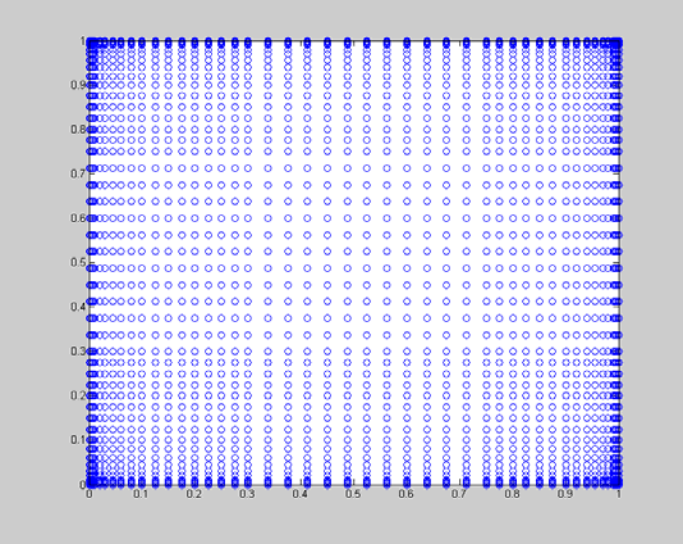

Figure 50: 23 non-uniform mesh discretization for stability comparison

The 15 non-uniform mesh was discretized on the horizontal and vertical axes by [0.0125 0.025 0.0417 0.0667 0.125 0.200 0.375 0.625 0.800 0.875 0.9333 0.9583 0.975 0.9875 1.000] and is shown in Figure 51.

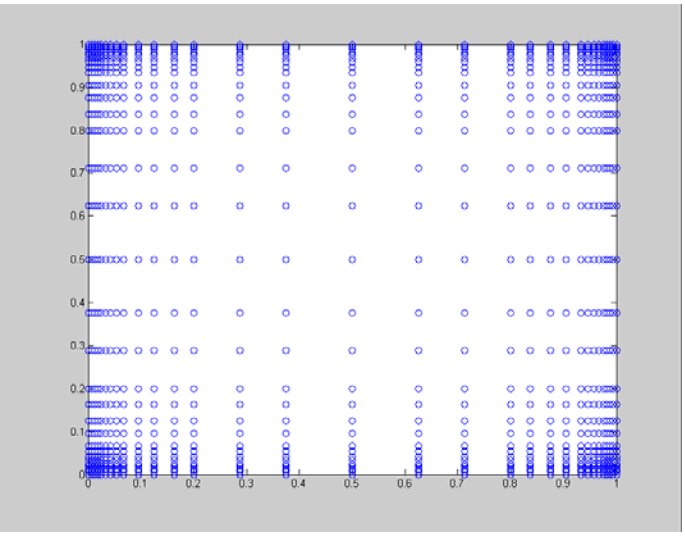

Figure 51: 15 non-uniform mesh discretization for stability comparison

It is important to note that these two cases were chosen to compare the increasing Reynolds flows because without stability the high velocity gradients and pressures at the upper two corners can be stabilized. The 15 non-uniform mesh demonstrates the stability issue because it a courser mesh than the 23 non-uniform mesh.

In addition a 20 uniform discretization of the domain was also analyzed for a Reynolds number flow at 1000. This was conducted so that the upper two corners were not discretized very well, leading to high velocity gradients and pressures inside each element, which should be stabilized by the introduction of the SUPG method. Figure 52 shows the 20 uniform mesh discretization.

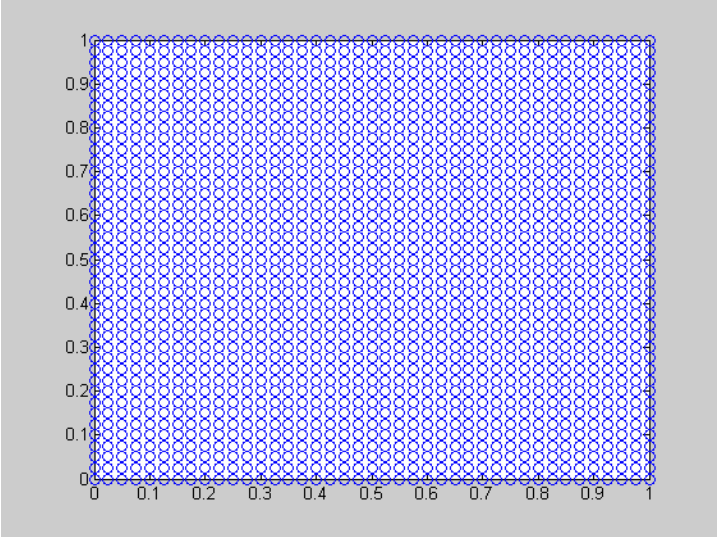

Figure 52: 20 uniform mesh discretization for stability comparison

The first analysis will be on a Reynolds number flow of 400. This Reynolds number is not really considered a highly convective case, but will serve as a low end study for convective flows. Figure 53 shows the error of the cavity flow problem over iteration loops, analyzed at a Reynolds number of 400 for a 23 non-uniform mesh and 15 non-uniform mesh. The iterative convergence tolerance was set to 2% for a fully implicit iterative scheme and all of the following graphs for Chapter 6 show the error of each iteration versus the iteration where the tolerance was calculated. Note that the error calculation is the same as in Chapter 4, Equation 4.6.

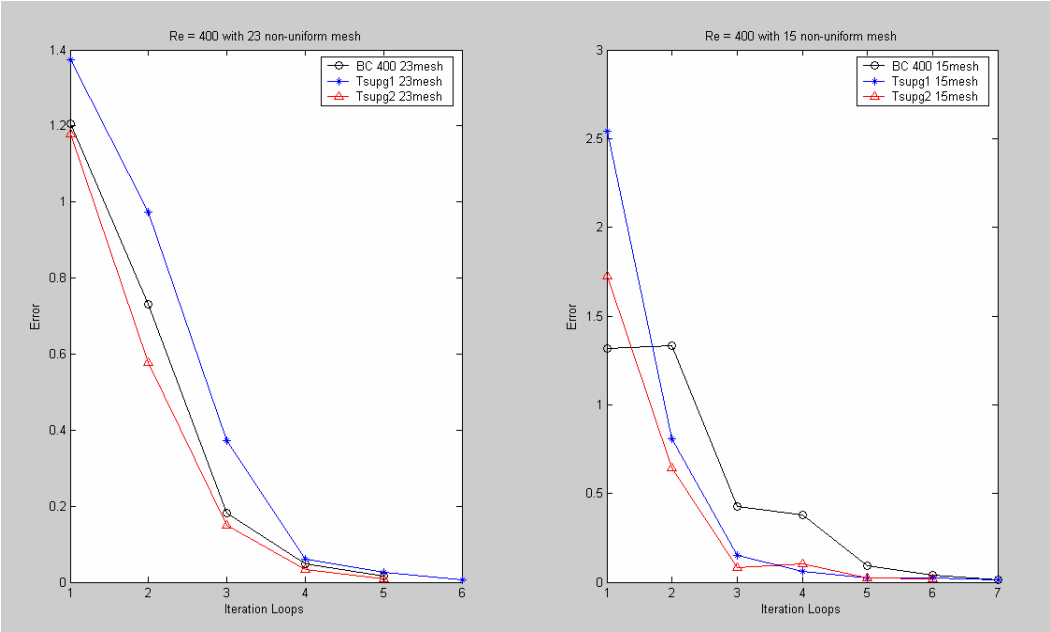

Figure 53: Stability comparison of Re = 400 for 23 and 15 non-uniform meshes

The circle line represents the base case, where no stability was introduced. The star line represents τ_{SUPG1}, while the triangle line represents τ_{SUPG2}.

Figure 53 shows the low end of the stability parameters comparison study at a Reynolds number 400. The 23 non-uniform mesh graph shows that all three cases have relatively good stability, shown by relatively smooth curves. For the 15 non-uniform mesh the numerical results of the base case exhibit some numerical instability but the stabilized cases do not.

The second analysis is for a Reynolds Number flow of 1000. This Reynolds number is considered the start of highly convective flow cases. Figure 54 shows the cavity flow problem analyzed at a Reynolds number of 1000 for a 23 non-uniform mesh and 15 non-uniform mesh.

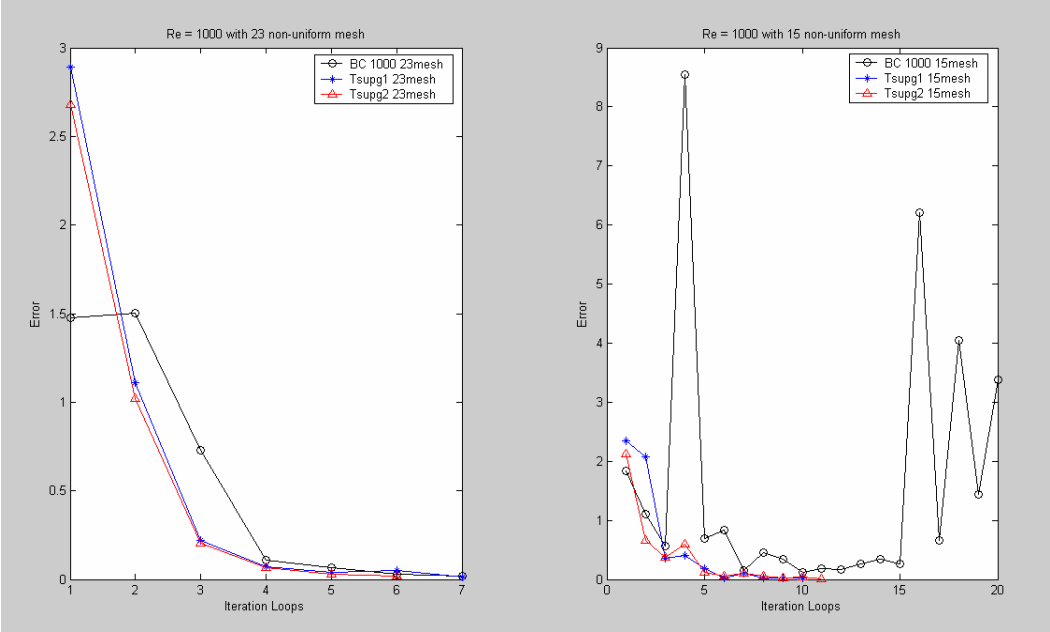

Figure 54: Stability comparison of Re = 1000 for 23 and 15 non-uniform meshes

The circle line represents the base case, where no stability was introduced. The star line represents τ_{SUPG1}, while the triangle line represents τ_{SUPG2}.

Figure 54 shows similar results as Figure 53 for the 23 non-uniform mesh cases, where the two stability parameter cases converged very nicely, however the base case had slight numerical instability. For the case of a 15 non-uniform mesh, the base case did not stabilize at all. The stability parameter cases both stabilized but the τ_{SUPG1} case stabilized one step sooner than the τ_{SUPG2} case.

The third analysis is for a Reynolds Number flow of 1000, but it will use the 20 uniform mesh. Figure 55 shows the cavity flow problem analyzed at a Reynolds number of 1000 for a 20 uniform mesh.

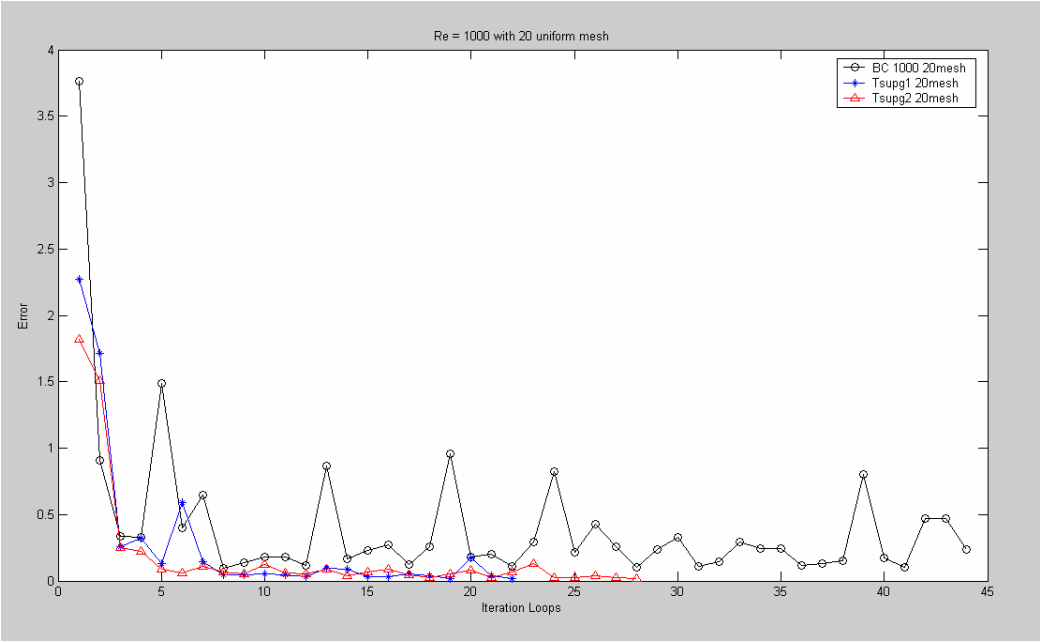

Figure 55: Stability comparison of Re = 1000 for 20 uniform mesh

The circle line represents the base case, where no stability was introduced. The star line represents τ_{SUPG1}, while the triangle line represents τ_{SUPG2}.

Figure 55 shows the 20 uniform mesh results and it is obvious that the base case does not converge. Both stabilization parameter cases stabilized, however the τ_{SUPG1} case stabilized after 22 loops, where the τ_{SUPG2} case stabilized after 28 loops. An inference can be drawn from this data that the τ_{SUPG1} case may be better suited for courser meshes.

The final analysis is for a Reynolds Number flow of 1500. This Reynolds number is considered a highly convective flow case. Figure 56 shows the cavity flow problem analyzed at a Reynolds number of 1500 for a 23 non-uniform mesh and 15 non-uniform mesh.

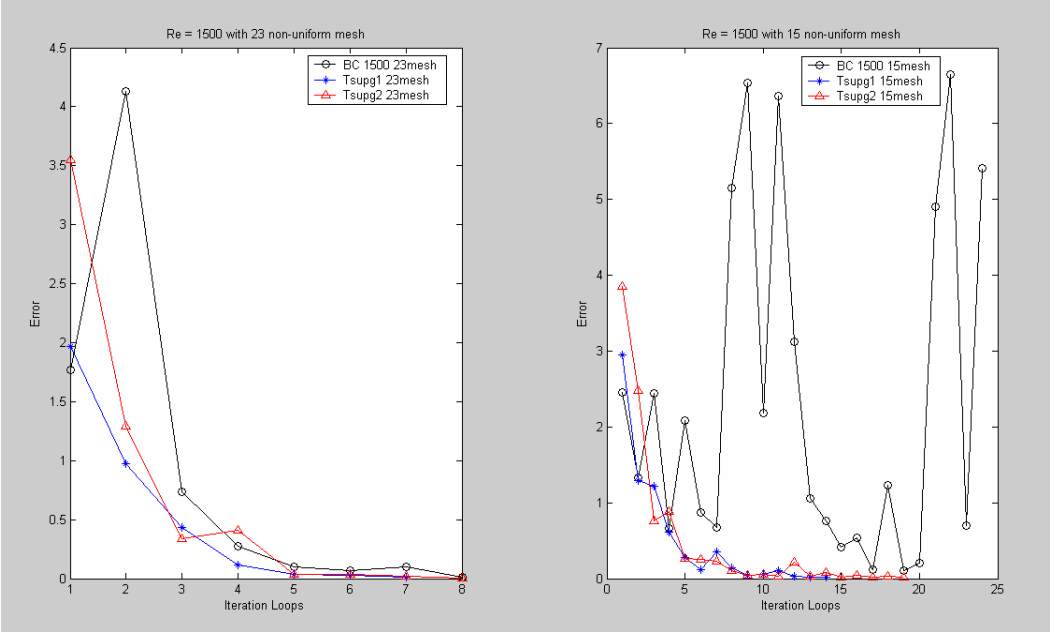

Figure 56: Stability comparison of Re = 1500 for 23 and 15 non-uniform meshes

The circle line represents the base case, where no stability was introduced. The star line represents τ_{SUPG1}, while the triangle line represents τ_{SUPG2}.

Figure 56 (left) shows that all three cases were able to converge. The τ_{SUPG1} case converged one step sooner than the τ_{SUPG2} and base cases. Comparing the data from the 15 non-uniform mesh, the base case was not able to achieve numerical stability, where both stability parameter cases were able to stabilize. The τ_{SUPG1} case converged after 14 loops and the τ_{SUPG2} case converged after 19 loops. The previous inference that τ_{SUPG1} may be better suited for courser meshes, to converge faster is aided by the fact that under a courser 15 non-uniform mesh, it was able to stabilize faster once again.

For this study the two stability parameter cases performed very well. It was noted that for courser meshes, where previous problems arose, the τ_{SUPG1} case seemed to stabilize quicker than the τ_{SUPG2} case. Overall a faster convergence will drop the computational effort

associated with the iterative loops. For situations where stability is needed, these results conclude that the τ_{SUPG1} case will be utilized.

SECTION 2

7 Euler-Bernoulli Beam Theory and Analysis

Preface

This section analyzes a cantilevered beam using Euler-Bernoulli beam theory, the finite element method and the Galerkin solution technique. The beam is a one-dimensional representation of the marine propulsion device that is expected to be analyzed in future work without the piezoelectric actuation. The natural frequencies of the beam are found and compared to published results.

7.1 Basic Concepts, Governing Equations and FE Formulation

In the Euler-Bernoulli beam theory, it is assumed that plane cross sections perpendicular to the axis of the beam remains plane and perpendicular to the axis after deformation. The kinematic relationships that exist on a point, or differential element, of a beam are illustrated in the following Figure and are mathematically expressed below. Figure 57 shows a differential element, dx, of a beam with reaction moments, M_z, transverse shear components, V, distributed transverse load per length, $q(x)$, and the elastic foundation modulus, c_f.

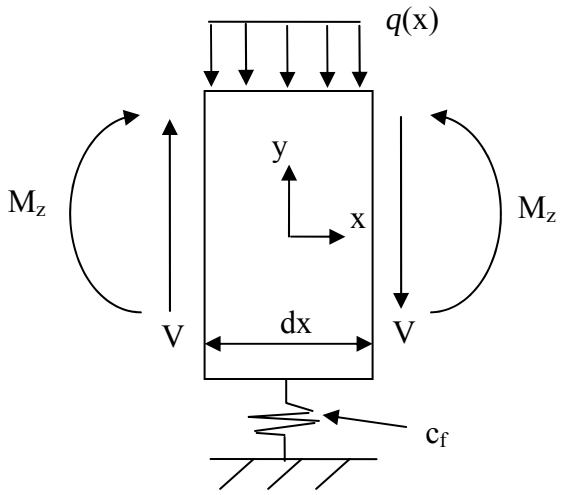

Figure 57: Differential element of a beam under load

$$-\frac{dV}{dx}+c_f \mathrm{w}=q,$$
$$-\frac{dM_z}{dx}+V=0,$$
$$M_z=-EI\frac{d^2\mathrm{w}}{dx^2},$$

The governing equation of the transverse deflection, w, neglecting rotary inertial effects is:

$$\rho A\frac{d^2\mathrm{w}}{dt^2}+\frac{d^2}{dx^2}\left(EI\frac{d^2\mathrm{w}}{dx^2}\right)+c_f \mathrm{w}=q(x), \tag{7.1}$$

where ρ is the mass density per unit length, A is the cross sectional area, E is the modulus of elasticity, I is the second moment of area about the neutral axis, z-axis, of the beam, q(x) is the distributed transverse load, c_f is the elastic foundation modulus, and w is the transverse deflection of the beam. The elastic foundation modulus will not be used for the present work so it will be neglected for the remainder of the calculations and q will be considered a constant load over each element for the remainder of the calculations. The local domain is one-dimensional between two nodes and is expressed $\Omega_e = [x_e:x_{e+1}]$.

The weak formulation of Equation 7.1 is:

$$\int_{\Omega_e}\left(\Psi_i \rho A\frac{d\mathrm{w}}{dt}+EI\frac{d^2\Psi_i}{dx^2}\frac{d^2\mathrm{w}}{dx^2}-\Psi_i q\right)dx+\left[\Psi_i\frac{d}{dx}\left(EI\frac{d^2\mathrm{w}}{dx^2}\right)-\frac{d\Psi_i}{dx}EI\frac{d^2\mathrm{w}}{dx^2}\right]_{x_e}^{x_{e+1}}=0, \tag{7.2}$$

The marine propulsion device being analyzed is considered to have cantilevered boundary conditions. The four appropriate boundary conditions for a cantilevered beam are addressed:

$$\begin{aligned}
&\mathrm{w}_0=\left.\frac{d\mathrm{w}}{dx}\right|_{x=0}=0,\\
&EI\left.\frac{d^2\mathrm{w}}{dx^2}\right|_{x=L}=M_{z0},\\
&\left[\frac{d}{dx}\left(EI\frac{d^2\mathrm{w}}{dx^2}\right)\right]\Bigg|_{x=L}=0,
\end{aligned} \tag{7.3}$$

Following the weak formulation of the governing equation, the interpolation functions must be formulated. The interpolation functions are identified with the need to be continuous with non-zero derivatives up to the order of two. The approximation of the displacement, $\mathrm{w_h}$, over a finite element should be twice differentiable and satisfy the essential boundary conditions of:

$$\mathrm{w}_h^e(x_e)=\mathrm{w}_1^e,\quad \mathrm{w}_h^e(x_{e+1})=\mathrm{w}_2^e,\quad \theta_h^e(x_e)=\theta_1^e,\quad \theta_h^e(x_{e+1})=\theta_2^e, \tag{7.4}$$

where θ is the slope at the specified point.

The family of Hermite cubic interpolation functions were chosen because they satisfy the aforementioned needs. Equation 7.5 shows the equations and Figure 58 shows the functions over the local coordinates, or unit element.

$$\Psi_1^e = 1 - 3\left(\frac{\bar{x}}{l_e}\right)^2 + 2\left(\frac{\bar{x}}{l_e}\right)^3, \quad \Psi_2^e = -\bar{x}\left(1 - \frac{\bar{x}}{l_e}\right)^2,$$
$$\Psi_3^e = 3\left(\frac{\bar{x}}{l_e}\right)^2 - 2\left(\frac{\bar{x}}{l_e}\right)^3, \quad \Psi_4^e = -\bar{x}\left[\left(\frac{\bar{x}}{l_e}\right)^2 - \left(\frac{\bar{x}}{l_e}\right)\right], \tag{7.5}$$

where $\bar{x}$ is the local coordinate and l_e is the length of the element

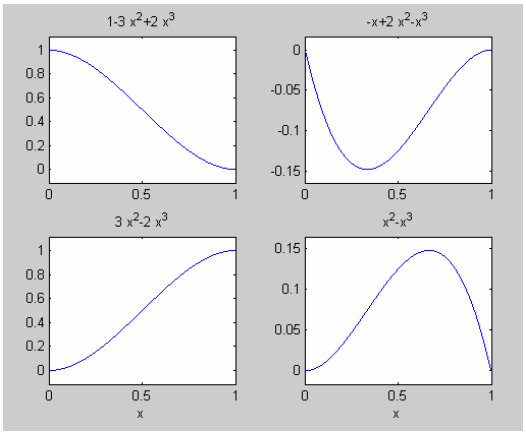

Figure 58: Graphs of the four functions on a unit element

Using the interpolation functions and the fact that the approximation solution is defined as:

$$w(x,t) = \sum_{j=1}^{n} w^j(t)\Psi_j(x), \tag{7.6}$$

This leads to a finite element model formulation of the following form:

$$[M^e]\begin{Bmatrix} \ddot{w} \\ \ddot{\theta} \end{Bmatrix} + [K^e]\begin{Bmatrix} w \\ \theta \end{Bmatrix} = \{F^e\} + \{Q^e\}, \tag{7.7}$$

The coefficient matrices of the finite element model are:

$$M_{ij}^{e} = \int_{x_e}^{x_{e+1}} \left(\rho A \Psi_i^e \Psi_j^e\right) dx$$

$$K_{ij}^{e} = \int_{x_e}^{x_{e+1}} \left(EI \frac{d^2\Psi_i^e}{dx^2} \frac{d^2\Psi_j^e}{dx^2} \right) dx$$

$$F_i^e = \int_{x_e}^{x_{e+1}} \left(\Psi_i^e q\right) dx$$

$$Q^e = \begin{Bmatrix} \left[\frac{d}{dx}\left(EI \frac{d^2 w}{dx^2} \right) \right]\Big|_{x_e} \\ \left(EI \frac{d^2 w}{dx^2} \right)\Big|_{x_e} \\ -\left[\frac{d}{dx}\left(EI \frac{d^2 w}{dx^2} \right) \right]\Big|_{x_{e+1}} \\ -\left(EI \frac{d^2 w}{dx^2} \right)\Big|_{x_{e+1}} \end{Bmatrix} \tag{7.8}$$

7.2 Natural vibration of a beam and comparison of results

Consider the free vibration of an isotropic beam. The properties of the beam are not influential on the results, except the length-to-thickness ratio given as 100; this is considered thin beam analysis, which is close to the type of marine propulsion analyzed. The reason for only defining this property is that the end result is a non-dimensionalized number representing the frequency.

To obtain the solution for free vibration, the equation is reduced to the following eigenvalue problem:

$$-\omega^2 [M] + [K] = 0, \tag{7.9}$$

Using this form of the equation results were calculated using MATLAB software. The first four modes of a beam with $L/t_b = 100$ and 16 elements can be seen in Figure 59.

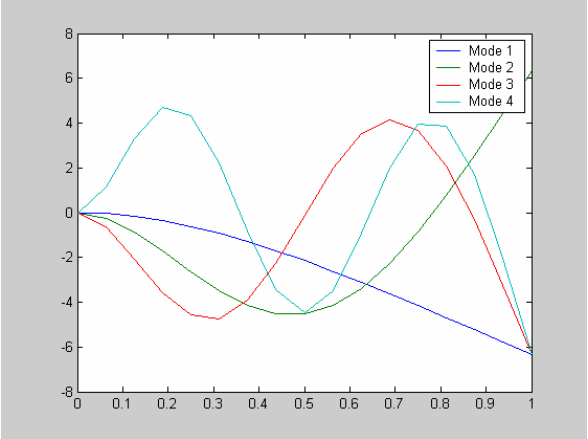

Figure 59: The first four modes of a beam with L/tb = 100 and 16 elements; all other data is unity

The results of the free vibration data are compared to published results in Table 3. To non-dimensionalize the natural frequency for Euler-Bernoulli beam theory, $\overline{\omega} = \omega L^2 \left(\rho A / EI\right)^{1/2}$, where L is the total length.

Mode shapes for a beam	$\overline{\omega}_1$	$\overline{\omega}_2$	$\overline{\omega}_3$	$\overline{\omega}_4$
Present Simulation	3.5160	22.0346	61.6997	120.9202
Reddy (2006)	3.5160	22.0345	61.6972	120.9019

The data found from the present simulation correlates very well to the published data [Reddy (2006)].

Table 3: Simulation vs. Published Results for Beam Mode Shapes

The MATLAB code used to formulate the beam model and analysis can be found in Appendix B.4.

8 Piezoelectric Theory

Preface

The history of piezoelectricity dates back to 1880 when Pierre and Jacques Curie discovered it in Rochelle Salt and quartz. Piezoelectricity and its effect allows a material to generate an electric charge with the application of pressure. Alternatively, in the presence of an electric field, the materials change shape. The materials that have piezoelectric properties allow ions to be moved more easily on some crystal axes than others. Piezoelectric properties coupled with a thin plate, or beam in one-dimension, allows for actuation properties. The properties are similar to the actuation found in bi-metallic metals. Applying two piezoelectrics to the fixed end of a cantilevered beam on opposite sides of the neutral surface and actuating them with a 180 degree phase shift in electrical voltage potential will result in the transverse bending from the orthogonal plane to the vertical axis of the piezoelectric device. This is the type of actuation expected to be used on the marine propulsion device being developed.

8.1 Piezoelectric Theory

For most piezoelectrics, external pressure (force) causes the deformation of a coordinate tetrahedron lattice in the material, shifting the gravity centers of the electric charges, creating a local polarization dipole to form – thus an electrical field is created. As stated above, the reverse is possible which induces a strain on the material and therefore a deformation. In other words the piezoelectric material changes shape when their electrical dipoles spontaneously align in electric fields causing deformation of the crystalline structure. To go into more depth about the piezoelectric effect is out of the scope of this thesis.

The piezoelectric constitutive relations are expressed in the following matrix form:

$$\begin{pmatrix} \underline{\varepsilon} \\ \underline{D} \end{pmatrix} = \begin{bmatrix} [\mathrm{S}] & [\mathrm{d}] \\ [\mathrm{d}]^T & [\mathrm{e}]^t \end{bmatrix} \begin{pmatrix} \underline{\sigma} \\ \underline{\mathrm{E}} \end{pmatrix}, \tag{8.1}$$

The coefficient matrices and vectors are defined as:

ε = The strain vector

D = The electric displacement vector

σ = The stress vector

E = The electric field vector

[S] = The elasticity compliance matrix

[d] = The piezoelectric strain coefficient matrix

$[e]^t$ = The electric displacement-field matrix

Expanding the matrix gives the following form:

$$\begin{pmatrix} \varepsilon_1 \\ \varepsilon_2 \\ \varepsilon_3 \\ \gamma_{23} \\ \gamma_{31} \\ \gamma_{12} \\ D_1 \\ D_2 \\ D_3 \end{pmatrix} = \begin{bmatrix} S_{11} & S_{12} & S_{13} & 0 & 0 & 0 & 0 & 0 & d_{31} \\ S_{12} & S_{22} & S_{23} & 0 & 0 & 0 & 0 & 0 & d_{31} \\ S_{13} & S_{23} & S_{33} & 0 & 0 & 0 & 0 & 0 & d_{33} \\ 0 & 0 & 0 & G_{23} & 0 & 0 & 0 & d_{15} & 0 \\ 0 & 0 & 0 & 0 & G_{13} & 0 & d_{15} & 0 & 0 \\ 0 & 0 & 0 & 0 & 0 & G_{12} & 0 & 0 & 0 \\ 0 & 0 & 0 & 0 & d_{15} & 0 & e_{11} & 0 & 0 \\ 0 & 0 & 0 & d_{15} & 0 & 0 & 0 & e_{22} & 0 \\ d_{31} & d_{31} & d_{33} & 0 & 0 & 0 & 0 & 0 & e_{33} \end{bmatrix} \begin{pmatrix} \sigma_1 \\ \sigma_2 \\ \sigma_3 \\ \tau_{23} \\ \tau_{31} \\ \tau_{12} \\ E_1 \\ E_2 \\ E_3 \end{pmatrix}, \tag{8.2}$$

where the axes directions are shown in Figure 60.

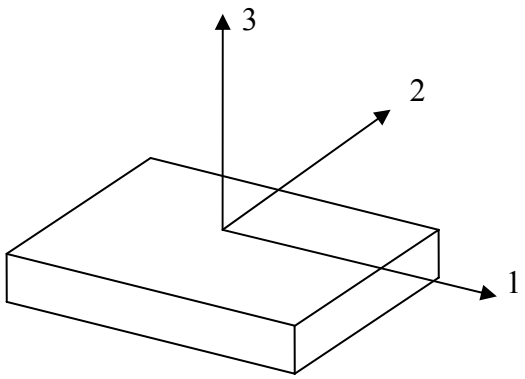

Figure 60: Axes directions associated with the above matrix, Equation 8.2

The particular piezoelectric chosen, the Sonox P505 (5A1), for this project is made by the Smart Material Corporation. The material characteristics are:

Modulus of Elasticity = $E_p = 70 \cdot 10^9$

Density = $\rho_p = 7800$ kg/cm^3

Poisson's Ratio = $\nu_p(x,y) = 0.3$

Relative Dielectric Constant = $K_{33}T = 1850$

Charge Constants = $d_{31} = -185\ 10^{-12}$ C/N
$d_{33} = 440\ 10^{-12}$ C/N
$d_{15} = 560\ 10^{-12}$ C/N

Compliance Constants = $S_{11} = 18.5\ 10^{-12}$ m^2/N
$S_{22} = S_{11}$
$S_{33} = 20.7\ 10^{-12}$ m^2/N
$S_{12} = -S_{11} * \nu_p$
$S_{13} = -S_{33} * \nu_p$
$S_{23} = S_{13}$
$G_{12} = 2 * S_{11} * (1+\nu_p)$
$G_{13} = 2 * S_{33} * (1+\nu_p)$
$G_{23} = G_{13}$

Electric Displacement Field Constants: $e_{11} = K_{33}T * V_p$
$e_{22} = e_{11}$
$e_{33} = e_{11}$

where V_p = Permittivity of a vacuum = $8.8541878176204\ 10^{-12}$

The piezoelectric chosen extends in a transverse mode when an electric field is produced between its two electrical contacts. The transverse mode is defined in the Figure 61.

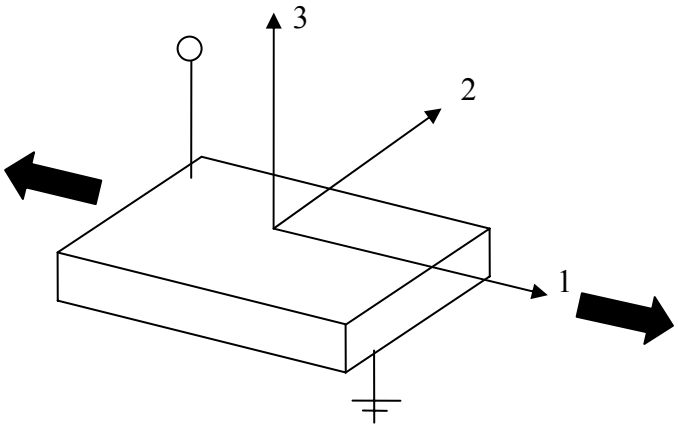

Figure 61: Transverse mode of piezoelectric

8.2 ANSYS 9.0 modeling

ANSYS 9.0 software is a comprehensive finite element software package that is widely used in industry and academia. It has the ability to solve for piezoelectric elements, which is the reason it is being used as a comparison tool for the models in this thesis. Using the ANSYS 9.0 software required different forms of the data listed above. MATLAB code was written to provide the correct forms of data that ANSYS 9.0 required, see Appendix B.4.

To allow for piezoelectric effects to take place it is necessary to utilize the 20-node brick solid 226 element in ANSYS 9.0. This requires that the ANSYS 9.0 models produced in all analysis be in 20-node brick solid elements. The following process outlines the steps needed to complete a three-dimensional piezoelectric element, using the material properties listed above, with necessary boundary conditions in ANSYS 9.0:

Preprocessor:

Element type - Coupled Field - Brick20node 226
Options - Piezoelectric

Material Model - Structural - Linear - Elastic - Anisotropic - Enter [D] "stiffness form" from MATLAB code
- Density - Add density

Electromagnetics - Relative Permittivity - Orthotropic - Enter [perx,y,z] values from MATLAB code

Piezoelectrics - Piezoelectric Matrix - Enter Piezoelectric stress matrix [e] from MATLAB code

Modeling - Create - Volumes - Block - By Dimensions

Meshing - Mesh Tool - Element Attributes
- Size Controls - Set Lines - Do all lines (3 sets)
- Mesh - Volumes - Hex - Mapped - MESH

Solution:

Define Loads - Apply - Structural - Displacement - On Areas
NOTE: Set structural BC (Displacement ux = uy = uz = 0)
Set Voltage BC (Top Area = 100, Bottom = 0)

Solve - Current LS

9 Laminated Piezoelectric-Beam Theory and Analysis

Preface

This section analyzes a cantilevered beam using Euler-Bernoulli beam theory integrating laminated piezoelectric-beam elements. The beam is a one-dimensional representation of the marine propulsion device that is expected to be analyzed in future work. The natural frequencies of the beam and the forced vibration natural frequencies are found and compared to results from ANSYS 9.0 software. The natural modes of vibration are of interest because the greatest vibration amplitude of the free end is achieved with the lowest input voltage near resonance frequency.

9.1 Laminated Piezoelectric-Beam Element Constitutive Relations and FE Formulation

The laminated piezoelectric-beam element adopts the basic assumptions that the piezoelectric is symmetrically applied to opposite sides of the neutral axis to the beam, the piezoelectric has perfect, thin bonding to the beam, and the lateral effects are neglected.

Under these conditions the beam element is shown in Figure 62.

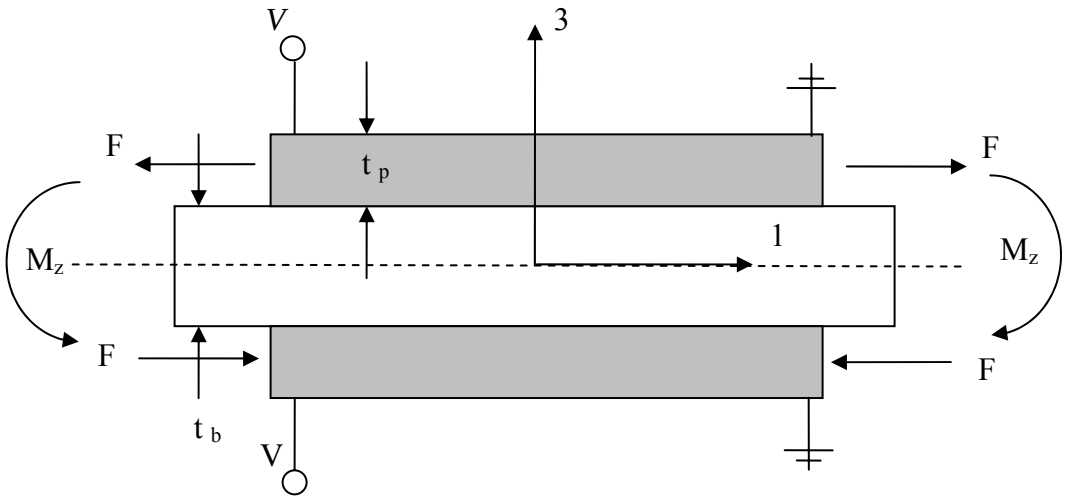

Figure 62: Laminated piezoelectric-beam element

where t_b is the thickness of the beam, t_p is the thickness of the piezoelectric, F denotes a force due to the voltage difference, V, on the piezoelectric and M_z denotes the moment experienced in the beam.

From the constitutive relationships and the diagram above, the following proof of half of the moment on the beam is constructed:

$$\begin{aligned}
\sigma_1 &= Ed_{31}\left(\frac{V}{t_p}\right) = \frac{F}{A} = \frac{F}{w_p t_p}, \\
F &= Ed_{31}Vw_p, \\
\mathrm{M}_{1/2} &= F \times \left(\frac{1}{2}t_b + \frac{1}{2}t_p\right) = Ed_{31}Vw_p\left(\frac{1}{2}t_b + \frac{1}{2}t_p\right),
\end{aligned} \tag{9.1}$$

where w_p is the width of the piezoelectric.

The moment experienced on the beam element due to both piezoelectrics is:

$$\mathrm{M}_p = Ed_{31}Vw_p\left(t_b + t_p\right), \tag{9.2}$$

The piezoelectric produces an externally applied moment and therefore the equation above is added to the right hand side terms in the finite element modeling equation for a beam, Equation 7.7.

9.2 Natural and forced vibration of a laminated piezoelectric-beam

An Euler-Bernoulli beam theory model was analyzed using a 15 element mesh over a domain $\Omega = [0:1]$. All assumptions for Euler-Bernoulli beam theory and the piezoelectric theory are contained within this model. The 1 meter long cantilevered beam has two piezoelectrics on the element closest to the fixed cantilevered boundary condition, which is 0.125 meters in length. The other elements are defined by lengths of 0.0625 meters. Figure 63 shows the beam mesh with the laminated piezoelectric-beam element, along with lengths of its elements.

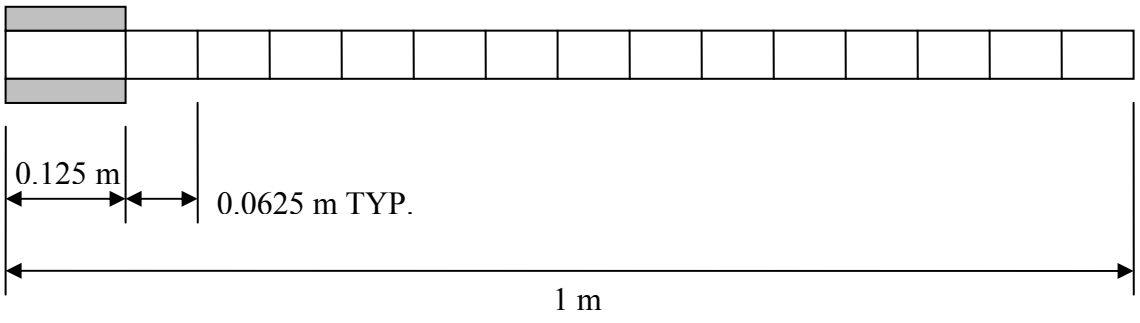

Figure 63: Mesh of laminated piezoelectric-beam analyzed

The modeling properties for the laminated piezoelectric-beam are:

$$E_b = 205\ 10^9$$
$$w_b = 0.2 \text{ m}$$
$$t_b = 0.002 \text{ m}$$
$$\rho_b = 7870 \text{ kg/cm}^3$$
$$t_p = 0.001 \text{ m}$$

where E_b = Modulus of Elasticity for the beam, w_b = width of the beam, t_b = thickness of the beam, ρ_b = density of the beam, and t_p = thickness of the piezoelectric. The properties for the piezoelectric can be found in Chapter 8.

The natural frequencies can be obtained by using Equation 7.9: $-\omega^2[M]+[K]=0$. Figure 64 shows the mode shapes of the first four natural vibration frequencies {1.9614, 11.9423, 32.4751, 61.6051} Hz.

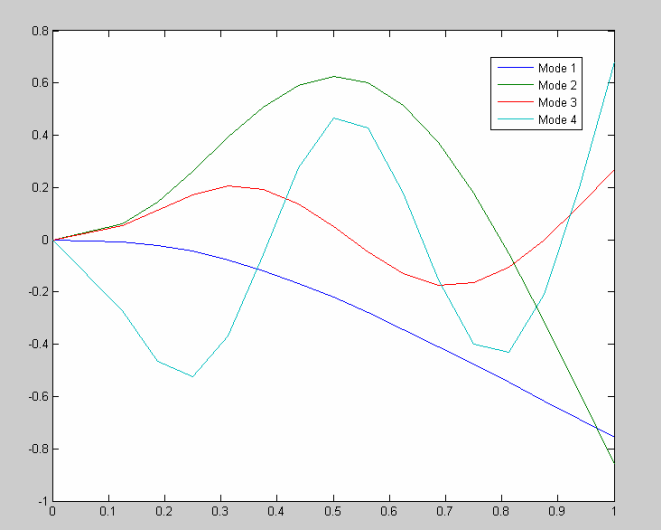

Figure 64: The first four free vibration modes of the laminated piezoelectric-beam model

Note that the first element from the cantilevered side, the laminated piezoelectric-beam element is stiffer than the other elements and therefore the natural frequency of the beam with piezoelectrics is higher than the bare beam, analyzed in Chapter 7.

The input voltage to the piezoelectric is a narrow white noise with a low cut-off frequency of 0 Hz and a high cut-off frequency of 75 Hz. The steady-state frequency response of the displacement amplitude at the tip of the beam is computed and displayed in Figure 65.

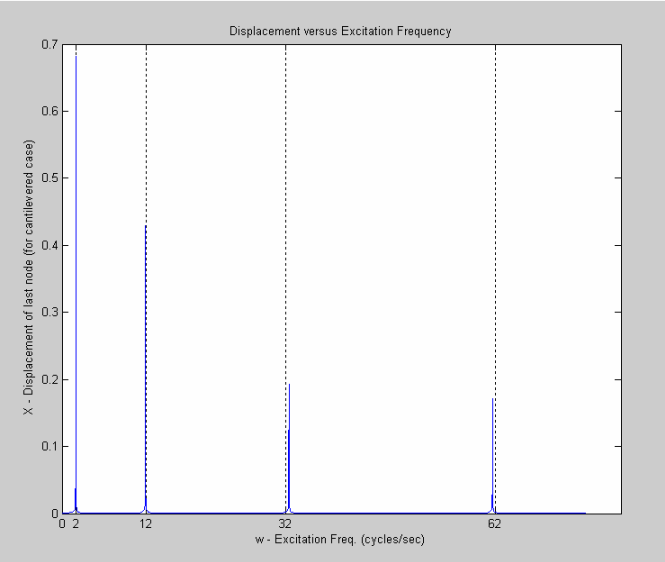

Figure 65: Natural modes of vibration under 100 volt actuation signal

It is shown that within the domain [0:75] Hz, there are four natural modes of vibration, f ~ {2, 12, 32, 62} Hz. These modes of vibration are the same as the natural modes of vibration analyzed previously, which would be expected.

9.3 ANSYS 9.0 analysis and comparison

To construct the piezoelectric model of the beam in ANSYS 9.0, a 3-D model is constructed as follows:

Preprocessor:

Element type - Solid – 20-node Brick 95

Material Model - Structural - Linear - Elastic – Isotropic – Add E and ν
- Density - Add density

Modeling - Create - Volumes - Block - By Dimensions
NOTE: Create beam and piezoelectric elements separately
- Booleans – Glue – Volumes: beam to piezoelectric

Meshing - Mesh Tool - Element Attributes
- Size Controls - Set Lines - Do all lines of volumes
- Mesh - Volumes - Hex - Mapped - MESH

Solution:

Analysis Type – New analysis – Modal
- Analysis Options – Block Lanzcos

Define Loads - Apply - Structural - Displacement - On Areas
NOTE: Set structural BC (Displacement ux = uy = uz = 0) only for areas that are part of beam, not the piezoelectric area

The 20-node, 3-D, solid brick element was chosen for the beam elements because the piezoelectric elements in ANSYS 9.0 are three-dimensional, 20-node elements (Chapter 8); both of these need to interface. Also the three-dimensional elements produce the most accurate model and can predict more modes such as the twisting modes, which is not included in the Euler-Bernoulli beam analysis conducted in Chapter 7. Table 4 compares the simulated MATLAB code results to the ANSYS 9.0 results and Figure 66 shows the mode shape results from ANSYS 9.0.

Comparison study to show 1-D versus 3-D modes of vibration

Case 1: Beam without piezoelectric elements 16 elements – each 1/16 long	f1	f2	f3	f4
Simulated Results:	1.6489	10.3337	28.9356	56.7085
ANSYS 9.0 Results:	1.7103	10.672	30.380	60.663
Case 2: Beam without piezoelectric elements 15 elements – 1/8 w/ rest 1/16 long	**f1**	**f2**	**f3**	**f4**
Simulated Results:	1.6489	10.3337	28.9357	56.7110
ANSYS 9.0 Results:	1.7259	10.767	30.883	62.339
Case 3: Beam with piezoelectric element 15 elements – 1/8 w/ rest 1/16 long First element is beam-piezoelectric	**f1**	**f2**	**f3**	**f4**
Simulated Results:	1.9614	11.9423	32.4751	61.6051
ANSYS 9.0 Results:	2.026	12.348	34.299	66.768

Results use the same material and modeling properties as the previous example for comparison and all results are in Hz.

Table 4: Simulation vs. ANSYS 9.0 Results for Laminated Piezoelectric-Beam Modes

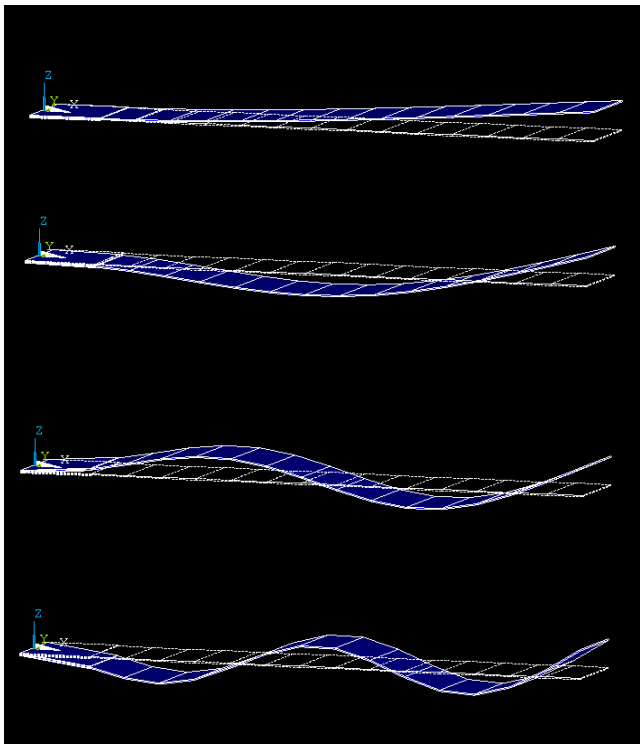

Figure 66: ANSYS 9.0 beam model with piezoelectric modes of vibration

Note that the modes of vibration in Figure 66 are modes 1, 2, 4, and 6. This can be explained by the fact that the analysis used for the MATLAB code can not predict twisting modes, while ANSYS 9.0 can because it uses a three-dimensional analysis; modes 3 and 5 are primarily twisting modes.

All the data compared is contained within a relatively low error scale meaning that the one-dimensional beam simulation prediction of the modes of vibration with or without the piezoelectric elements is very similar to the three-dimensional ANSYS 9.0 analysis.

The scope of this thesis is to demonstrate the possibility of creating marine propulsion due to one of the modes associated with a plate, or beam in 1-D. This same type of analysis can be done in conjunction with the fluid finite element analysis to obtain the modes of largest amplitude vibration, therefore giving the largest thrust forward for the marine propulsion device.

The MATLAB code used to formulate the laminated piezoelectric-beam model and analysis can be found in Appendix B.4. The MATLAB code used to formulate the constants for ANSYS 9.0 can be found in Appendix B.4 as well.

SECTION 3

10 Simplified Fluid Interaction

Preface

Fluid structure interaction problems are known for their very computationally intensive nature. There are current simulation programs that transfer load data between a computational fluid dynamics model and a finite element dynamics model. These simulations are difficult to set up and include very long computation times. Therefore in an effort to simplify some of this analysis a simplified fluid interaction problem is proposed that incorporates both the fluid and structure elements into one program. Due to time constraints this simplification will not directly include the beam elements; instead a pseudo-beam will be present in the analysis.

A simplified fluid interaction problem is presented with appropriate boundary conditions to mimic a 1-D beam, 2-D fluid structure interaction problem. The basic concepts of a fluid structure interaction problem are introduced and the major hurdles involved with solving this type of problem are addressed. To verify the first transient time step, velocity and pressure results are compared to ANSYS 9.0 simulation results. The results of this simulation are to help better understand the underwater marine propulsion mechanics: the evolution of pressure, velocity and vortices.

10.1 Problem Definition

The simplified fluid interaction problem is intended to model the experimental results obtained. It models a plane flow where the domain is the right-half space, or $\{x > 0\}$ and $\{-\infty < y < \infty\}$. The computational domain is condensed to only incorporate a small section of the positive right-half space: $\{0 < x < 1\}$ and $\{0 < y < 1\}$. The beam is situated at [0.5, 0]

and is 0.3571 meters long (approximately 1 foot long). The domain is discretized by a 20 X 19 non-uniform mesh of Q2Q1 elements.

The properties of the fluid (water at 20^oC) are:

Dynamic viscosity = μ= 0.001003 kg/m·s

Density = ρ = 998.29 kg/m^3

The boundary conditions are all considered to be 'open boundary conditions', which are essential and normal boundary conditions. The boundary conditions for the top (y = 1) and bottom (y = 0) sides of the domain set the velocity in the x-direction and the traction forces in the y-direction to be zero. The boundary conditions for the left (x = 0) and right (x = 1) sides of the domain set the velocity in the y-direction and the traction forces in the x-direction to be zero. These types of boundary conditions simulate open water on all sides and both the velocity and traction boundary conditions are required to satisfy the necessary amount of boundary conditions. Figure 67 shows a schematic of the simplified fluid interaction problem with labeled boundary conditions.

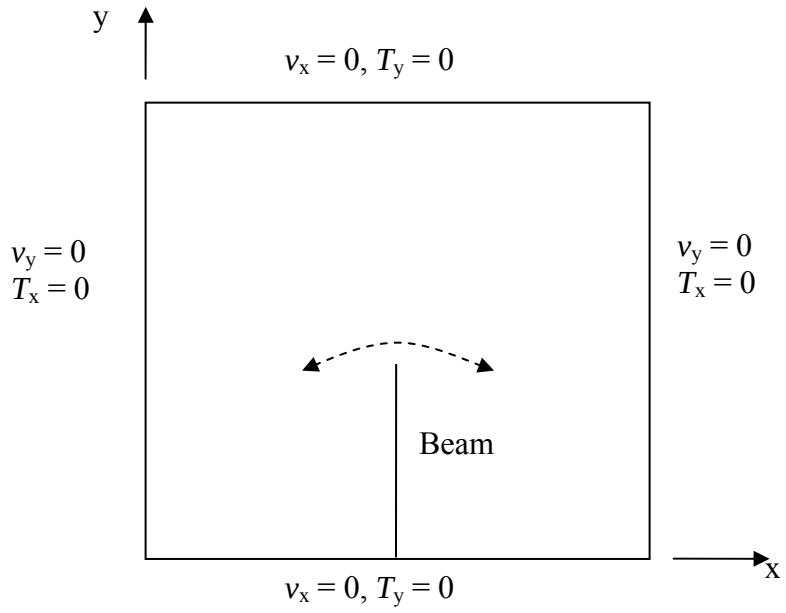

Figure 67: Boundary Conditions

The water is initially stationary and the beam swings through an arc of less than 10 degrees. The reason for this is that it simplifies the analysis so that the small angle theory can be used. That is, there is no change in the height of the nodal locations of the beam over the complete arc.

The mesh is a 20 X 19 non-uniform mesh refined around the beam. No consecutive pair of elements violates the standard ratio, greater than 2:1. The divisions for the non-uniform mesh in the x-direction are: [3/24, 6/24, 7/24, 8/24, 9/24, 9.5/24, 10/24, 10.5/24, 11/24, 12/24, 13/24, 13.5/24, 14/24, 14.5/24, 15/24, 16/24, 17/24, 18/24, 21/24, 1]. The divisions for the non-uniform mesh in the y-direction are: [2/21, 3/21, 4/21, 5/21, 5.5/21, 6/21, 6.5/21, 7/21, 7.5/21, 8/21, 8.5/21, 9/21, 9.5/21, 10/21, 11/21, 12/21, 13/21, 15/21, 1]. Figure 68 shows the non-uniform mesh where circles represent nodal locations.

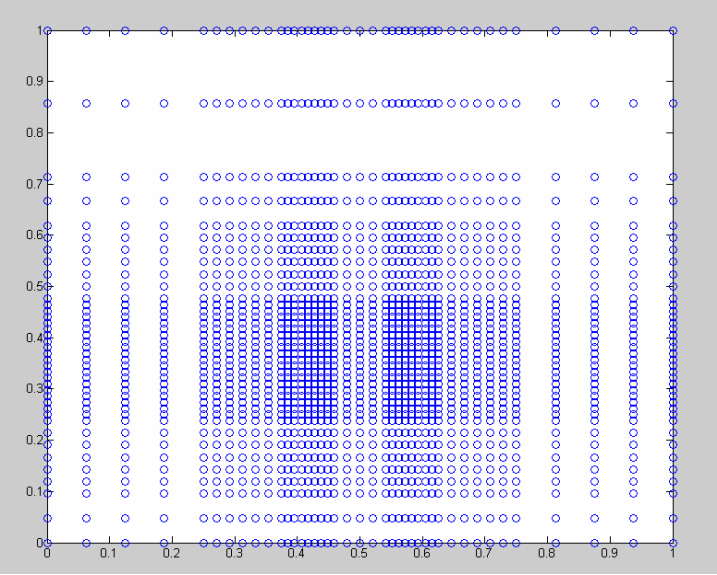

Figure 68: Mesh over the domain of the simplified fluid interaction

10.2 Adaptive Mesh

Developing a fluid structure interaction program involves creating an adaptive mesh for each new time step, based on the previous time step results. Typically for a fluid structure interaction problem, the mesh is generated at each step based on the deformed shape of the beam, however due to the complexity that this scenario involves a simplification was proposed, which pre-defines the beam's location at each time step. Knowing the beam's location allows the mesh to be generated beforehand and all of the appropriate matrices to be calculated before the program starts. This saves computational effort because over the course of one cycle to the next, the beams location is the same as the previous cycle. It should be pointed out again that this is not the case in a fully developed fluid structure interaction problem.

The change of the location of the beam over time renders the problem very complex. The elements in the vicinity of the beam are distorted, which requires isoparametric analysis to be conducted.

The small angle assumption is a critical assumption in this simplified fluid interaction problem. The beam 'swings' through a small arc, approximately 6 degrees to its peak, and therefore using the assumption, the height of the arc does not change. Meaning that the adaptive mesh nodes do not need to change vertically (y-direction), just horizontally (x-direction), which simplifies the computational intensity associated with the isoparametric analysis.

The simplified fluid interaction problem also assumes that the beam is rigid and swings like a pendulum at the bottom node [0.5, 0]. It is known that the first mode of a laminated piezoelectric-beam is not completely rigid, Chapter 9, but under the circumstances of a small angle, the beam will be modeled this way. Also this helps with reducing the coding complexity and computational effort. Figure 69 shows the first four views of the adaptive mesh around the beam. It is a condensed view of the entire mesh so that the differences between 4 consecutive time steps are distinguishable. The circles represent the nodes of the

mesh, the dashed lines represent the element boundaries and the solid line represents the beam.

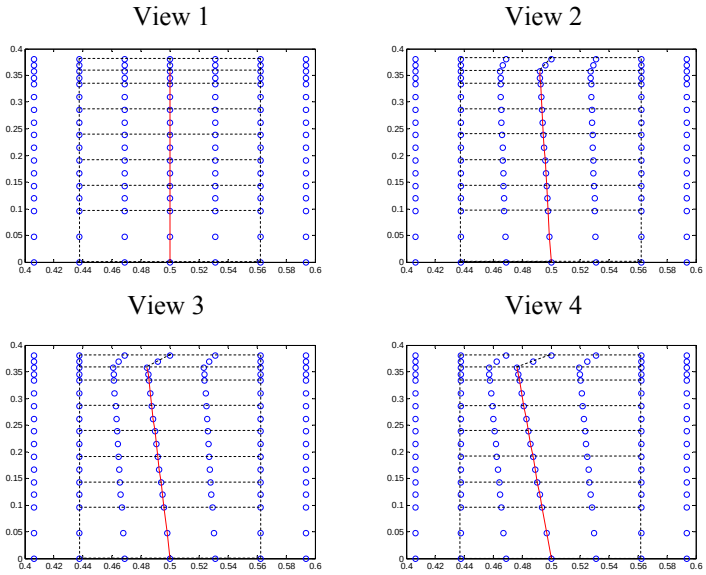

Figure 69: 2-D Adaptive Mesh - 4 consecutive views

10.3 Solution Technique

The solution for the simplified fluid interaction problem follows the same solution scheme presented in Chapter 5 (algebraic splitting technique of the Chorin-Temam projection method). The same type of transient analysis is implemented where the time step is decided upon by the frequency with which the beam oscillates. The convective term is handled in the same fashion as in Chapter 4 and Streamline-upwind Petrov-Galerkin (SUPG) stability is implemented over the whole solution domain to deal with the instability that will result when the beam switches from a positive direction to a negative direction, at its maximum peak.

The velocity of the beam is an input of the simulation program based on the frequency of the beam's oscillations and the displacement of the nodes over time. The no-slip assumption is adopted at the nodes of the beam; that is the velocity of the beam, due to the change in the adaptive mesh and time equals the velocity of the fluid at those nodes. Therefore the known velocities of the fluid at the beam's nodal locations are decided by inputs based on the

frequency and/or time step over the distance change from one adaptive mesh step to the next. The velocity values at the peak oscillation steps are taken as zero.

10.4 First Time Step Comparison to ANSYS 9.0

The first time step of the solution is constructed of all rectangular elements and the velocities are defined for the 2-D fluid at the beam nodal locations: [0.0347, 0.0694, 0.0868, 0.1042, 0.1215, 0.1389, 0.1563, 0.1736, 0.1823, 0.1910, 0.1997, 0.2083, 0.2170, 0.2257, 0.2344, 0.2431, 0.2517, 0.2604] m/s. These values were found by dividing the mesh distance from the original position to the second position by the time step. The time step was decided upon to give the beam a frequency of approximately 1 Hz, mimicking the experimental results found. To obtain approximately 1 Hz frequency, the time step was set at 0.04 seconds. The solution and mesh of the first time step are easily constructed in ANSYS 9.0. The ANSYS 9.0 results are compared to the first step transient analysis results obtained from the MATLAB simulation program to validate consistent initial results.

The results from the MATLAB simulation program first time step are shown in Figures 70, 71 and 72. Figure 70 shows the velocity vector field, Figure 71 shows the pressure contours, and Figure 72 shows the particle streamline plot.

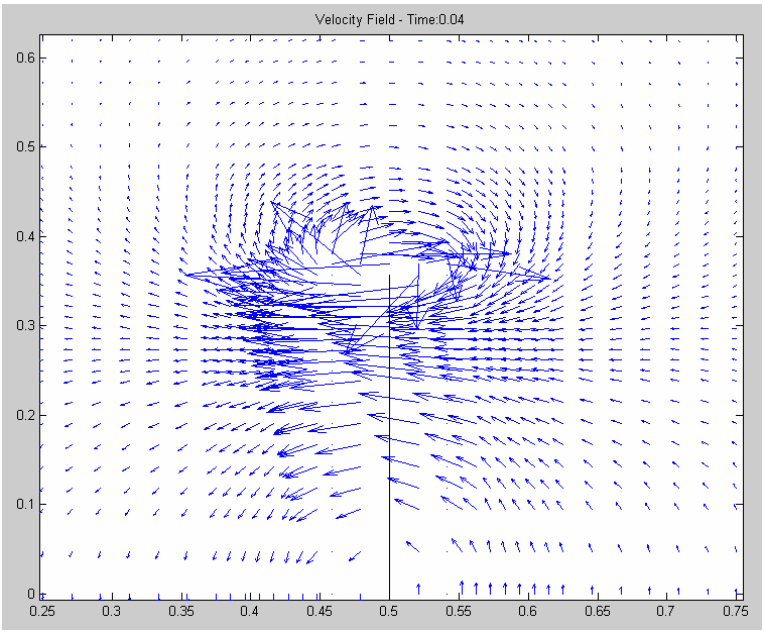

Figure 70: Velocity vectors for first time step of simplified fluid interaction problem y-position: {0:0.65}, x-position {0.25:0.75}

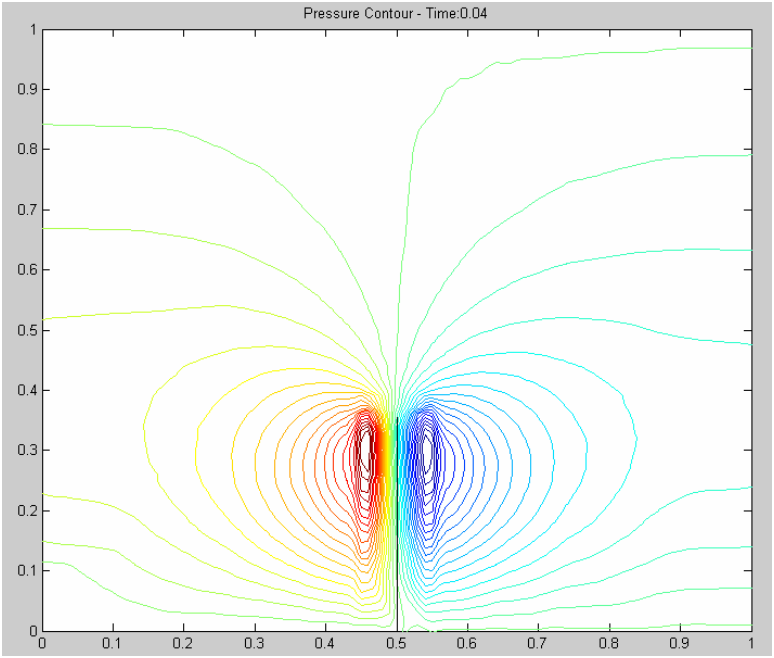

Figure 71: Pressure contours for first time step of simplified fluid interaction problem

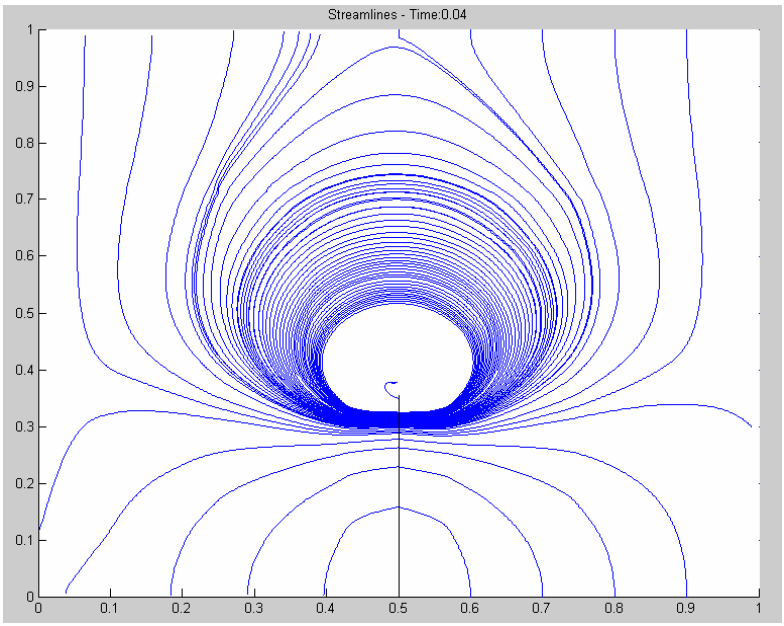

Figure 72: Particle Streamlines for first time step of simplified fluid interaction problem

The results from ANSYS 9.0 first time step are shown in Figures 73 and 74. Figure 73 shows the velocity vector field, Figure 74 shows the pressure contours.

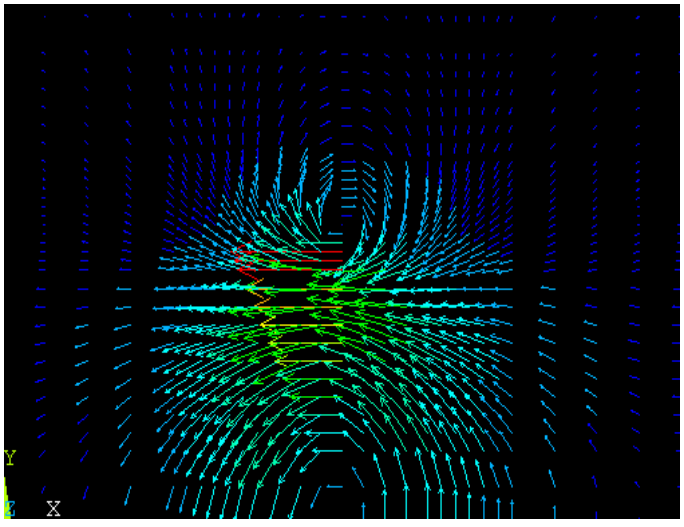

Figure 73: ANSYS 9.0 velocity vectors for first time step of simplified fluid interaction y-position: {0:0.65}, x-position {0:1}

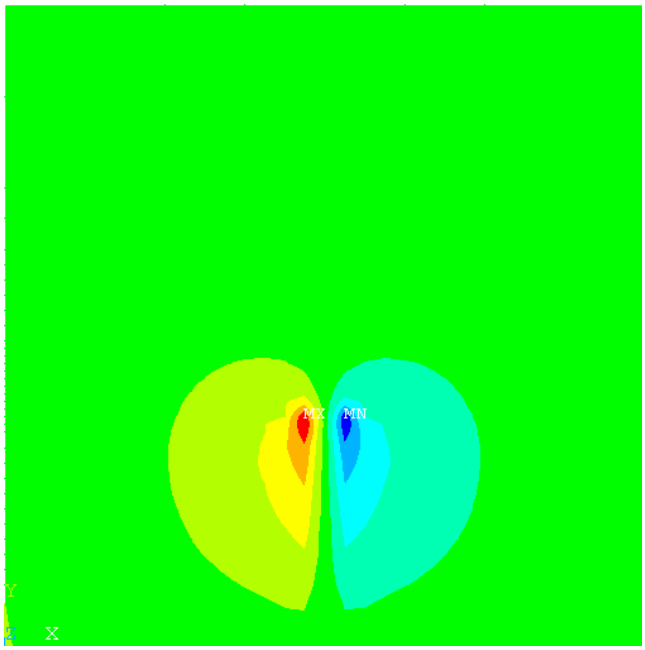

Figure 74: ANSYS 9.0 pressure contours for first time step of simplified fluid interaction problem

There is good agreement between the MATLAB simulation code and ANSYS 9.0 for the first time step of the simplified fluid interaction program.

10.5 MATLAB Simulation Transient Results

The evolution of the pressure and velocity profiles of the surrounding water due to the oscillating rigid beam at different frequencies is investigated using the developed program. The assumptions, problem definition, mesh and solution scheme are all presented before. The first set of simplified fluid interaction results uses an excitation frequency of approximately 1 Hz (0.9 Hz); the same frequency that was observed for the experimental results. An excitation frequency of 0.9 Hz requires that the time step be set to 0.04 seconds. The results are shown below for specific time steps {0.08, 0.32, 0.76, 1.4, 2.4} seconds in Figures 75 – 79. Each plot shows the pressure contour lines overlaid by the particle streamlines. The particle streamlines start at every 0.25 interval in the y-direction crossed with every 0.1 interval in the x-direction.

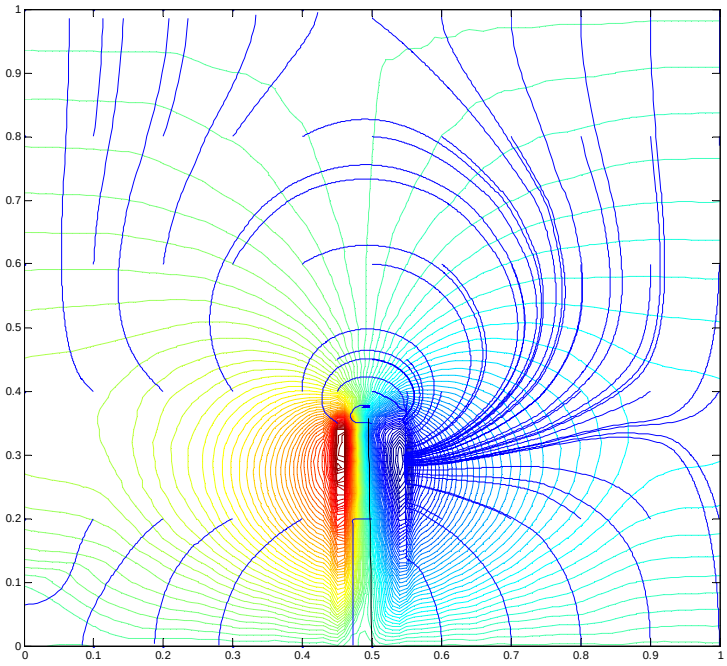

Figure 75: 0.08 seconds for Simplified Fluid Interaction

Figure 75 shows the 2nd time step (0.08 sec) with the beam moving left. Note the tip vortex that occurs at the tip of the beam nodal location. Also note that there is high pressure in front of the beam's movement and low pressure behind its movement. The fluid is rotating in a clockwise fashion on the top of the beam and on the lower front side (left) of the beam the fluid is being push out of the frame, while on the lower back side (right) of the beam the fluid is being pulled into the frame.

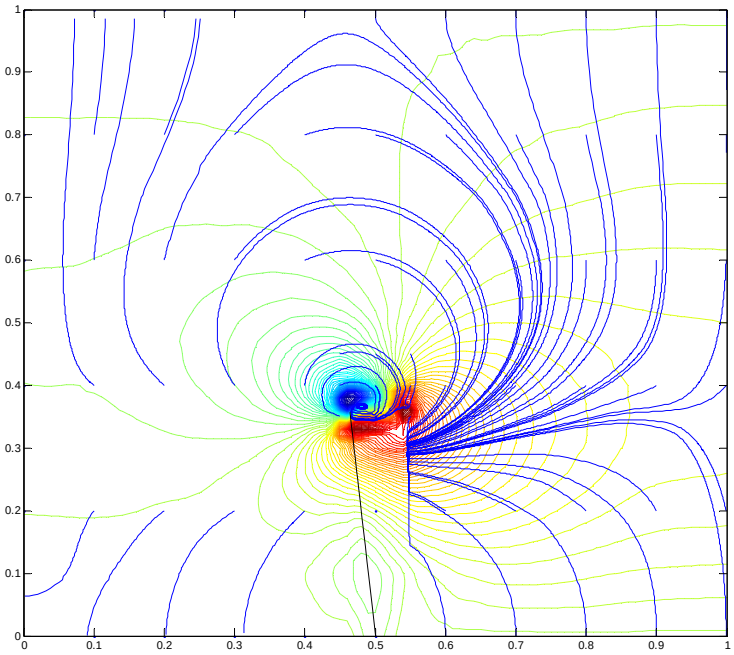

Figure 76: 0.32 seconds for Simplified Fluid Interaction

Figure 76 shows the 8th time step (0.32 sec) where the beam is considered at its maximum left position, or stationary with respect to the beam's nodal velocities. Note that the high pressure switched to the right hand side because the inertia of the moving water coupled with the now-stationary beam location, compresses the water on the right hand side. A very visible vortex is at the tip of the beam due to increased fluid rotation creation over the last seven time steps at the tip of the beam and the now stationary beam. Again the fluid is moving out of the frame in the lower left, the fluid is rotating clockwise over the beam and the fluid is coming into the frame from the lower right hand side.

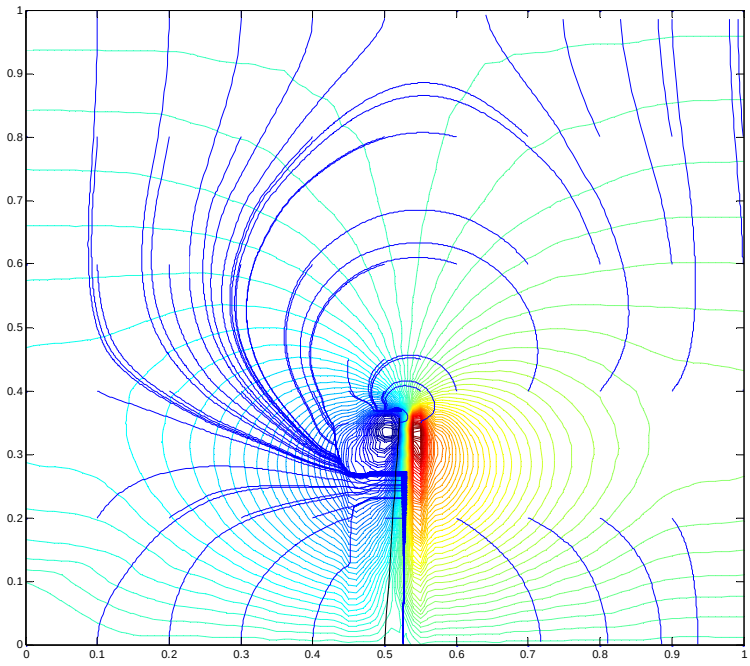

Figure 77: 0.76 seconds for Simplified Fluid Interaction

Figure 77 shows the 19th time step (0.76 seconds) where the beam is moving right. It shows the high pressure in front of the beam as well as the low pressure behind the beam. It is easily seen that the fluid now has a counterclockwise motion over the beam, the fluid is moving into the frame from the lower back side (left) of the beam and it is moving out of the frame on the lower front side (right) of the beam.

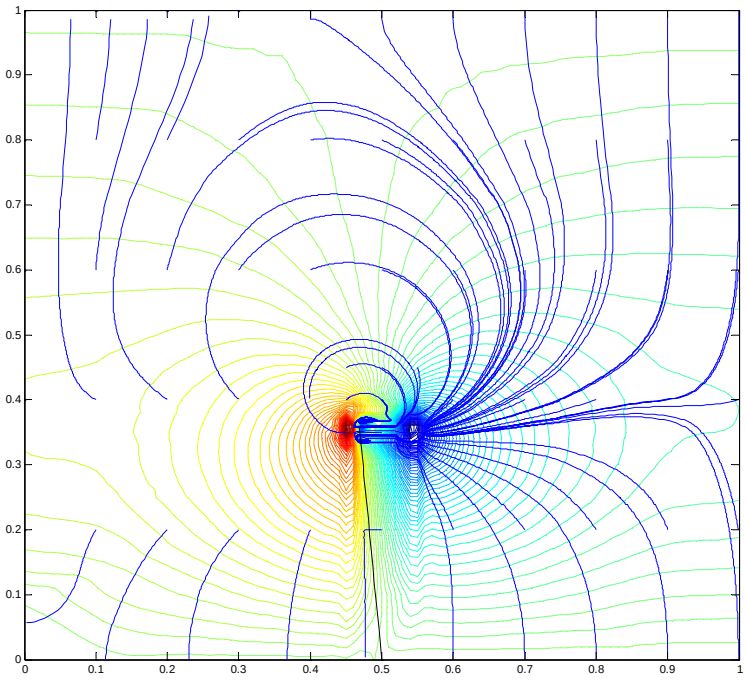

Figure 78: 1.4 seconds for Simplified Fluid Interaction

Figure 78 shows the 35th time step (1.4 seconds) where the beam is moving left. It again shows the high pressure on the front of the beam and the low pressure on the back of the beam. A clearly defined vortex is behind the beam rotating clockwise along with the fluid above the beam. The tip of the beam also creates a small vortex rotating clockwise. The fluid is moving out of the frame in the lower front (left) of the beam and moving into the frame from the lower back side (right) of the beam.

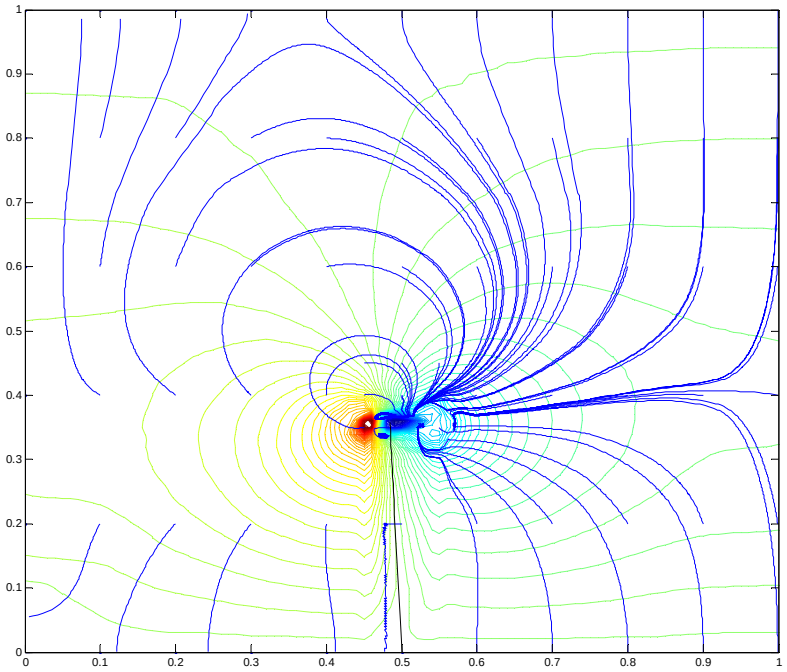

Figure 79: 2.4 seconds for Simplified Fluid Interaction

Figure 79 shows the 60th time step (2.4 seconds) where the beam is moving left. It shows that the same scenario is present as the 35th time step but the pressure locations are more concentrated over time.

The plots of the pressure and particle streamlines continue in this nature and show that there is flow into the frame from (y=0) alternatively from one side of the beam to the other as the cycles progress. There is not a point where there is flow in the positive y-direction on both sides of the beam, which would indicate a forward propulsive force. It is also true that the pressures alternate sides in the same respect. There are points in the results where small vortices are present outside the normal high and low pressure next to the beam, however they tend to dissipate quickly and do not keep the fluid rotating and pulling so that a forward propulsion thrust can be attained. No reverse Kármán vortex pattern was observed at all.

Observations of higher frequencies such as 1.8, 3.6, 7.0, 17.4, 35.5 Hz were also obtained. It is shown that at higher frequencies there is no propulsive advantage, meaning positive y-direction flow on both sides of the beam. The higher frequency plots mimicked

the 0.9 Hz plots (above), where the pressure alternates from one side to the other as the beam moves left and right. This observation shows that a small angle, such as the six degree, is not able to produce a forward motion with this type of setup for different frequencies.

11 Conclusion and Discussion

Experimental as well as analytical investigations of the newly conceived marine propulsion mechanism were conducted. The simple propulsor is made of a piezoelectric actuated composite laminate beam immersed in water. The beam is excited at resonance to provide small displacement oscillations. The analytical investigation is conducted using the Galerkin finite element analysis technique with the oscillating beam simulated as a moving rigid line. Both experimental and analytical results indicate that the simple setup is incapable of generating a forward propulsion motion.

The developed fluid finite element program is applied to solve some 'standard' problems of fluid analysis (Stokes Flow, Cavity Flow, Plane Jet). The results agreed very well with analytical, published and/or ANSYS 9.0 results.

Also, numerical results of the oscillatory beam setup, the simplified fluid interaction problem, gives reasonable velocity and pressure results over time. The results of the first time step agree well with the corresponding results in ANSYS 9.0. The developed rigorous and intensive numerical analysis indicates the fluid finite element program is robust and accurate.

However it should be pointed out that because of the complexity of the fluid structure interaction nature of the problem, many assumptions had to be introduced which limited application capability of the program. These assumptions are:

1) The assumption that there is no-slip on the nodal locations of the beam, between the water and the beam. In reality the fluid particles slip over the surface of the beam and therefore a 'slippery' boundary condition would give a more realistic result.

2) Though a modest adaptive mesh scheme was adopted in the program, more flexible and accurate results would be obtained using a mesh-regeneration technique. This

technique would have the ability to collapse elements and regenerate elements in the vicinity of the beam, when needed.

3) A rather course mesh and time step were adopted because of the storage and computational effort of the available computers and software. A finer mesh together with a smaller time step would produce better results.

These limiting assumptions leave room for improvement. However the initial testing of the fluid interaction problem shows conforming results to ANSYS 9.0 and to expected trends. These positive results in conjunction with overcoming many fluid structure interaction issues and modeling the experimental results aid in the progression to a full finite element piezoelectric actuated model of the marine propulsion fin.

12 Future Work

As mentioned in the conclusion, an experimental setup was established and is readily available for the cantilevered composite plate marine propulsion fin. Also a robust and accurate analytical fluid finite element program was developed for simulating simplified marine propulsion, via a rigid beam oscillation in a fluid medium.

Future work investigation into three main areas is recommended to improve the analytical simulation of the marine propulsion fin:

1) Implementation of full fluid-structure interaction. That is, develop analysis that combines the beam and fluid analysis into one program completely. This full fluid-structure interaction program should include a deformed composite beam analytical model, rather than the rigid beam in the current analysis. Also large deformation non-linear analysis of the beam would give a more realistic result.

2) Implement a deformed mesh with collapsible and regenerative elements in the vicinity of the beam.

3) Extend the analysis to a three-dimensional simulation with plates [Appendix A] immersed in a three-dimensional fluid medium.

For experimental future work it is recommended that a larger water tank is used and a segmented beam (fin) with appropriately distributed piezoelectrics, is constructed to achieve a larger and more flexible deformation. This will increase the ability to mimic biologically inspired undullatory, with oscillatory, marine fin propulsion.

The future work outlined here should be considered because this type of underwater propulsion has the potential to be a very efficient, effective, lightweight, noiseless, generate a small wake, be neutrally buoyant and fast.

REFERENCES

Allen, J. J., and A. J. Smits. "Energy Harvesting Eel." Journal of Fluids and Structures 15 (2001).

Anderson, J. M., et al. "Oscillating foils of high propulsive efficiency." Journal of Fluid Mechanics 360 (1998): 41-72.

Ayers, J., C. Wilbur, and C. Olcott. "Lamprey Robots." . Proceedings of the International Symposium on Aqua Biomechanisms. Ed. T. Wu and N. Kato. N.p.: Tokai University, 2000.

Babuška, I. "Approximation by Hill Functions." Comment Math Univ. Carolinae 11 (1970): 787-811.

- - -. "The Finite Element Method for Elliptic Equations." Numerical Solution of Partial Differential Equations II. Ed. B. Hubbard. London: Academic Press, 1971. 69-106.

Balakrishnan, Sivakumar, and Christopher Niezrecki. "Investigation of THUNDER Actuators as Underwater Propulsors." Journal of Intelligent Material Systems and Structures 13 (Apr. 2002): 193-207.

Bandyopadhyay, Promode R., and Marin J. Donnelly. "The Swimming Hydrodynamics of a Pair of Flapping Foils Attached to a Rigid Body." High Speed Body Motion in Water. AGARD FDP Workshop. Kiev, Ukraine: n.p., 1997. 1-1 - 1-17.

Barmac, T. "Validation of High Displacement Piezoelectric Actuator Finite Element Models." Proceedings of the SPIE 5th European Conference on Smart Structures and Materials. Vol. 4073. Glasgow, UK: n.p., 2000. 37-45.

Blake, R. W. "Influence of pectorial fin shape on thrust and drag in labriform locomotion." Journal of Zoology (London) (1981).

- - -. "On ostraciiform locomotion." Journal of Marine Biology 57 (1977): 1047-1055.

Breder, C. M. "The locomotion of fishes." Zoological (New York) 4 (1926): 159-297.

Brezzi, F. "On the existence, uniqueness and approximation of saddle point problems arising from Lagrangian multipliers." Anal. Num. 8 (1974): 129-151.

Bristeau, M. O., R. Glowinski, and J. Periaux. "Numerical Methods for the Navier-Stokes Equations." Computer Physics Reports 6 (1987): 73-187.

Brooks, A. N., and T.J.R. Hughes. “Streamline upwind/Petrov-Galerkin formulations for convection dominated flows with particular emphasis on the incompressible Navier-Stokes equation.” Comput. Methods Appl. Mech. Engrg. 32 (1982): 199-259.

Cappozzoli, M., et al. “Modeling Aspects Concerning THUNDER Actuators.” Proceedings of the SPIE - The International Society of Optical Engineering. Vol. 3667. N.p.: n.p., 1999. 719-727.

Donea, J., et al. “Finite Element Solution of the Unsteady Navier-Stokes Equations by a Fractional Step Method.” Computer Methods in Applied Mechanics and Engineering 30 (1982): 53-73.

Donea, J., and A. Huerta. Finite Element Methods for Flow Problems. Chichester: John Wiley and Sons, 2003.

Drucker, Eliot G., and George V. Lauder. “Locomotor function of the dorsal fin in teleost fishes: experimental analysis of wake forces in sunfish.” Journal of Experimental Biology 204 (2001): 2943-2958.

Elias, R. N., A.L.G.A. Coutinho, and M.A.D. Martins. “Inexact Newton-type methods for the solution of steady incompressible viscoplastic flows with the SUPG/PSPG finite element formulation.” Computer Methods in Applied Mechanics and Engineering 195 (2006): 3145-3167.

Face International Corp. THUNDER. 2002. Apr. 2006 <http://www.faceco.com>.

Face International Corp. THUNDER. 2001. Apr. 2006 <http://www.faceco.com>.

Fukuda, Toshio, et al. “Steering Mechanism of Underwater Micro Mobile Robot.” IEEE International Conference on Robotics and Automation (1995): 363-368.

Goldfarb, Michael. “Utilization of Elastodynamic Locomotion in Mesoscale Robotic Insects.” Center for Intelligent Mechatronics: Vanderbilt University (2000).

Guermond, J. -L., and L. Quartapelle. “On stability and convergence of projection methods based on pressure Poisson equation.” International Journal of Numerical Methods in Fluids 26.9 (1998): 1039-1053.

- - -. “On the approximation of the unsteady Navier-Stokes equations by finite element projection methods.” Numer. Math. 80.5 (1998): 207-238.

Hover, F. S., O. Haugsdal, and M. S. Triantafyllou. “Effect of angle of attack profiles in flapping foil propulsion.” J. Fluid. Struct. 19.1 (Jan. 2004): 37-47.

Hughes, T.J.R., and A. N. Brooks. “A multi-dimensional upwind scheme with no crosswind diffusion.” Finite Element Methods for Convection Dominated Flows. Ed. T.J.R. Hughes. Vol. 34. New York: ASME, 1979. 19-35.

Janocha, Harmot. Adaptronics and Smart Structures. Berlin; New York: Springer, 1999.

Jung, Jaehoon, et al. “Tadpole Robot (TadRob) using ionic polymer metal composite (IPMC) actuator.” Proceedings of SPIE. Smart Structures and Materials 2003: Electroactive Polymer Actuators and Devices (EAPAD). Ed. Yoseph Bar-Cohen. Vol. 5051. N.p.: n.p., 2003. 272-280.

Katz, J., and D. Weihs. “Large amplitude unsteady motion of a flexible slender propulsor.” Journal of Fluid Mechanics 89 (1979): 713-723.

Kelly, D. W., et al. “A note on upwinding and anisotropic balancing dissipation in finite element approximations to convective diffusion problems.” International Journal of Numerical Methods in Engineering 15 (1980): 1705-1711.

Kerrebrock, Peter A, Jamie M. Anderson, and Joel Parry. “Application Requirements of Artificial Muscles for Swimming Robots.” Smart Structures an Materials 4329 (2001): 364-374.

Ladyzhenskaya, O. A. The mathematical theory of viscous incompressible flow. New York: Gordon and Breach, 1969.

Lauder, George V., and Eliot G. Drucker. “Morphology and Experimental Hydrodynamics of Fish Fin Control Surfaces.” IEEE Journal of Oceanic Engineerin 29.3 (July 2004): 556-569.

Laurent, Guillaume, and Emmanuel Piat. “Efficiency of Swimming Microrobots using Ionic Polymer Metal Composite Actuators.” _. Proceedings of the 2001 IEEE International Conference on Robotics and Automation. Seoul, Korea: n.p., 2001. 3914-3919.

Laval, H., and L. Quartapelle. “A Fractional-Step Taylor-Galerkin Method for Unsteady Incompressible Flows.” International Journal for Numerical Methods in Fluids 11 (1990): 501-513.

Lighthill, M. J. “Aquatic animal propulsion of high hydrodynamic efficiency.” Journal of Fluid Mechanics 44 (1970): 263-301.

- - -. “Hydromechanics of aquatic animal propulsion.” Ann. Rev. Fluid. Mech. 1 (1969): 413-466.

Lighthill, M J. “Note on the swimming of slender fish.” Journal of Fluid Mechanics 9 (1960): 305-317.

Lindsey, C. C. “Form, function and locomotory habits in fish.” Fish Physiology Vol. VII Locomotion. By W. S. Hoar and D. J. Randall. Academic. New York: n.p., 1978. 1-100.

Liu, H., and K Kawachi. “A numerical study of undullatory swimming.” J. Comput. Phys. 155 (1999): 223-247.

Miniature Swimming Vehicles. Intelligent Structures and Systems Laboratory , 2001. May 2006 <http://www.mecheng.ohio-state.edu/~gnwashin/parts/swim.html>.

Mojarrad, Mehran. “Characterization of light-weight electroactive polyelectrolyte Composite Artificial Muscles (CAM) as biomimetric propulsion fins for remote-controlled aquatic vehicles.” Proceedings of SPIE . Smart Structures and Materials 2000: Electroactive Polymer Actuators and Devices (EAPAD). Ed. Yoseph Bar-Cohen. Vol. 3987. N.p.: n.p., 2000. 344-350.

Mojarrad, Mehran, and Mohsen Shahinpoor. “Biomimetric Robotic Propulsion Using Polymeric Artificial Muscles.” . Proceedings of the 1997 IEEE International Conference on Robotics and Automation. Albuquerque, New Mexico: n.p., 1997. 2152-2157.

Mulling, J., et al. “LoadCharacterization of High Displacement Piezoelectric Actuators with Various End Conditions.” Materials Research Center, North Carolina State University, Raleigh, NC (2000): 27695-7919.

Murray, M. M., and L. E. Howle. “Spring stiffness influence on an oscillating propulsor.” Journal of Fluids and Structures 17 (2003): 915-926.

Niezrecki, C., and H. H. Cudney. “Improving Power Consumption Characteristics of Piezoelectric Actuators.” Journal of Intelligent Material Systems and Structures 5.4 (1994): 522-529.

Olson, Mervyn D., and Shih-Yu Tuann. “New Finite Element Results for the Square Cavity.” Computers and Fluids 7 (1979): 123-135.

Ono, Nagato, et al. “Design of fish fin actuators using shape memory alloy composites.” Proceedings of SPIE. Smart Structures and Materials 2004: Industrial and Commercial Applications of Smart Structures Technologies. Ed. Eric H. Anderson. Vol. 5388. Bellingham, WA: n.p., n.d. 305-312.

“Penguin Boat.” MIT Briefing Book, MIT Research Support, DoD Recent MIT Campus Projects 1997: 2-4.

Quarteroni, A., F. Saleri, and A. Veneziani. “Factorization methods for the numerical approximation of Navier-Stokes equations.” Comput. Methods Appl. Mech. 188 (2000): 505-526.

Rabinovitch, Oded, and Jack Vinson. “Smart Fins: Analytical Modeling and Basic Design Concepts.” Mechanics of Advanced Materials and Structures 10 (2003): 249-267.

Reddy, J. N. An Introduction to the Finite Element Method. 3rd ed. New York: McGraw-Hill Companies, Inc., 2006.

Rediniotis, O. K., et al. “Development of a Shape-Memory-Alloy Actuated Biomimetric Hydrofoil.” Journal of Intelligent Material Systems and Structures 13 (Jan. 2002): 35-49.

Root, R. G., and J. H. Long Jr. “A virtual swimming fish: modeling carangiform fish locomotion using elastic plate theory.” _. 10th Int’l. Symp. Unmanned Untethered Submersible Technology (UUST), Procs. Spec. Session Bio-Engineering. N.p.: n.p., 1997. Supplement 1-7.

Rosen, M. W. “Water flow about a swimming fish.” US Naval Ordnance Test Station, China Lake, CA TP 2298 (1959): 96.

Stakiotakis, Michael, David M Lane, and J. Bruce C Davies. “Review of Fish Swimming Modes for Aquatic Locomotion.” IEEE Journal of Oceanic Engineering 24.2 (Apr. 1999): 237-252.

Streitlien, K., and G. S. Triantafyllou. “On Thrust Estimates for Flapping Foils.” Journal of Fluids and Structures 12 (1998): 47-55.

Taleghani, B. K., and J. F. Campbell. “Non-Linear Finite Element Modeling of THUNDER Piezoelectric Actuators.” Proceedings of the SPIE Conference on Smart Structures and Materials. Smart Structures and Intelligent Systems . Vol. 3668. Newport Beach, CA: n.p., 1999. 555-566.

Tezduyar, T. E., et al. “Incompressible flow computations with stabilized bilinear and linear equal-order-interpolation velocity-pressure elements.” Computer Methods in Applied Mechanics and Engineering 95 (1992): 221-242.

Tezduyar, Tayfun E. “Finite elements in fluids: Stabilized formulations and moving boundaries and interfaces.” Computers and Fluids (2005): In Press.

Tezduyar, Tayfun E., and Yasuo Osawa. “Finite element stabilization parameters computed from element matrices and vectors.” Computer Methods in Applied Mechanics and Engineering 190 (2000): 411-430.

THUNDER TH-7R. Face International Corporation, 2006. Apr. 2006 <http://www.faceco.com>.

Triantafyllou, G. S., M. S. Triantafyllou, and M. A. Grosenbaugh. “Optimal Thrust Development in Oscillating Foils with Application to Fish Propulsion.” Journal of Fluids and Structures 7 (1993): 205-224.

Von Kármán, T., and J. M. Burgess. “General aerodynamic theory - perfect fluids.” Aerodynamic Theory (ed. W. F. Durand) Berlin: Springer 2 (1935).

Wu, T. Y. “Swimming of a waving plate.” Journal of Fluid Mechanics 10 (1961): 321-344.

APPENDIX A: CPT, Laminated piezoelectric-plate Theory and Analysis

Preface

Classical plate theory will be used to model the three-dimensional marine propulsion device so that the analysis will be available when it is possible to move to three-dimensions. The limiting factor at this time is the finite element code for three dimensional fluids because this thesis is mainly concerned with two-dimensional modeling and comparison. Natural vibration results, for small deflections, will be obtained from this section and compared to ANSYS 9.0 results.

A.1 Basic Equations, Governing Equations and FE Formulation

Classical plate theory, dealing with relatively small deformations, assumes that a straight line perpendicular to the thickness plane of the plate is inextensible, remains straight and rotates so that it remains perpendicular to the tangent of the deformed surface. The reason for abiding by these assumptions is that if internal membrane stresses develop within the material, the resulting governing equation is nonlinear. Therefore due to the fact that the deformation is relatively small compared to the marine propulsion fin, the assumption is adequate and the equation simplifies to a linear governing equation and the computation is reduced drastically. Figure 75 shows the local coordinate system for a plate element.

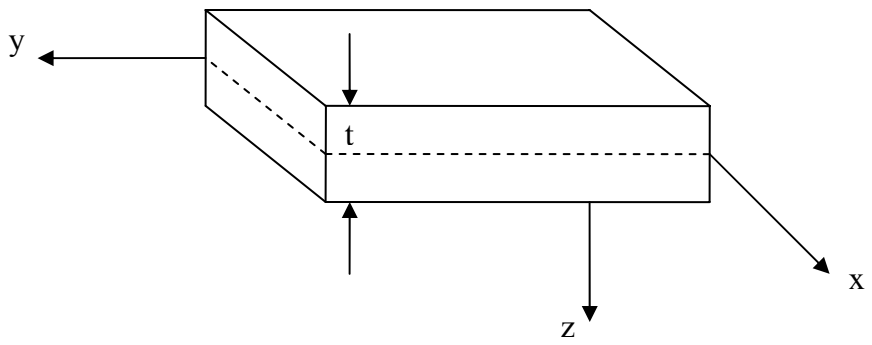

Figure 80: The local Cartesian coordinate system for a plate element

The strain-displacement relationship for the classical plate theory is:

$$\begin{Bmatrix} \varepsilon_x \\ \varepsilon_y \\ \gamma_{xy} \end{Bmatrix} = \begin{Bmatrix} \frac{\partial u_0}{\partial x} + z\kappa_x \\ \frac{\partial v_0}{\partial x} + z\kappa_y \\ \frac{\partial v_0}{\partial x} + \frac{\partial u_0}{\partial y} + z\kappa_{xy} \end{Bmatrix} = \begin{Bmatrix} \frac{\partial u_0}{\partial x} - z\frac{\partial \theta_x}{\partial x} \\ \frac{\partial v_0}{\partial x} - z\frac{\partial \theta_y}{\partial y} \\ \frac{\partial v_0}{\partial x} + \frac{\partial u_0}{\partial y} - z\left(\frac{\partial^2 w}{\partial x \partial y} + \frac{\partial^2 w}{\partial x \partial y}\right) \end{Bmatrix} = \begin{Bmatrix} \frac{\partial u_0}{\partial x} - z\frac{\partial^2 w}{\partial x^2} \\ \frac{\partial v_0}{\partial x} - z\frac{\partial^2 w}{\partial y^2} \\ \frac{\partial v_0}{\partial x} + \frac{\partial u_0}{\partial y} - 2z\frac{\partial^2 w}{\partial x \partial y} \end{Bmatrix}, \tag{A.1}$$

where κ is the curvature.

Figure 76 shows the x-z plane strain-displacement relationship:

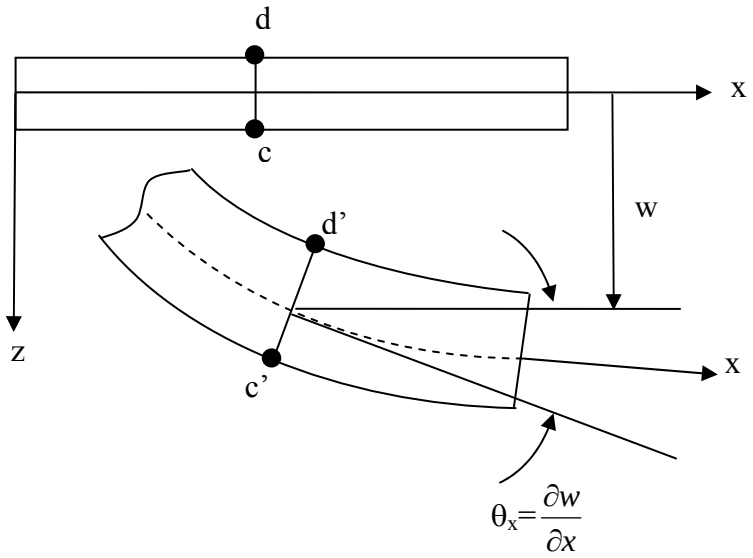

Figure 81: Illustrating the strain-displacement relationship in the x-z plane

Using the stress-strain relationship for plane stress analysis, the resulting matrix in Cartesian coordinates is:

$$\begin{Bmatrix} \sigma_x \\ \sigma_y \\ \sigma_{xy} \end{Bmatrix} = \begin{bmatrix} \frac{E_x}{1-\nu_{xy}\nu_{yx}} & \frac{\nu_{xy}E_y}{1-\nu_{xy}\nu_{yx}} & 0 \\ \frac{\nu_{yx}E_y}{1-\nu_{xy}\nu_{yx}} & \frac{E_y}{1-\nu_{xy}\nu_{yx}} & 0 \\ 0 & 0 & G_{xy} \end{bmatrix} \begin{Bmatrix} \varepsilon_x \\ \varepsilon_y \\ \varepsilon_{xy} \end{Bmatrix}, \tag{A.2}$$

where σ denotes the stresses, E is the modulus of elasticity, G is the modulus of rigidity, ν denotes poisson's ratio and ε denotes the strains.

The moments created on each faces of the plate element are related to the stress by:

$$M_{ij} = \int_{-t/2}^{t/2} z\sigma_{ij}\, dz, \tag{A.3}$$

where M denotes the moments and z represents the distance from the mid-plane.

Summing the forces in the z-direction reveals the equation:

$$\frac{\partial V_x}{\partial x} + \frac{\partial V_y}{\partial y} + q(x,y) = \rho A \ddot{w}, \tag{A.4}$$

where V denotes the shear stresses, q is the applied pressure over the surface, ρ is the density, and $\ddot{w}$ is the acceleration in the z-direction.

Summing the moments in the x and y directions respectively reveals:

$$V_y = \frac{\partial M_{xy}}{\partial x} + \frac{\partial M_y}{\partial y}, \tag{A.5}$$

$$V_x = \frac{\partial M_{xy}}{\partial y} + \frac{\partial M_x}{\partial x}, \tag{A.6}$$

Substituting Equations A.5 and A.6 into Equation A.4, using the moment-stress relationship defined in Equation A.3, including the dynamic terms and integrating over the thickness gives the governing equation for the classical plate theory.

$$\frac{\partial^2}{\partial x^2}\left(D_{11}\frac{\partial^2 w}{\partial x^2} + D_{12}\frac{\partial^2 w}{\partial y^2}\right) + \frac{\partial^2}{\partial y^2}\left(D_{12}\frac{\partial^2 w}{\partial x^2} + D_{22}\frac{\partial^2 w}{\partial y^2}\right) + 2\frac{\partial^2}{\partial x \partial y}\left(D_{66}\frac{\partial^2 w}{\partial x \partial y}\right) - q + I_0\frac{\partial^2 w}{\partial t^2} = 0, \tag{A.7}$$

where the coefficients defined above are defined as:

$$D_{11} = \frac{E_x t^3}{12\left(1-\nu_{xy}\nu_{yx}\right)}, \quad D_{12} = \frac{\nu_{xy} E_y t^3}{12\left(1-\nu_{xy}\nu_{yx}\right)},$$

$$D_{22} = \frac{E_y t^3}{12\left(1-\nu_{xy}\nu_{yx}\right)}, \quad D_{66} = \frac{1}{12} G_{xy} t^3,$$

$$I_0 = \int_{-t/2}^{t/2} \rho \, dz = \rho t, \tag{A.8}$$

Therefore the weak form of the governing equation for classical plate theory is:

$$\int_{\Omega_e}\left[\frac{\partial^2\Psi_i}{\partial x^2}\left(D_{11}\frac{\partial^2 w}{\partial x^2}+D_{12}\frac{\partial^2 w}{\partial y^2}\right)+\frac{\partial^2\Psi_i}{\partial y^2}\left(D_{12}\frac{\partial^2 w}{\partial x^2}+D_{22}\frac{\partial^2 w}{\partial y^2}\right)+4D_{66}\frac{\partial^2\Psi_i}{\partial x\partial y}\frac{\partial^2 w}{\partial x\partial y}\right]dxdy$$
$$+\int_{\Omega_e}\left[-\Psi_i q+\Psi_i I_0\frac{\partial^2 w}{\partial t^2}\right]dxdy$$
$$-\int_{\Gamma_e}\left[\Psi_i\left(\frac{\partial M_x}{\partial x}+\frac{\partial M_{xy}}{\partial y}\right)n_x+\Psi_i\left(\frac{\partial M_{xy}}{\partial x}+\frac{\partial M_y}{\partial y}\right)n_y\right]ds$$
$$+\int_{\Gamma_e}\left[\frac{\partial\Psi_i}{\partial x}\left(M_x n_x+M_{xy}n_y\right)+\frac{\partial\Psi_i}{\partial y}\left(M_{xy}n_x+M_y n_y\right)\right]ds=0, \qquad \text{(A.9)}$$

where n_x and n_y are the direction cosines of the applied moment or force in the directions of the x and y axis.

To begin the finite element formulation interpolation functions must be formed. In this analysis a four node rectangular element is chosen. The interpolation functions used are formed from Pascal's triangle. Due to the fact that the displacements as well as the slopes in both x and y directions for each node need to be approximated, there are twelve variables that need to be included. Using the first four tiers of Pascal's triangle and the two "middle" terms of the fifth tier, to create symmetry, this is accomplished. Figure 82 shows the degree of freedom of each node on the element.

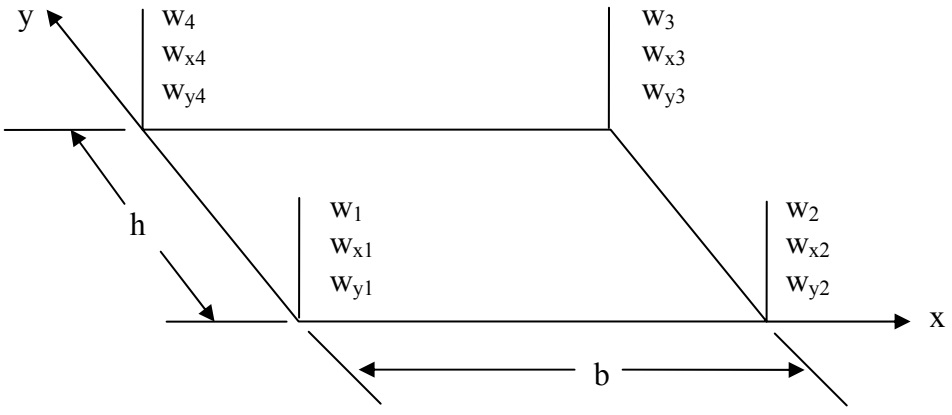

Figure 82: Degrees of freedom on each node

This formulation of the interpolation functions results with the following equations for the interpolation functions:

$$
\begin{aligned}
\Psi_1^e &= 1-\frac{3}{4}x^2-\frac{1}{4}xy-\frac{3}{4}y^2+\frac{1}{4}x^3+\frac{3}{8}x^2y+\frac{3}{8}xy^2+\frac{1}{4}y^3-\frac{1}{8}x^3y-\frac{1}{8}xy^3,\\
\Psi_2^e &= x-x^2-\frac{1}{2}xy+\frac{1}{4}x^3+\frac{1}{2}x^2y-\frac{1}{8}x^3y,\\
\Psi_3^e &= y-\frac{1}{2}xy-y^2+\frac{1}{2}xy^2+\frac{1}{4}y^3-\frac{1}{8}xy^3,\\
\Psi_4^e &= \frac{3}{4}x^2+\frac{1}{4}xy-\frac{1}{4}x^3-\frac{3}{8}x^2y-\frac{3}{8}xy^2+\frac{1}{8}x^3y+\frac{1}{8}xy^3,\\
\Psi_5^e &= -\frac{1}{2}x^2+\frac{1}{4}x^3+\frac{1}{4}x^2y-\frac{1}{8}x^3y,\\
\Psi_6^e &= \frac{1}{2}xy-\frac{1}{2}xy^2+\frac{1}{8}xy^3,\\
\Psi_7^e &= -\frac{1}{4}xy+\frac{3}{8}x^2y+\frac{3}{8}xy^2-\frac{1}{8}x^3y-\frac{1}{8}xy^3,\\
\Psi_8^e &= -\frac{1}{4}x^2y+\frac{1}{8}x^3y,\\
\Psi_9^e &= -\frac{1}{4}xy^2+\frac{1}{8}xy^3,\\
\Psi_{10}^e &= \frac{1}{4}xy+\frac{3}{4}y^2-\frac{3}{8}x^2y-\frac{3}{8}xy^2-\frac{1}{4}y^3+\frac{1}{8}x^3y+\frac{1}{8}xy^3,\\
\Psi_{11}^e &= \frac{1}{2}xy-\frac{1}{2}x^2y+\frac{1}{8}x^3y,\\
\Psi_{12}^e &= -\frac{1}{2}y^2+\frac{1}{4}xy^2+\frac{1}{4}y^3-\frac{1}{8}xy^3,
\end{aligned}
\tag{A.10}
$$

Figure 83 graphically represents the shape functions.

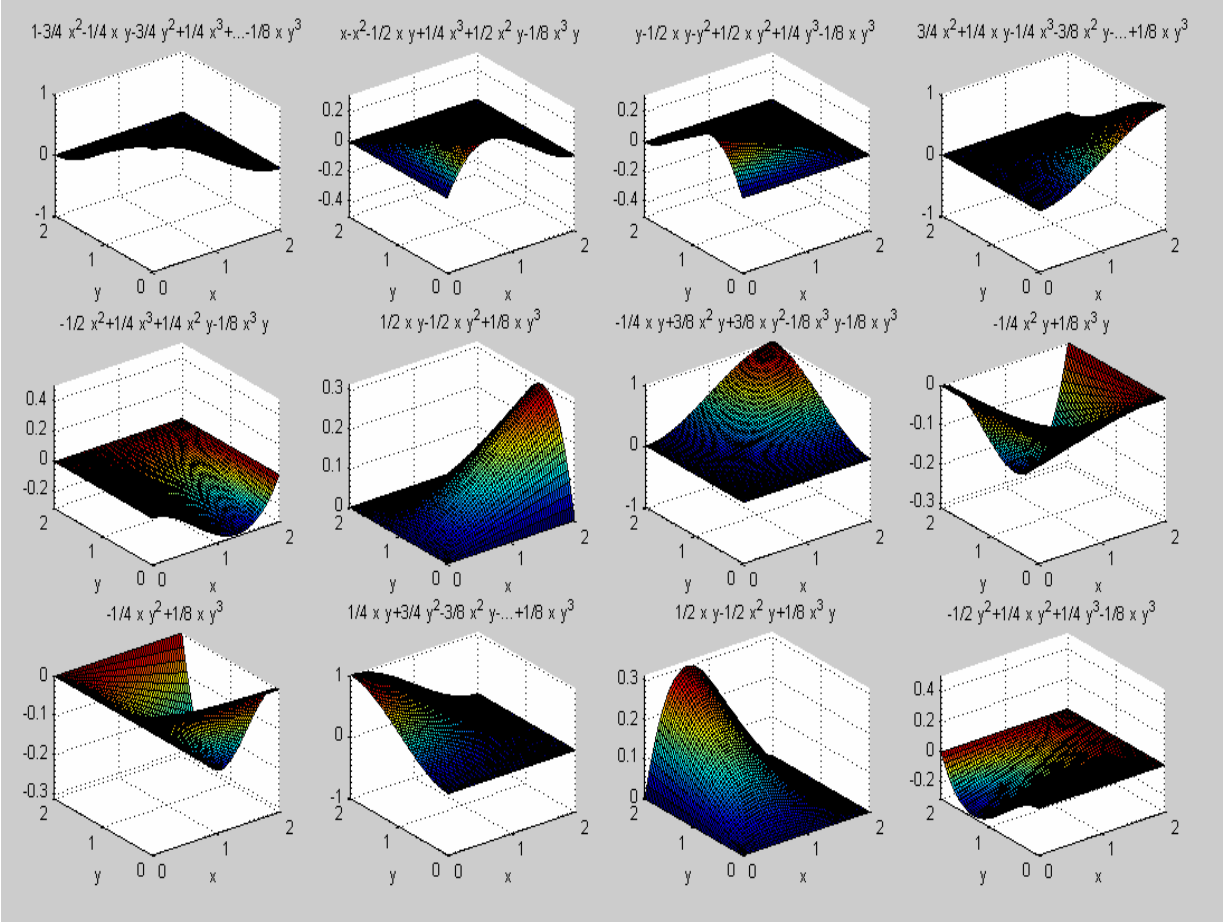

Figure 83: Graphical representation of shape functions over the domain Ω= [0:2,0:2]

Using Galerkin's method for finite element formulation the weak form of the governing equation is integrated by parts twice and the following matrix set of equations are formed. From this point forward the terms involving the third differentiation of the displacement will be neglected because they retain minimal effect on the resulting equation. The finite element form of the classical plate theory is:

$$\left[M_{ij}^{e}\right]\left\{\ddot{w}_{i}^{e}\right\}+\left[K_{ij}^{e}\right]\left\{w_{i}^{e}\right\}=\left\{f_{i}^{e}\right\}+\left\{Q_{i}^{e}\right\}, \tag{A.11}$$

The coefficients defined in A.11, the above matrix, are:

$$K_{ij}^{e} = \int_{\Omega_e} \left[\begin{array}{l} D_{11} \dfrac{\partial^2 \Psi_i}{\partial x^2} \dfrac{\partial^2 \Psi_j}{\partial x^2} + D_{12} \left(\dfrac{\partial^2 \Psi_i}{\partial x^2} \dfrac{\partial^2 \Psi_j}{\partial y^2} + \dfrac{\partial^2 \Psi_i}{\partial y^2} \dfrac{\partial^2 \Psi_j}{\partial x^2} \right) \\ \quad + D_{22} \dfrac{\partial^2 \Psi_i}{\partial y^2} \dfrac{\partial^2 \Psi_j}{\partial y^2} + 4 D_{66} \dfrac{\partial^2 \Psi_i}{\partial x \partial y} \dfrac{\partial^2 \Psi_j}{\partial x \partial y} \end{array} \right] dxdy$$

$$M_{ij}^{e} = \int_{\Omega_e} \left[I_0 \Psi_i \Psi_j + I_2 \left(\frac{\partial \Psi_i}{\partial x} \frac{\partial \Psi_j}{\partial x} + \frac{\partial \Psi_i}{\partial y} \frac{\partial \Psi_j}{\partial y} \right) \right] dxdy$$

$$f_i^{e} = \int_{\Omega_e} [q \Psi_i] dxdy$$

$$Q_i^{e} = \int_{\Gamma_e} \left[\Psi_i \left\{ \left(\frac{\partial M_x}{\partial x} + \frac{\partial M_{xy}}{\partial y} \right) n_x + \left(\frac{\partial M_{xy}}{\partial x} + \frac{\partial M_y}{\partial y} \right) n_y + \frac{\partial}{\partial s} \left[\left(M_y - M_x \right) n_x n_y + M_{xy} \left(n_x^2 - n_y^2 \right) \right] \right\} \right] ds$$

$$- \int_{\Gamma_e} \left[\frac{\partial \Psi_i}{\partial n} \left(M_x n_x^2 + M_y n_y^2 + 2 M_{xy} n_x n_y \right) \right] ds = 0 \qquad \text{(A.12)}$$

A.2 Natural vibration of a plate and comparison of results

Consider the natural vibration of a 1018 cold drawn steel cantilevered isotropic rectangular plate with the following properties:

Modulus of Elasticity = $E_x = E_y = 205\ 10^9$ Pa

Poisson's Ratio = $\nu_{xy} = 0.29$

$\nu_{yx} = \nu_{xy}$

Density = $\rho = 7870$ kg/m^3

Length = 0.5 m

Width = 0.2 m

Thickness = 0.002 m

The plate will be discretized into 15 elements; the length in the x-direction (length) will be 0.1 m and the length in the y-direction (height) will be {0.05, 0.1, 0.05} m.

MATLAB code was created to deal with the computations involved with the plate vibration. The natural vibration calculation follows the form of Equation 7.9. The first six free vibration frequencies are {6.7182, 42.0051, 45.3546, 118.1738, 141.2077, 233.6066} Hz and their plots can be seen in Figure 84.

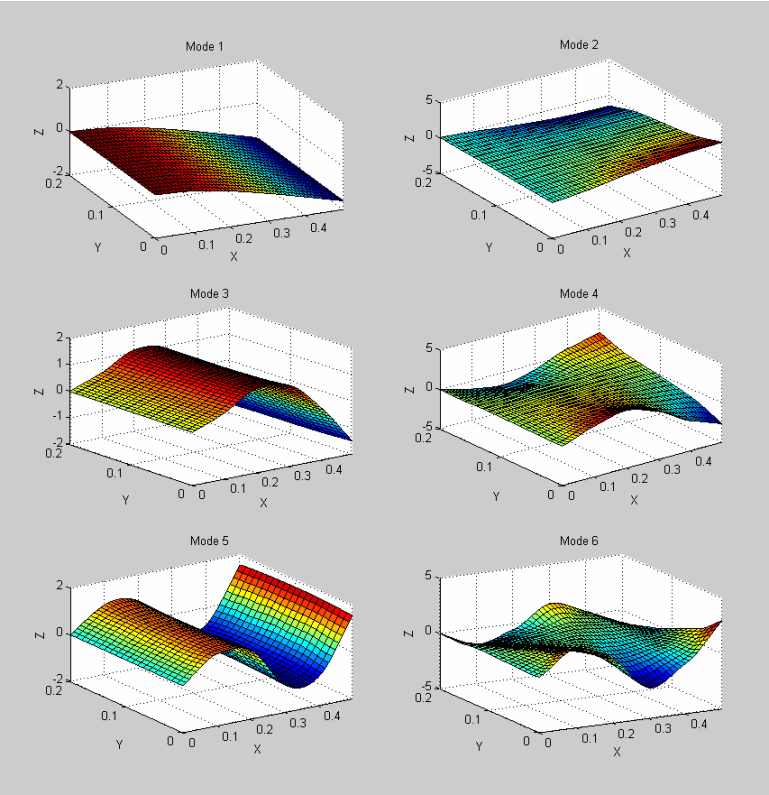

Figure 84: Graphical representations of the first six free vibration frequencies

A.3 ANSYS 9.0 analysis and comparison

The construction technique of the plate in ANSYS 9.0 is exactly the same as the construction of the beam in ANSYS 9.0, except the values for material properties and material sizes are different. Again the 20-node solid 95 was utilized to calculate the following data so that future analysis can utilize the 20-node solid 226 for the piezoelectric model building. Table 5 shows the comparison between the simulated MATLAB code and

the ANSYS 9.0 results and Figure 85 shows the mode shapes for the ANSYS 9.0 free vibration results.

Comparison study 3-D modes of vibration

Plate without piezoelectric elements
15 elements – 0.1 each in length and {0.05, 0.1, 0.05} in width

	f1	f2	f3	f4	f5	f6
Simulated Results:	6.7182	42.0051	45.3546	118.1738	141.2077	233.6066
ANSYS 9.0 Results:	7.016	36.377	45.830	118.847	141.731	231.452

Table 5: Simulation vs. ANSYS 9.0 Results for Plate Modes

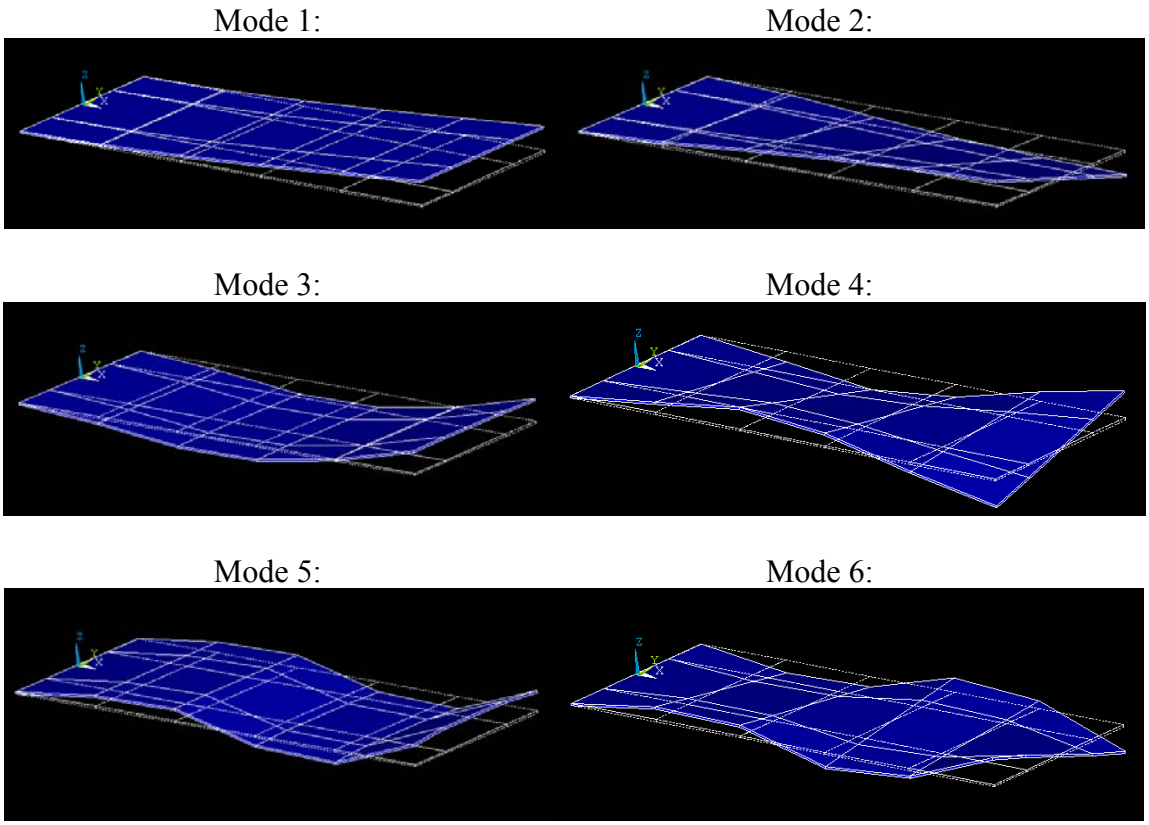

Figure 85: Mode shapes of free vibration from ANSYS 9.0 data

The small difference is due to leaving out the higher order terms and making the simplifying assumptions for classical plate theory. It is obvious, as assumed before, that the difference is quite small.

A.4 Natural and forced vibration of a laminated piezoelectric-plate: ANSYS 9.0 comparison

The laminated piezoelectric-beam theory that was developed in Chapters 8 and 9 can be directly applied to a three-dimensional case as well. Switching to three-dimensions requires that the transverse deflection, represented in Figure 61, be applied to both the x-direction and y-direction because the deformation experienced in x-direction is the same in the y-direction. The moment created by both piezoelectric elements on the top and bottom surfaces of the plate can be mathematically represented by Equation 9.2, just like the beam element. However since there are two nodes on each side of the plate element, the moment experienced on the plate nodes will be divided by two and each resulting moment will be distributed between the two nodes.

Considering a plate that is identical to the one observed in the previous analysis, a laminated piezoelectric-plate element will be added to the cantilevered side of the plate in the middle, shown in Figure 86.

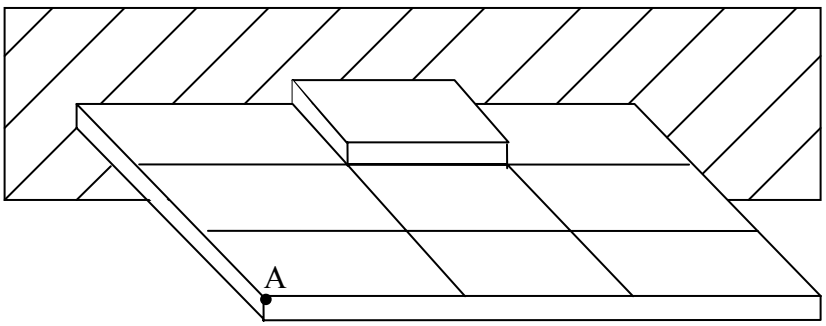

Figure 86: Model of cantilevered plate with laminated piezoelectric-plate element in the middle of the cantilevered side. Note another laminated piezoelectric-plate element is located on the bottom surface as well to complete the element

Free vibration of the laminated piezoelectric-plate was analyzed using Equation 7.9. The results for the natural frequencies are {8.8490, 49.0285, 55.5132, 150.9688, 157.3552,

275.5715} Hz. These results are slightly higher than the results of the free vibration without the laminated piezoelectric-plate element, which is expected. Figure 87 shows the first six modes of free vibration.

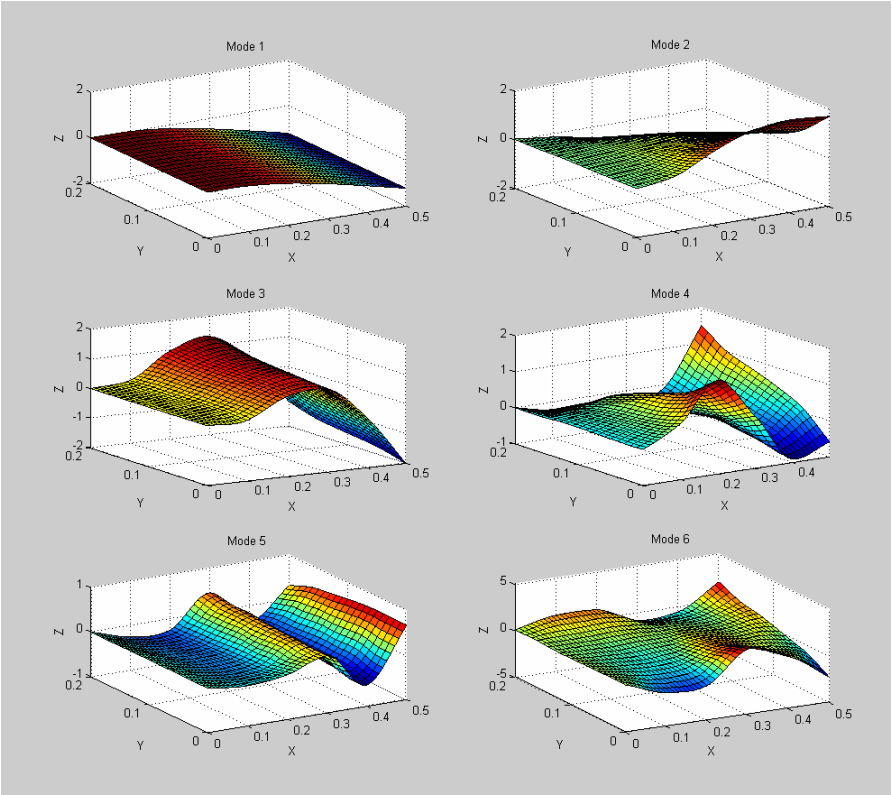

Figure 87: First six modes of vibration for the laminated piezoelectric-plate model

Using the data obtained from the simulated MATLAB code and the results obtained from an ANSYS 9.0 model, a comparison table was created, Table 6. The ANSYS 9.0 modes of vibration are shown in Figure 88.

Comparison study 3-D modes of vibration

Plate with piezoelectric elements
15 elements – 0.1 each in length and {0.05, 0.1, 0.05} in width
Piezoelectric element is implemented on the cantilevered side of the plate in the middle

	f1	f2	f3	f4	f5	f6
Simulated Results:	8.8490	49.0285	55.5132	150.9688	157.3552	275.5715
ANSYS 9.0 Results:	8.431	38.763	51.217	125.262	148.029	241.08

Table 6: Simulation vs. ANSYS 9.0 Results for Laminated Piezoelectric-Plate Modes

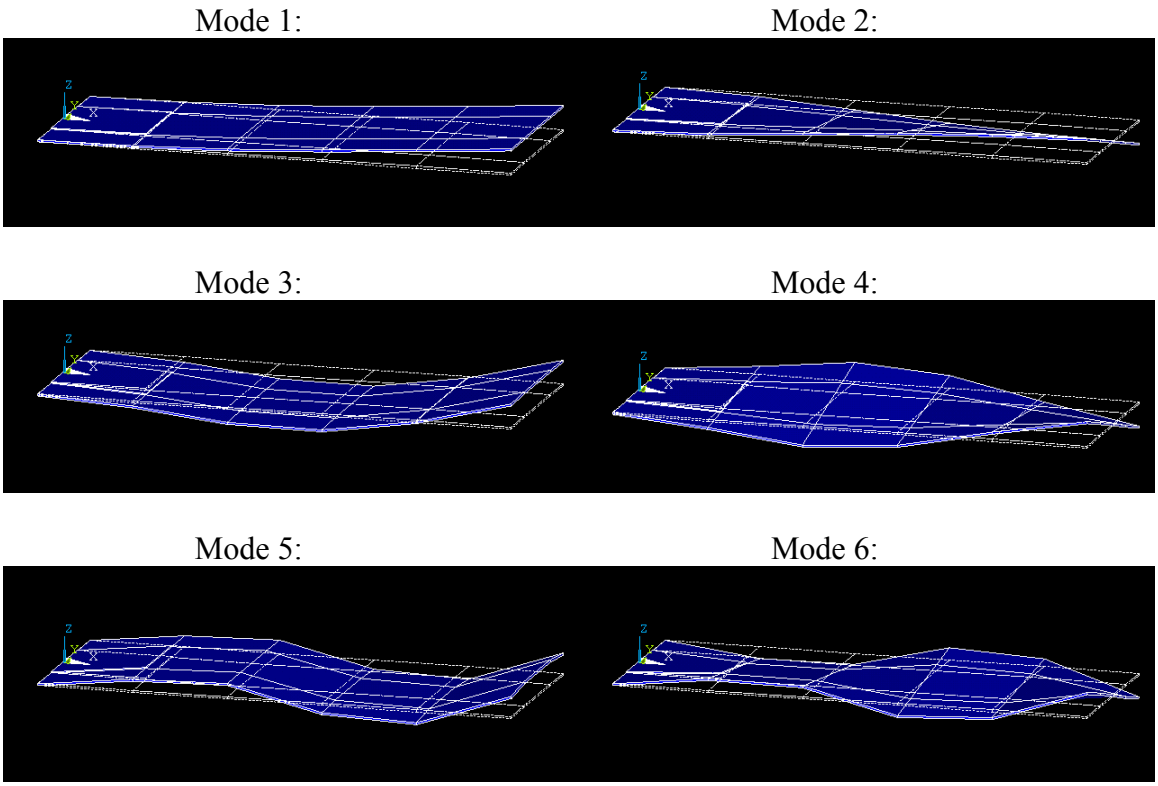

Figure 88: Mode shapes of free vibration from ANSYS 9.0 data

This analysis doesn't seem to approximate the twisting modes of vibration as well, which could potentially be due to the simplifying assumptions that the classical plate theory makes as opposed to the 20-node solid 95 element that is being used to analysis the modes. This is seen by the fact that the twisting modes are modes 2, 4, and 6 and looking at Table 6, the results are slightly skewed.

Using an array of narrow white noise with the lower cut-off frequency as 0 Hz, the upper cut-off frequency as 70 Hz, and an amplitude of 100 volts, the forced vibration analysis showed the first six modes at approximately {9, 49, 56, 151, 157, 276}Hz, which correlate to the ones found for free vibration of the laminated piezoelectric-plate. Figure 89 shows these frequencies versus displacement of point A, marked in Figure 86.

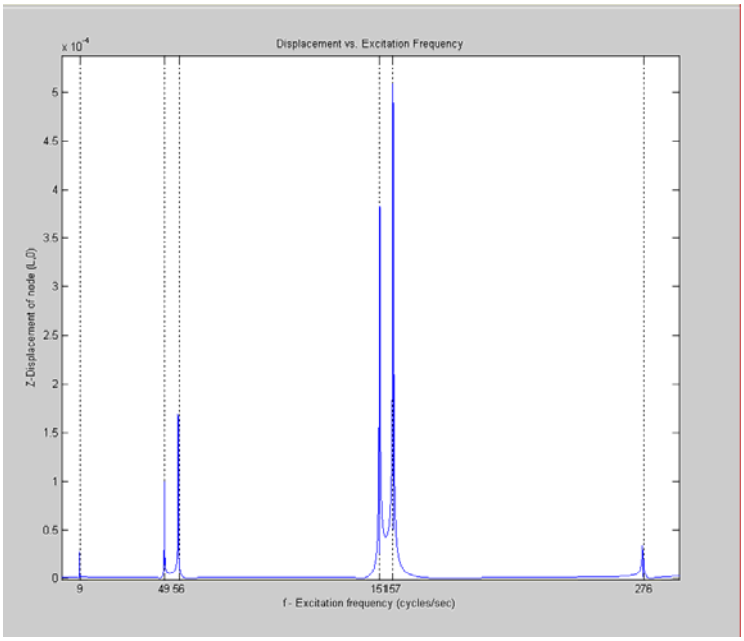

Figure 89: Piezoelectric actuation and the resulting modes of vibration, analyzed at point A

Note that the MATLAB code used for Appendix A can be found in Appendix B.6 and the simulations have also been setup to include analysis for forced vibration due to an external force and base motion.

Appendix B: Explanation of MATLAB Simulation Programs

Preface

All programs run within the MATLAB software interface. To do this, open the main program (Documented in the highest rectangle), change any input parameters in the top part of the code and run the program. The only other changes may involve where the data is saved, this is located at the end of the code. It is important to change the main input variables thoroughly so that the correct simulation is run. In addition this code takes advantage of MATLAB's ability to do computations symbolically.

The program is sectioned into three main categories: The Pre-Processor, The Solution, and the Post-Processor. The Pre-Processor deals with constants that are used throughout the program like mesh coordinates, connectivity matrices and boundary conditions. The Solution solves for the unknowns using compiled element matrices, such as $[K]^e$ and $[M]^e$. The Post-Processing section deals with plotting data, saving data and generating plots.

The MATLAB simulation code can be found on a compact disc (CD) on the back cover of this thesis. Each section and problem described below is located in a specified folder on the CD.

SECTION 1

B.1 Stokes Flow flow-down

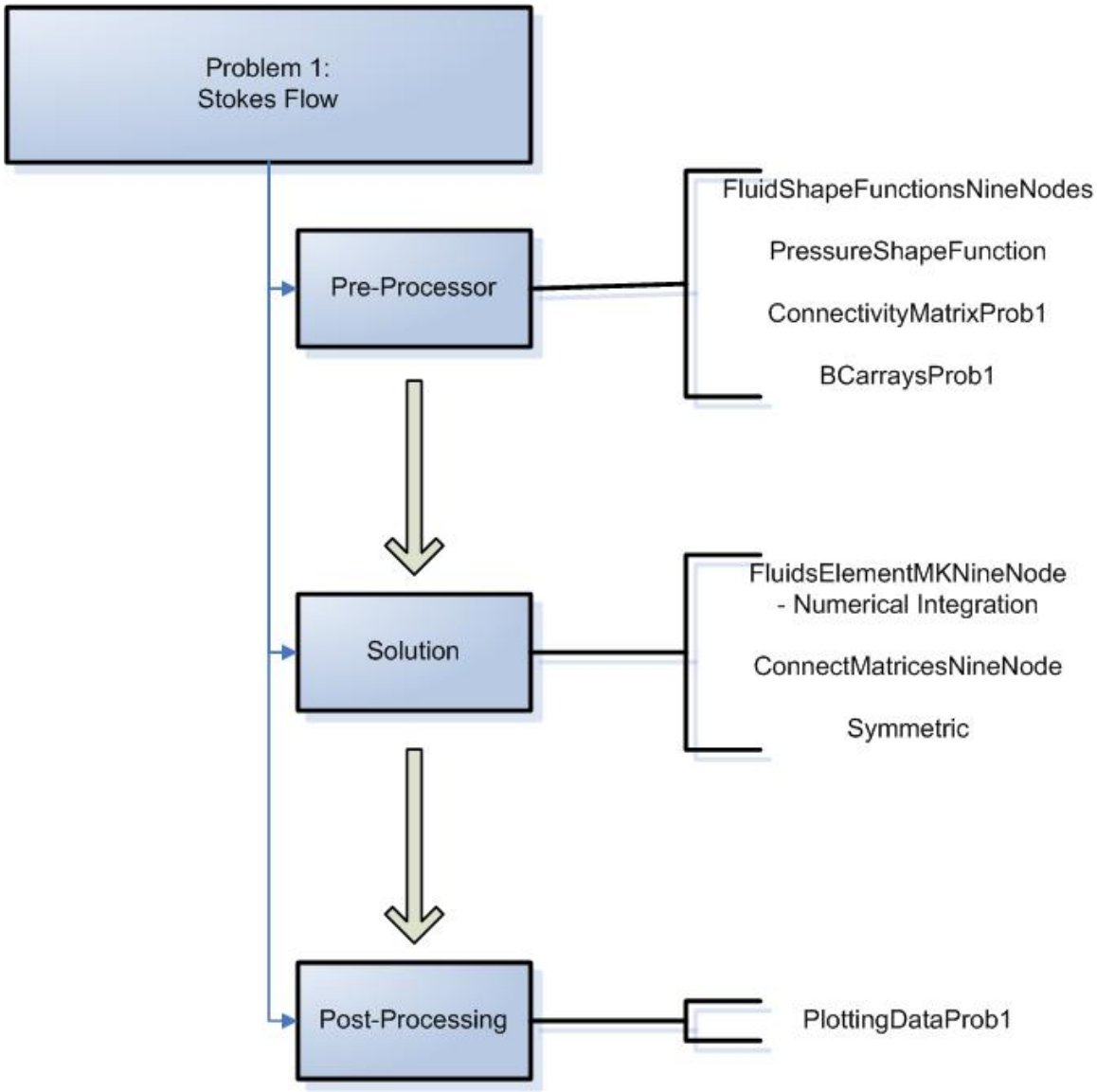

This is the flow-down chart for the programs associated with the Fluids Problem 1: Stokes Flow.

For the Pre-Processor of this program:

1. FluidShapeFunctionsNineNodes is a program that generates the symbolic expressions for the nine-noded velocity interpolation functions

2. PressureShapeFunction develops the symbolic expressions for the four-noded pressure interpolation functions
3. ConnectivityMatrixProb1 determines the individual boundary conditions, known velocity nodes and connectivity pressure/velocity matrices
4. BCarraysProb1 assembles an array consisting of ones and zeros that dictates either a unknown velocity node (1) or a known zero boundary condition (0)

For the Solution of this program:

1. FluidsElementMKNineNode is a program that calculates/integrates all the elemental matrices
2. Numerical_Integration determines if the integral expression contains both or only one local coordinate variable and integrates respectfully
3. ConnectMatricesNineNode connects all elemental matrices into global matrices
4. Symmetric is a short program that determines whether the matrix analyzed is symmetric. This was used for debugging purposes.

For the Post-Processing:

1. PlottingDataProb1 develops the appropriate data to be used later for plotting

B.2 Cavity Flow flow-down

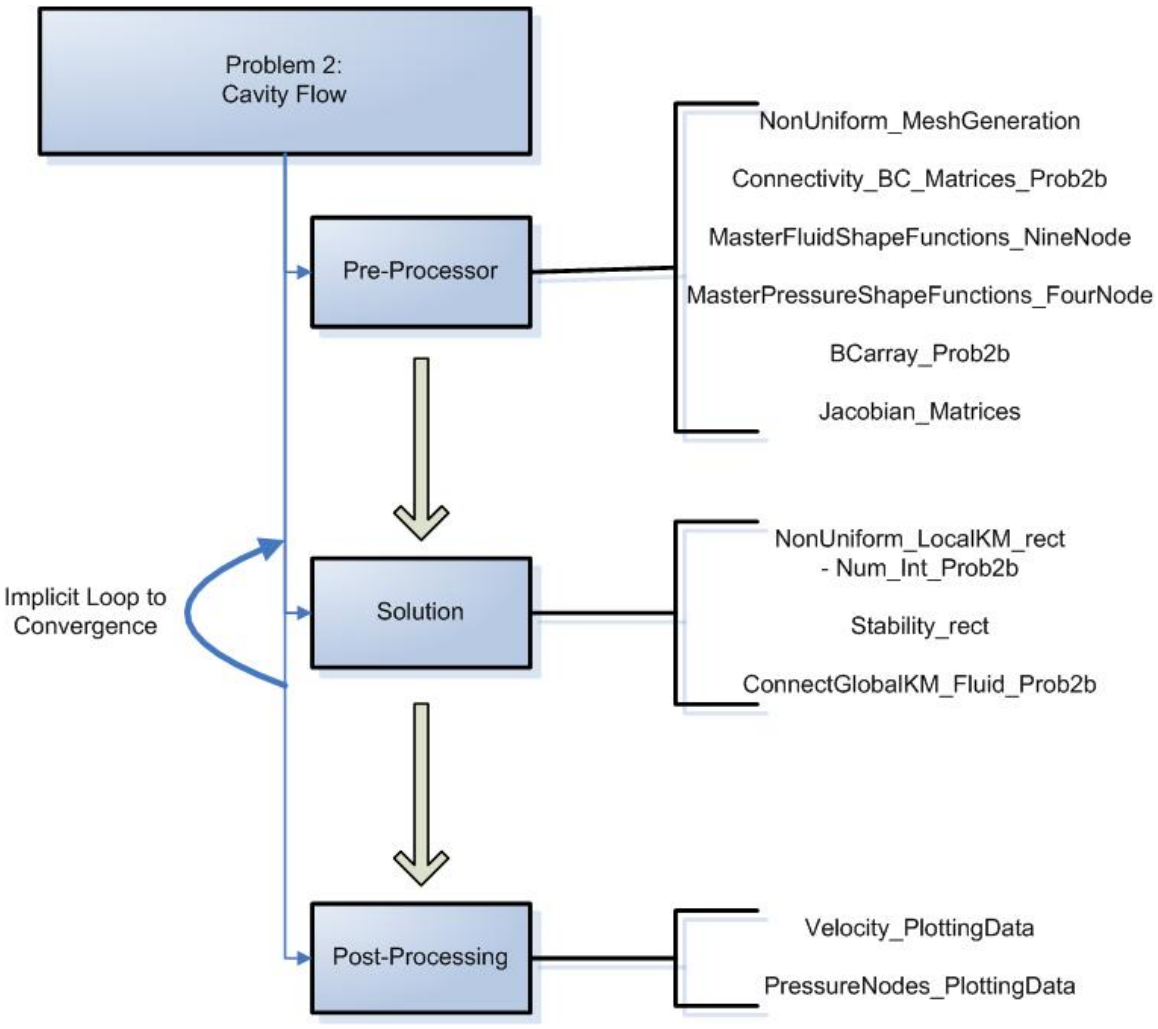

This is the flow-down chart for the programs associated with the Fluids Problem 2: Cavity Flow.

For the Pre-Processor of this program:

1. NonUniform_MeshGeneration develops arrays that consist of the x and y coordinates for the inputted elemental size requirements
2. Connectivity_BC_Matrices_Prob2b determines the individual boundary conditions, known velocity nodes and connectivity pressure/velocity matrices
3. MasterFluidShapeFunctions_NineNode generates the symbolic expressions for the nine-noded velocity interpolation functions

4. MasterPressureShapeFunctions_FourNode generates the symbolic expressions for the four-noded pressure interpolation functions
5. BCarray_Prob2b assembles an array consisting of ones and zeros that dictates either a unknown velocity node (1) or a known zero boundary condition (0)
6. Jacobian_Matrices finds the elemental Jacobian matrices

For the Solution of this program:

1. NonUniform_LocalKM_rect is a program that calculates/integrates all the elemental matrices for rectangular elements, not isoparametric
2. Num_Int_Prob2b determines if the integral expression contains both or only one local coordinate variable and integrates respectfully
3. Stability_rect calculates the stability matrices
4. ConnectGlobalKM_Fluid_Prob2b connects all elemental matrices into global matrices

Note: To obtain answers for simulations that have high Reynolds Numbers, which means a high rate of convection, an implicit iterative loop is formed over the unknown variables; in this case velocity. This loop runs until convergence is met and it was previously shown that the stability terms aided the solution to converge faster in certain situations.

For the Post-Processing:

1. Velocity_PlottingData takes the solution data for the unknowns and repackages it together with the boundary conditions and known velocities, which were taken out for solving purposes.
2. PressureNodes_PlottingData compiles a connectivity matrix for the pressure based off of the velocity nodal numbering scheme. This is used for plotting the pressure.

B.3 Plane Jet flow-down

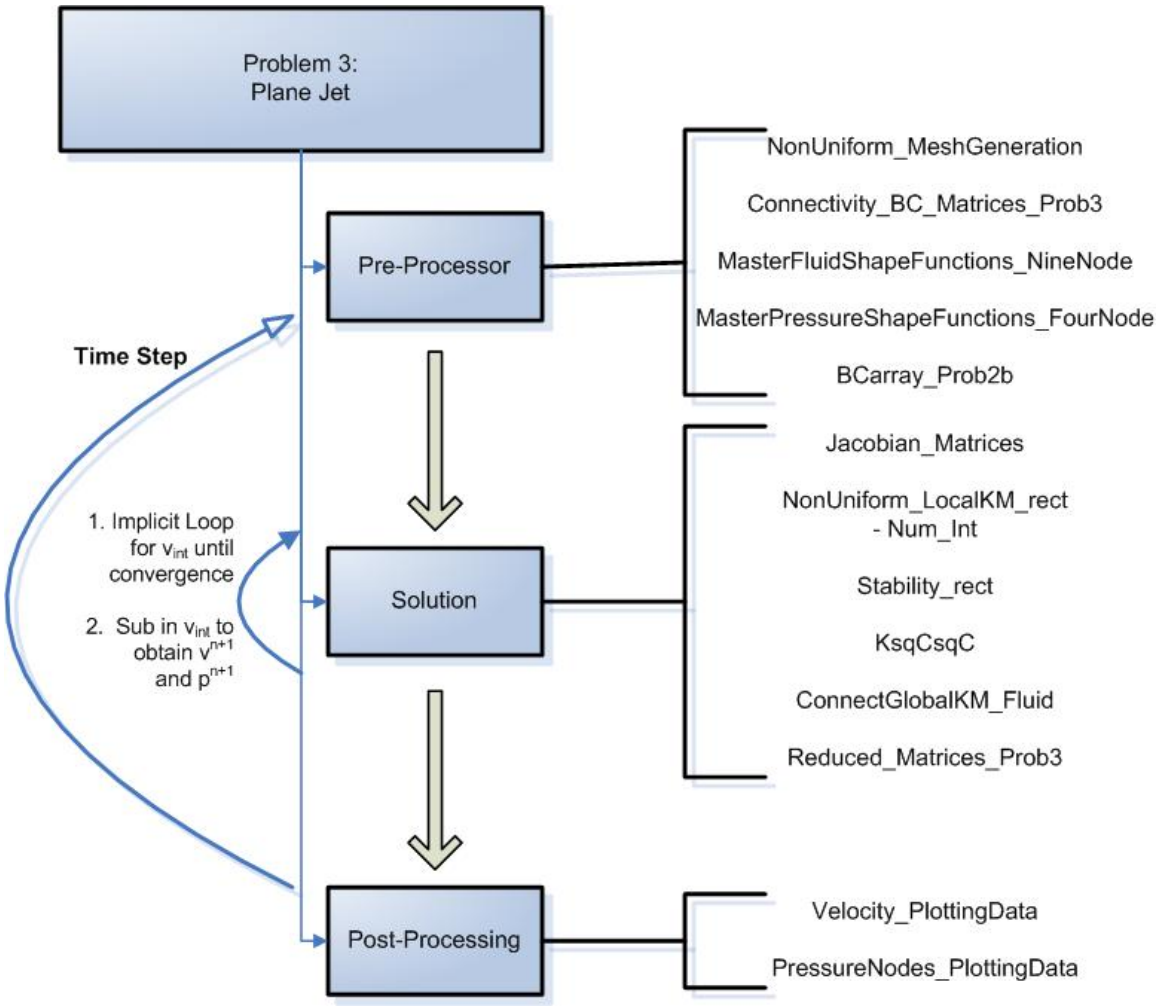

This is the flow-down chart for the programs associated with the Fluids Problem 3: Plane Jet.

For the Pre-Processor of this program:

1. NonUniform_MeshGeneration develops arrays that consist of the x and y coordinates for the inputted elemental size requirements
2. Connectivity_BC_Matrices_Prob3 determines the individual boundary conditions, known velocity nodes and connectivity pressure/velocity matrices
3. MasterFluidShapeFunctions_NineNode generates the symbolic expressions for the nine-noded velocity interpolation functions

4. MasterPressureShapeFunctions_FourNode generates the symbolic expressions for the four-noded pressure interpolation functions
5. BCarray_Prob2b assembles an array consisting of ones and zeros that dictates either a unknown velocity node (1) or a known zero boundary condition (0)

For the Solution of this program:

1. Jacobian_Matrices finds the elemental Jacobian matrices
2. NonUniform_LocalKM_rect is a program that calculates/integrates all the elemental matrices for rectangular elements, not isoparametric
3. Num_Int determines if the integral expression contains both or only one local coordinate variable and integrates respectfully
4. Stability_rect calculates the stability matrices
5. KsqCsqC is a program to condense the code found in Problem 2: Cavity Flow
6. ConnectGlobalKM_Fluid connects all elemental matrices into global matrices
7. Reduced_Matrices_Prob3 is a refined, faster algorithm that solves for the reduced global matrices, which are used in the solution of the unknowns

Note: To obtain answers for simulations that have high Reynolds Numbers, which means a high rate of convection, an implicit iterative loop is formed over the unknown variables; in this case velocity. This loop is finding the intermediate velocity, explained previously. Once the intermediate velocity is found, it is introduced to find the final end-of-step velocity and pressure. This value is then saved and a new value is found for the next time-step.

For the Post-Processing:

1. Velocity_PlottingData takes the solution data for the unknowns and repackages it together with the boundary conditions and known velocities, which were taken out for solving purposes.
2. PressureNodes_PlottingData compiles a connectivity matrix for the pressure based off of the velocity nodal numbering scheme. This is used for plotting the pressure.

SECTION 2

B.4 Laminated Piezoelectric-Beam flow-down

For the beam and laminated piezoelectric-beam analysis, the programs are significantly shorter. Therefore there is no need to show a visual flow-down chart, just a description of the pre-processor, solution and post-processor is presented. The main program is labeled: beamExampleFEM.m

It is important to note that the ANSYS 9.0 simulations including piezoelectrics needed specific variables. The program to obtain these specific variables and how to obtain them is found in conjunction with the code for the laminated piezoelectric-beam.

For the Pre-Processor of this program:

The user has to first choose which program is to be used. The options are:

1) Free Vibration
2) Forced Vibration

The second main option the user needs to input is the length of each element and the type of element. The types are either beam or laminated piezoelectric-beam element. The rest of the preprocessor allows all variables to be inputted depending on the program choosen. It is important to note that all boundary conditions are inputted by the user, where the fluid programs (above) made up all boundary conditions automatically.

For the Solution of this program:

All element matrices are found and the solution to the problem is found, depending on the options chosen above.

For the Post-Processing:

The post-processing of this program outputs/plots different data depending on the pre-processor options chosen. For the first option of free-vibration, the problem solved was an eigenvalue problem. Therefore the values that are outputted to the screen are the frequency values, first in rad/sec and then in Hertz. The second option, forced vibration, outputs the frequencies from the free vibration and also constructs a graph of frequency versus displacement of the farthest node from the cantilevered boundary condition. This graph should line up very close to the free vibration case because it shows peaks when the last node is vibrating at a particular resonance.

SECTION 3

B.5 Simplified Fluid Interaction flow-down

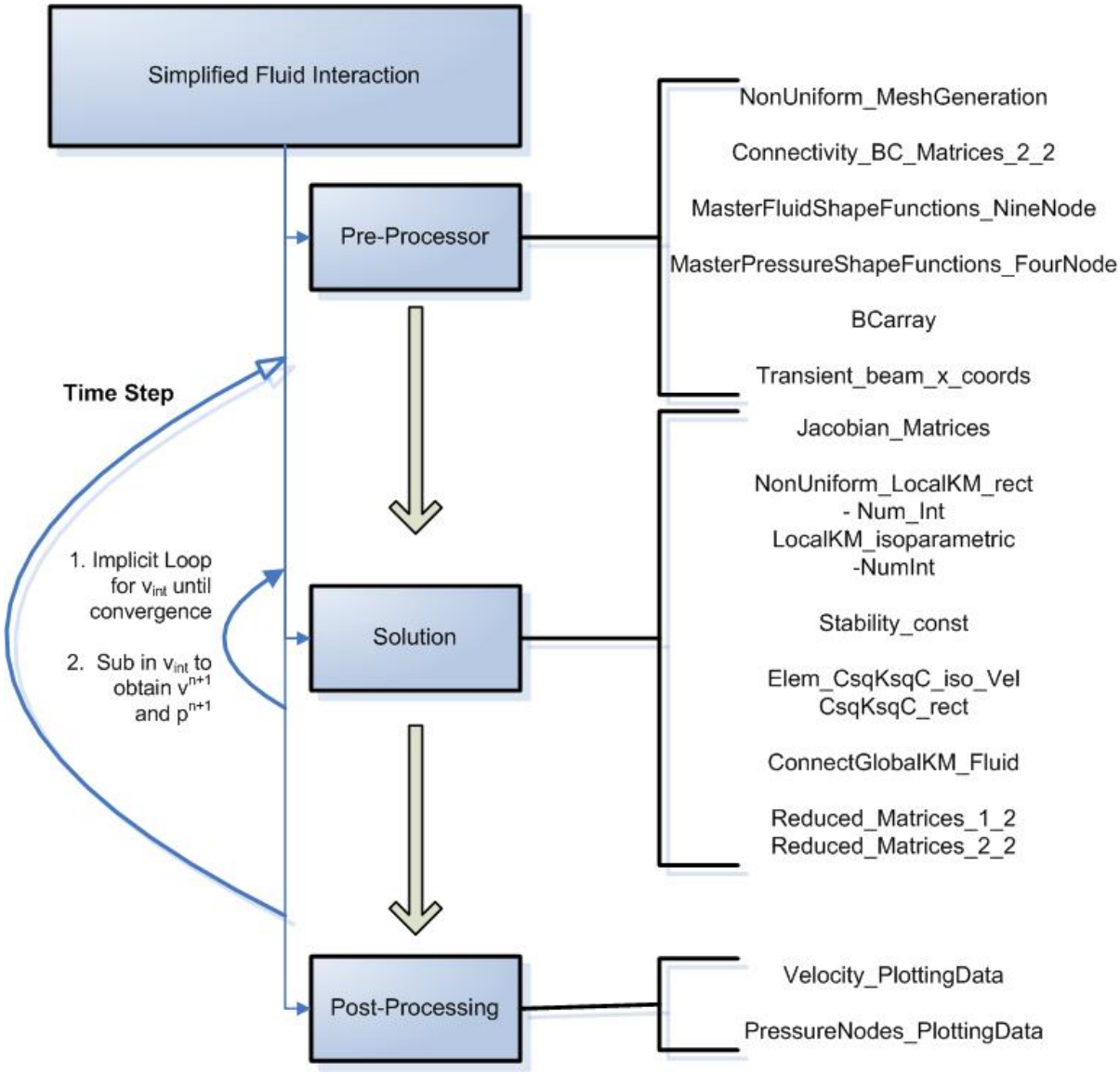

This is the flow-down chart for the programs associated with the Simplified Fluid Interaction Analysis.

<u>For the Pre-Processor of this program</u>:

1. NonUniform_MeshGeneration develops arrays that consist of the x and y coordinates for the inputted elemental size requirements

2. Connectivity_BC_Matrices_2_2 determines the individual boundary conditions, known velocity nodes and connectivity pressure/velocity matrices
3. MasterFluidShapeFunctions_NineNode generates the symbolic expressions for the nine-noded velocity interpolation functions
4. MasterPressureShapeFunctions_FourNode generates the symbolic expressions for the four-noded pressure interpolation functions
5. BCarray assembles an array consisting of ones and zeros that dictates either a unknown velocity node (1) or a known zero boundary condition (0)
6. Transient_beam_x_coords

For the Solution of this program:

1. Jacobian_Matrices finds the elemental Jacobian matrices
2. NonUniform_LocalKM_rect is a program that calculates/integrates all the elemental matrices for rectangular elements, not isoparametric
3. LocalKM_isoparam
4. Num_Int determines if the integral expression contains both or only one local coordinate variable and integrates respectfully
5. Stability_rect calculates the stability matrices
6. KsqCsqC is a program to condense the code found in Problem 2: Cavity Flow
7. ConnectGlobalKM_Fluid connects all elemental matrices into global matrices
8. Reduced_Matrices_Prob3 is a refined, faster algorithm that solves for the reduced global matrices, which are used in the solution of the unknowns

Note: To obtain answers for simulations that have high Reynolds Numbers, which means a high rate of convection, an implicit iterative loop is formed over the unknown variables; in this case velocity. This loop is finding the intermediate velocity, explained previously. Once the intermediate velocity is found, it is introduced to find the final end-of-step velocity and pressure. This value is then saved and a new value is found for the next time-step.

For the Post-Processing:

1. Velocity_PlottingData takes the solution data for the unknowns and repackages it together with the boundary conditions and known velocities, which were taken out for solving purposes.
2. PressureNodes_PlottingData compiles a connectivity matrix for the pressure based off of the velocity nodal numbering scheme. This is used for plotting the pressure.

B.6 Laminated Piezoelectric-Plate flow-down

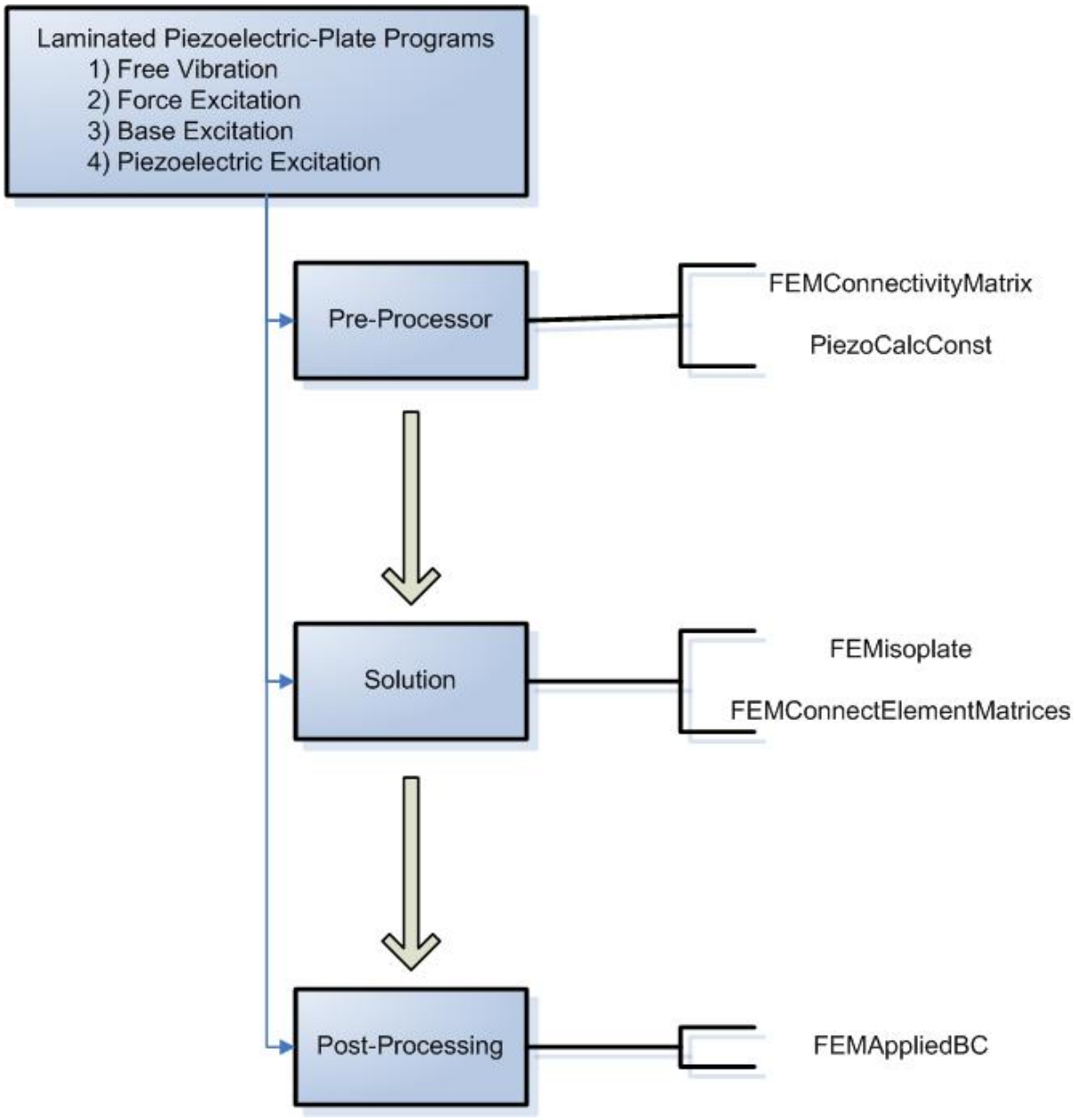

This is the flow-down chart for the programs associated with the Laminated Piezoelectric-Plate Programs. This program incorporates all the four programs developed for the laminated piezoelectric-plate vibration. The first choice the user has to make is which program to use, shown in the top box of the visual flow down chart above.

For the Pre-Processor of this program:

1. FEMConnectivityMatrix determines the connectivity matrices for each element of the plate
2. PiezoCalcConst determines all of the piezoelectric constants that are used later in the program

For the Solution of this program:

1. FEMisoplate is a program that calculates/integrates all the elemental matrices
2. FEMConnectElementMatrices connects all elemental matrices into global matrices

For the Post-Processing:

1. FEMAppliedBC develops the appropriate data to be used later for plotting